(On the Spine) LOCALIZED SURFACE PLASMON RESONANCE (LSPR) BASED BIOSENSORS CHEN PENG 2015

NANYANG TECHNOLOGICAL UNIVERSITY

LOCALIZED SURFACE PLASMON RESONANCE (LSPR) BASED BIOSENSORS

CHEN PENG

SCHOOL OF MATERIALS SCIENCE AND ENGINEERING

2015

LOCALIZED SURFACE PLASMON RESONANCE (LSPR) BASED BIOSENSORS

CHEN PENG

School of materials science and engineering

A thesis submitted to the Nanyang Technological University

In fulfilment of the requirement for the degree of

Doctor of Philosophy of materials science and engineering

2015

Abstract

Biosensors provide a quick and cheap alternative way of characterization and analysis as compared to standard analytical methods such as spectrometry, chromatography, biochemical or microbiological techniques. In the past few decades, biosensors have been quickly developed both in fundamental research and applications in the areas of medical diagnosis, pharmaceutics and environmental monitoring, as well as food, forensic, sports and defense and military science etc. Many different sensing platforms including the enzyme-linked immunosorbent assay (ELISA), surface plasmon resonance (SPR) and electrochemical sensor have been developed and found practical applications in medical diagnosis, environmental monitoring, detection of explosives etc.[1,2] Most of these sophisticated sensing platforms are available at test centers, laboratories and hospitals etc. Moreover, these biosensors generally require professional training on operation. In this thesis, I developed some biosensor that is suitable for field test. These sensors are generally robust enough to stand for harsh environmental conditions, simple to operate and require minimal instrumentations.

Localized surface plasmon resonance (LSPR) of gold nanoparticles has attracted tremendous interest in biosensing, due to its unique optical properties. The frequency and strength of the surface plasmon resonance of noble metal nanoparticles is affected by many factors, including the size, shape, inter-particle distance and surrounding medium etc. The resonance frequency and strength of the local electromagnetic field can be used to monitor the molecular interactions (bindings) occurs on (near) the surface of particle. In addition, graphene, a new

2D carbon material has been widely used in biosensing since its discovery in 2004, due to its excellent electrical and fluorescence quenching properties. The two materials are used as active materials for biosensors for their excellent property and chemical stability.

A colorimetric sensor for MMP-7, a cancer marker was designed based on peptide functionalized gold nanoparticles (AuNPs). Presence of MMP-7 digests the peptide, leading to aggregation of the AuNPs. A colorimetric change of the solution from red to blue can be detected by the naked eye. This colorimetric sensor has a huge potential because it is easy for use and it does not require any instrumentation.

Compared to SPR sensor, the refractive index (RIU) sensitivity of LSPR sensor is lower. I demonstrated that the sensitivity can be increased significantly by assembling simple spherical AuNPs into preferred configurations in 2D plane and 3D clusters. In addition to sensitivity, the noise level of LSPR peak is equally important. I demonstrate that by analyzing the LSPR peak using the curvature (overall shape of the peak) could improve the Signal-to-noise ratio for a few times than traditional methods based on peak shift and extinction. In addition, curvature is less affected by instrumental/chemical instabilities than peak shift and extinction.

I also designed a hybrid sensing platform relying on two or more independent transducing mechanisms, LSPR and Raman scattering. A prototype platform for hybrid sensor was developed by assembling gold-silver alloy particles on

graphene oxide. For biomolecules, it is generally difficult to observe the Raman scattering due to the low Raman scattering compared to the high fluorescence background. With this novel substrate, the Raman scattering is significantly enhanced, while fluorescence is quenched. The Raman to fluorescence ratio is improved by 6 orders of magnitude. In addition, this substrate can be used the same way as the LSPR sensor, where the LSPR peak shift, extinction and curvature can be used to monitor the molecule binding. With two independent responses on the same chip, more information can be obtained and the false responses from contaminants can be discriminated.

Acknowledgment

Firstly, I would like to thank Centre for Biomimetic Sensor Science and School of Materials Science and Engineering for providing me this opportunity to work on this excellent project.

I would like to thank my supervisor Prof. Bo Liedberg for his guidance and advice for the research work during my PhD study. From him I learned quite a lot of knowledge, skills and the integrity as a researcher. I would also like to express my great gratitude to Prof. Zhang Hua in MSE and Prof. Daniel Aili at Linköping University, Sweden who has given me much guidance and training on graphene oxide and peptide related work, respectively. Through them, I have gained valuable insights in the research related to nano-bio interface.

I would like to thank Dr. Chia Wei Sheng, Dr. Wang Yi, Mr. Liu Xiaohu, Mr. Lim Seng Koon and Ms. Tran Thi Nhung in CBSS and Mr. Robert Selegård and Mr. Erik Martinsson at Linköping University for their help in experiment and discussion. I would also like to thank Dr. Yin Zongyou, Dr. Wang Zhijuan, Dr. Huang Xiao, Dr. Zhou Xiaozhu, Dr. Zeng Zhiyuan and Dr. Lv Gang in MSE for their kind help on the graphene oxide related work.

Thanks also go to Ms. Ang Wunly and Ms. Phyllis Kim, the senior managers of Centre for Biomimetic Sensor Science, who helped me quite a lot on general work. I would also like to thank my FYP students Mr. Tan Guorui and Mr. Lester Lu Jingheng, who helped me doing a lot of lab works.

On a personal note, I would like to express my most sincere gratitude to my parents Chen Jiafang and Han Zongjing and my wife Hu Ping whose love, sacrifice and support made my work enjoyable.

Contents

Abstract i

Acknowledgment iv

List of Figures ix

List of Tables xxiii

Chapter 1: Introduction ..... - 1 -

1.1 Background ..... - 1 -

1.2 Motivation ..... - 3 -

1.3 Objective ..... - 4 -

1.4 Hypothesis ..... - 4 -

1.5 Materials ..... - 5 -

1.6 Methods ..... - 5 -

Chapter 2: Literature Review ..... - 8 -

2.1 Biosensors ..... - 8 -

2.2 Localized surface plasmon resonance ..... - 13 -

2.3 Effect of Shapes and Coupling ..... - 16 -

2.4 Synthesis of gold nanoparticles ..... - 18 -

2.5 Refractive Index Sensing ..... - 21 -

2.6 Colorimetric Sensing ..... - 26 -

2.7 Surface enhanced Raman scattering based biosensors ..... - 31 -

2.8 Evaluation of LSPR peaks ..... - 36 -

2.9 Graphene and graphene based sensors ..... - 37 -

2.10 Biosensing Recognition Scheme ..... - 41 -

2.11 Synopsis of following chapters ..... - 45 -

Chapter 3: Refractive index sensing using the curvature of the LSPR peak ..... - 50 -

3.1 Sensing principle: the relationship between curvature and refractive index - 51 -

3.2 Comparison of curvature to traditional peak shift and extinction techniques - 60 -

3.3 Response to small molecule binding and biosensor development ..... - 68 -
3.4 Experimental Section ..... - 73 -
3.5 Conclusions ..... - 75 -
Chapter 4: Effect of Configurations on the Refractive index Sensitivity of Coupled Gold Nanoparticles ..... - 77 -
4.1 Configurations of coupled AuNPs on 2D plane ..... - 77 -
4.2 Experimental Section ..... - 84 -
4.3 Conclusions ..... - 85 -
Chapter 5: Controlled aggregation of gold nanoparticles and colorimetric Sensor for matrix metalloproteinase 7 (MMP-7) ..... - 86 -
5.1 Controlled aggregation by complementary peptide and salt ..... - 86 -
5.2 Colorimetric sensor for MMP-7 ..... - 89 -
5.3 Experimental Section ..... - 101 -
5.4 Conclusions ..... - 103 -
Chapter 6: Towards a LSPR and Raman hybrid sensing ..... - 105 -
6.1 LSPR and Raman hybrid sensing chip ..... - 105 -
6.2 Experimental section ..... - 118 -
6.3 Conclusions ..... - 121 -
Chapter 7: Collaborative projects on plasmonics and biosensors ..... - 122 -
7.1 Colorimetric Sensor 1: Bio-functionalized gold nanoparticles for colorimetric sensing of botulinum neurotoxin A light chain ..... - 122 -
7.2 Colorimetric Sensor 2: Gold aggredots for colorimetric G6PD deficiency sensing ..... - 125 -
7.3 Colorimetric Sensor 3: Peptide-assembled graphene oxide as fluorescent turn-on sensor for specific and sensitive lipopolysaccharide detection ..... - 127 -
7.4 Platform 1: Optimizing the refractive index sensitivity of plasmonically coupled gold nanoparticles ..... - 129 -
7.5 Platform 2: High-density metallic nanogaps fabricated on solid substrates used for surface enhanced Raman scattering ..... - 131 -

7.6 Electrical sensor 1: Label-free, electrochemical detection of methicillin-resistant staphylococcus aureus DNA with reduced graphene oxide-modified electrodes ..... - 133 -

7.7 Electrical sensor 2: Real-time DNA detection using Pt nanoparticle-decorated reduced graphene oxide field-effect transistors ..... - 136 -

Chapter 8: Conclusion and Future Perspectives ..... - 139 -

Chapter 9 Publications Chen Peng ..... - 143 -

9.1 Journals ..... - 143 -

9.2 Conferences and Workshops ..... - 146 -

References ..... - 148 -

List of Figures

Figure 2.1 A typical SPR sensor setup consists of a sensor chip, a flow system and an optical detection system. Adapted by permission from Macmillan Publishers Ltd: Nature Reviews Drug Discovery with ref. [4] copyright©2002. .....- 12 -

Figure 2.2 Illustration of the localized surface plasmon resonance. Free electrons in metal spheres oscillate with the electromagnetic (EM) filed. When the frequency of EM filed matches with the intrinsic frequency of metal sphere, a resonance occurs. Reprinted with permission from ref.[2] Copyright © 2007, Annual Reviews. .....- 14 -

Figure 2.3 (a) Configuration of a refractive index sensor for streptavidin based on AuNPs (b) Response of resonance energy with receptor and target molecules. Adapted with permission from ref.[1] Copyright ©2003 American Chemical Society.....- 22 -

Figure 2.4 (a) Fabrication protocol of LSPR sensor (b) Detection principle of LSPR sensor. Adapted with permission from ref.[45] Copyright ©2003 American Chemical Society. .....- 23 -

Figure 2.5 (a) Absorption spectra of biotin functionalized AuNPs after addition of 0 μg/mL (A), 10 μg/mL (B) and 100 μg/mL fibrinogen (C), respectively. (b) Changes in absorbance at 550 nm as a function of time with the adsorption of fibrinogen. Adapted with permission from ref.[45] Copyright ©2003 American Chemical Society. .....- 24 -

Figure 2.6 Illustration of the colorimetric sensor for DNA. AuNPs are functionalized with probe DNAs which keep the AuNPs stable and dispersed. The target DNA could bind to 2 probe DNAs, resulting in aggregation of the AuNPs. Reprinted with permission from ref.[31] Copyright © 1997, American Association for the Advancement of Science. ..... - 27 -

Figure 2.7 The concentrations of Cd^{2+} in tubes 1 to 9 are 0, 0.06, 0.12, 0.18, 0.24, 0.30, 0.36, 0.42, and 0.48 μM, respectively. Reprinted with permission from ref.[19] Copyright © 2013, Springer-Verlag Wien. ..... - 28 -

Figure 2.8 Illustration of the protease triggered dispersion of aggregated AuNPs. 1: intact oligopeptide and 2: digested oligopeptide. Reprinted with permission from ref.[121] Copyright © 2007, American Chemical Society. ..... - 29 -

Figure 2.9 Illustration of the working principle of the colorimetric sensor. (a) Displacement of polymer dyes by protein increase the fluorescence of the dye. (b) Fluorescence pattern generation by protein adsorption to AuNPs with different polymer dyes conjugates. Reprinted with permission from ref.[122] Copyright © 2007, Rights Managed by Nature Publishing Group. ..... - 30 -

Figure 2.10 Illustration of the principle of detection of DNA. Dye labeled probe DNA is physically adsorbed on the GO surface, where the fluorescence of dye is quenched by GO. Hybridization of target DNA release the dye labeled probe DNA from the GO surface and the fluorescence recovers. Reprinted with permission from ref.[33]Copyright © 2009 WILEY-VCH Verlag GmbH & Co. KGaA, Weinheim. ..... - 31 -

Figure 2.11 Illustration of Raman scattering, Rayleigh scattering, IR absorption and energy levels.....- 32 -
Figure 2.12 A sensor for DNAs by characterizing SERS response. Probe DNA is first immobilized on the substrate to allow target DNA hybridization. A second DNA which could bind to the target DNA is labeled with dyes and immobilized on AuNPs (AuNP-DNA-dye). The intensity of SERS spectrum from the AuNP-DNA-dye is used to monitor the concentration of target DNA. Reprinted with permission from ref.[48] Copyright © 2002, American Association for the Advancement of Science.....- 34 -
Figure 2.13 SERS spectra of dAMP of different concentrations: (a)0.03 (b) 0.01 (c) 0.001 ppm. Inset shows the calibration curve. Reprinted with permission from ref.[143] Copyright © 2006, American Chemical Society.....- 35 -
Figure 2.14 The area in red is denoted D (dispersed) which is the integration from 490 to 540 nm. The area in blue is denoted A (aggregated) which is the integration from 550 to 700 nm. The spectra in a) and b) show the change in the A/D ratio for dispersed and aggregated particles, respectively. Reprinted with permission from ref.[64] Copyright © 2011, American Chemical Society.....- 37 -
Figure 2.15 Illustration of a FET sensor based on a suspended thermally reduced graphene oxide (TRGO) for immunoglobulin G (IgG). Anti-IgG molecules are immobilized on the TRGO sheet through gold nanoparticles (AuNPs). Adapted with permission from ref.[164] Copyright © 2010 WILEY-VCH Verlag GmbH & Co. KGaA, Weinheim.....- 40 -

Figure 2.16 sequence of JR2EC and JR2KC. Adapted with permission from ref.[174] Copyright © 2005, American Chemical Society. .....- 44 -
Figure 2.17 Illustration of the curvature of the LSPR peak of AuNPs. .....- 45 -
Figure 2.18 Effect of local electrical field on the AuNPs depends on the position of the neighboring AuNPs. Illustration of AuNP and AuNP clusters with different configurations. .....- 46 -
Figure 2.19 Illustration of the colorimetric sensor of MMP-7: digestion of peptide on AuNPs leads to an aggregation of AuNPs and color changes. .....- 47 -
Figure 2.20 Illustration of the enhancement of Raman scattering from $Au_{0.7}Ag_{0.3}$ NPs and fluorescence quenching from graphene.....- 48 -
Figure 3.1 (a) Real (filled triangle) and imaginary (open triangle) Johnson and Christy dielectric function of 13 nm gold nanoparticles (AuNPs) corrected for the size dependent surface damping. (b) Real (filled triangle) and imaginary (open triangle) dielectric function of 13 nm AuNPs in (a) near the LSPR peak. The real part is fitted with a linear function, Eq.(3.5) while the imaginary part is fitted with a reciprocal function, Eq.(3.6). Experimentally determined fitting constants are: a_1 =31.27, b_1= -0.0676, R^2=0.9999, a_2 =-1.799, b_2=0.00416, R^2=0.9864. (c) Measured absorption spectrum of 13 nm AuNPs in solution (open circles) and calculated absorption spectrum (solid line) by Mie theory using size corrected dielectric function fitted with the functions in (b), Eq.(3.10). Both spectra show a LSPR peak at ~ 521.0 nm. (d) Calculated changes in curvature K for AuNPs exposed to different media with refractive indices varying from 1 to 2, Eq.(3.15).
- 52 -

Figure 3.2 (a) Transmission electron microscope (TEM) image of as prepared AuNPs. (b) Histogram of the size distribution of AuNPs shown in (a). (c) Absorption spectrum of AuNPs in solution. (d) Scanning electron microscope (SEM) image of AuNPs assembled on glass substrate. (e) Absorption spectrum of AuNP SAMs on glass in air. ..... - 55 -

Figure 3.3 (a) Absorption spectra of AuNP SAMs on glass substrate immersed in solvents with different refractive indices: 1.333 (black), 1.364 (red), 1.399 (blue), 1.432 (green) and 1.474 (purple), respectively. Spectra are offset in purpose for better visualization. Inset: zoom in absorption spectra of AuNPs in solvent with refractive index 1.333 (black) and 1.474 (purple). (b) Second order derivatives of absorption spectra in (a). (c) Experimental (black circles/line) and calculated (red circles/line) curvature of AuNPs immersed in media with different refractive index. Experimental (black) and calculated (red) data are fitted linear function to yield a slope of 5.19×10^{-6} $nm^{-2}RIU^{-1}$ (R^2=0.9804) and 5.49×10^{-6} $nm^{-2}RIU^{-1}$ (R^2=0.9876), respectively. (d) Experimentally measured peak shift (squares) and absorbance (triangles) at different refractive indices. The peak shift is fitted linearly, with a slope of 34 nm/RIU (R^2=0.9970). ..... - 57 -

Figure 3.4 (a) TEM image of 40 nm sized AuNPs . (b) Size distribution of the 40 nm AuNPs in (a). (c) the curvature of 40 nm AuNP assemblies measured at different refractive index (black dots) and linear fitting (red line). The slope of the fitted line is 1.4×10^{-4} $nm^{-2}RIU^{-1}$ and R^2 equals 0.9910. (d) TEM image of 20 nm sized AuNPs . (e) Size distribution of the 20 nm AuNPs in (d). (f) the curvature of 20 nm AuNP assemblies measured at different refractive index (black dots) and

linear fitting (red line). The slope of the fitted line is 1.5×10^{-5} $nm^{-2}RIU^{-1}$ and R^2 equals 0.9726. ..... - 59 -
Figure 3.5 (a)-(d) absorption spectrum of AuNP sample 1, 2, 3 and 4 in different solvents with refractive indices from 1.333 to 1.474, respectively. (e)-(h) FESEM image of AuNP sample 1,2,3 and 4, respectively. ..... - 62 -
Figure 3.6 The S/N ratio of peak shift, absorbance and curvature of four different AuNP assemblies calculated from optimized noise levels, respectively. ..... - 64 -
Figure 3.7 (a) Extinction spectrum of AuNP assemblies on glass measured in water. (b) The first (black) and second order (red) derivatives of the spectrum in (a). (c) The second order derivative of spectrum in (a) with 9 (black), 19 (red), 29 (blue), 39 (cyan), 49 (pink) and 69 (brown) data points used in the calculation of derivatives. (d) S/N ratio with bulk refractive index of curvature calculated using different number of data points. ..... - 65 -
Figure 3.8 (a) 31 absorption spectra of AuNP on glass immersed in water measured over time. The time interval of measurement is 1 min. Arrow: stable baselines are observed from time 1 to 19 min. Errors occurs at time 20 min for some particular reasons. Left rectangle: spectra start to tilt from spectrum 20. Right rectangle: spectra shift upwards. Middle rectangle: a step-like feature appears near the peak maximum. (b) Evolution of peak shift (the maximum) over time. (c) Evolution of absorption over time. (d) Evolution of curvature over time. Dashed lines: 3 time the standard deviation (3σ) of baseline from 1 to 19 min. - 66 -
Figure 3.9 (a) Evolution of absorption spectra of AuNP assemblies on glass upon incubation of 10 μM SH-PEG_7-COOH. The SH-PEG_7-COOH was introduced

after 10 min stabilization. (b) Peak shift of the absorption spectra in (a) at different time of incubation. (c) Absorbance of the absorption spectra in (a) at different time of incubation. An overall shift down of spectrum occurs at time 24 min, see inset (23, 24 and 25 min). (d) Curvature of the absorption spectra in (a) at different time of incubation.....- 69 -
Figure 3.10 (a) GST protein (monomer) and GSH molecule. (b) Illustration of the LSPR sensor for GSH. .....- 71 -
Figure 3.11 (a) curvature of 13 nm AuNP assembly on glass with addition of 0.5 mM GSH at time 2 min. (b) Curvature of 13 nm AuNP assembly with different concentrations of GSH.....- 72 -
Figure 4.1 (a) Illustration of the effect of near field from surrounding AuNP. (b) Simplification of a high density AuNP SAMs into a heptamer configuration. - 78 -
Figure 4.2 Different configurations of AuNP clusters used in simulation at different surrounding media. The size of AuNP is 40 nm and inter-particle distance is 2 nm.....- 79 -
Figure 4.3 Electro-magnetic field strength around a single AuNP (a) and a heptamer (b). The color bar is in $\log_{10}$ scale.....- 80 -
Figure 4.4 Simulated extinction spectra of different AuNP clusters illustrated in Figure 4.2 at different refractive indices: red 1.0, blue 1.2, green 1.4 and black 1.6. (a) monomer, (b) dimer, (c) trimer close, (d) trimer straight, (e) tetramer and (f) heptamer.....- 81 -
Figure 4.5 Peak shift at different refractive indices of various AuNP clusters are shown in (a) and the sensitivity is summarized in (b). .....- 81 -

Figure 4.6 (a) 13 nm AuNPs assembled on APTES modified glass with low density (b) 13 nm AuNPs assembled on APTES modified glass with high density.- 82 -
Figure 4.7 (a) Absorption spectra of low density AuNP SAMs in solvents with different refractive indices. (b) Absorption spectra of high density AuNP SAMs in solvents with different refractive indices. ..... - 83 -
Figure 4.8 Peak shift of individual peak in low density SAMs (open square) and linear fitting with slope of 38.4 nm/RIU and R2 of 0.9801. The coupling peak (solid square) in high density SAMs and linear fitting with slope of 269.7 nm/RIU and R2 of 0.9213. ..... - 84 -
Figure 5.1 (a) Illustration of the aggregation of AuNPs induced by cross-linking molecules. Adapted with permission from ref.[64] Copyright © 2011, American Chemical Society. (b) Illustration of the forces that keep the AuNPs stable in solution. In equilibrium the Van der Waals attraction force between AuNPs equals the columbic repulsive force between charged layers. ..... - 86 -
Figure 5.2 (a) Extinction spectra of 20 nm JR2EC functionalized AuNPs with addition of 25 nM JR2KC$_2$ peptide. (b) Peak position of the extinction spectra in (a) after addition of JR2KC$_2$ at different time. (c) Extinction spectra of 20 nm AuNPs with addition of 50 mM NaCl. (d) (b) Peak position of the extinction spectra in (c) after addition of 50 mM NaCl. ..... - 87 -
Figure 5.3 (a) Structure of MMP-7 rendered with pyMOL based on PDB data. Bule balls stand for zinc ions and black balls stand for calcium ions. (b) MALDI-TOF spectrum of MMP-7. Reproduced from ref.[12]with permission from The Royal Society of Chemistry. ..... - 90 -

Figure 5.4 Working mechanisms of the colorimetric sensor. The JR2EC peptide contains a cysteine group at position 22 (green), and two digestion sites at 11 and 26 (red arrow). Adapted from ref.[12]with permission from The Royal Society of Chemistry. ..... - 92 -
Figure 5.5 (a) MALDI-TOF spectra of the intact JR2EC peptide (black) and JR2EC peptide after incubation with 1 μg/mL MMP-7 for 2 hr at 25 ℃ in PBS buffer with pH 7.4 (red); b) Ellipsometric image of the patterns of JR2EC peptide on gold surface before (+) and after (-) digestion with MMP-7; c) Height profile of JR2EC patterns on gold thin film along the red line in (b) before (black) and after the digestion of MMP-7 (red). The thicknesses reported in the profiles are measured with respect to the hydroxyl-terminated thiol frames. Adapted from ref.[12]with permission from The Royal Society of Chemistry. ..... - 94 -
Figure 5.6 Sequence, primary structure, peptide surface, highlight of positive and negative amino acids, and electrostatic potential of intact and digested JR2EC peptide calculated at pH 7. Reproduced from ref.[12]with permission from The Royal Society of Chemistry. ..... - 95 -
Figure 5.7 (a) UV-Vis extinction spectra of citrate-capped AuNPs (black) and JR2EC modified AuNPs after exposure to MMP-7 (blue), MMP-2 (red), MMP-7 with 10 μM inhibitor II (green) and MMP-7 with 10 mM EDTA (pink), respectively in PBS at pH 7.4. (b) Sequential extinction spectra of JR2EC modified AuNPs obtained during 30 min in the presence of 2 μg/mL MMP-7. (c) Plot of the evolution of the extinction maximum with time in the presence of 4 μg/mL MMP-7 in 20 min. Data points were fitted with exponential curve, the R^2

of which is equal to 0.9928. (d) Evolution of the extinction maximum with time for MMP-7 at different concentrations from top to bottom: 4 μg/mL, 2 μg/mL, 0.5 μg/mL and 0.1 μg/mL, respectively. Adapted from ref.[12] with permission from The Royal Society of Chemistry. ..... - 96 -
Figure 5.8 TEM images of the peptide functionalized AuNPs (a) before and (b) after 2 μg/mL MMP-7 digestion. Scale bar: 20 nm. Adapted from ref.[12] with permission from The Royal Society of Chemistry. ..... - 98 -
Figure 5.9 (a)Normalized extinction spectra of JR2EC modified AuNPs at different concentrations of MMP-7 from left to right is 0 μg/mL, 0.1 μg/mL, 0.5 μg/mL, 1 μg/mL, 2 μg/mL, and 4 μg/mL, respectively at time 4 min. Inset: zoom in extinction spectra. (b) LSPR peak position versus MMP-7 concentration incubated for different time from bottom to top: 0, 2, 4, 8 and 20 min, respectively. (c) LSPR peak position versus MMP-7 concentration (black line). The dashed line represents the extinction peak position plus 3 times of standard deviation (σ = 0.1 nm) of the JR2EC functionalized AuNPs which is used to determine the limit of detection (LOD). (d) Photos of JR2EC modified AuNPs without MMP-7 and with 2 μg/mL MMP-7 incubated for 20 min. Adapted from ref.[12] with permission from The Royal Society of Chemistry. ..... - 100 -
Figure 6.1 Illustration of a hybrid sensing platform. The LSPR response is monitored with UV/Vis absorption spectrometer while the Raman scattering is monitored by a Raman spectrometer. ..... - 106 -
Figure 6.2 (a) Peak of extinction spectra of AuAg alloy NPs with different molar fraction of Au (dots). The fitted curve (red line) shows a slope of 1.27 nm/1%Au

and R^2 of 0.9993 (b) Extinction spectrum of $Au_{0.7}Ag_{0.3}$ NPs. The peak position of this spectrum is 488 nm. (c) TEM image of the $Au_{0.7}Ag_{0.3}$ NPs. (d) Energy-dispersive X-ray spectroscopy (EDX) spectrum of $Au_{0.7}Ag_{0.3}$ NPs. The molar percentage of Au is measured to equal 69.5%. ..... - 108 -
Figure 6.3 (a) atomic force microscope (AFM) image of as-synthesized GO on SiO_2 substrate. (b) The height profile along the red line in (a). ..... - 110 -
Figure 6.4 Illustration of the assembly process of graphene oxide and $Au_{0.7}Ag_{0.3}$ NPs on SiO_2 substrate. Reprinted with permission from ref.[95] Copyright © 2011, American Chemical Society. ..... - 111 -
Figure 6.5 Raman spectra of graphite flakes, GO, activated GO and functionalized GO (FGO). Adapted with permission from ref.[95] Copyright © 2011, American Chemical Society. ..... - 111 -
Figure 6.6 FESEM image of SiO2/FGO/Au-Ag NP substrate. Scale bar: 500 nm. Adapted with permission from ref.[95] Copyright © 2011, American Chemical Society..... - 113 -
Figure 6.7 (a) Raman spectra of Alexa fluor 488 on the SiO_2, SiO_2/Au-Ag NP, SiO_2/FGO/Au-Ag NP and SiO_2/FGO, respectively. Characteristic peaks of Alexa fluor 488 in the blue spectrum are indicated by stars. The intensity of the spectrum on SiO_2 is divided by a factor of 5. Inset: Zoom in of the Raman spectrum of Alexa fluor 488 on SiO_2/FGO in the area of dotted square of green spectrum. (b) S/B ratio of different substrates: SiO_2 (10^{-6}), SiO_2/Au-Ag NP (0.039), SiO_2/FGO (0.12) and SiO_2/FGO/Au-Ag NP (1.6), respectively. Reprinted with permission from ref.[95] Copyright © 2011, American Chemical Society.- 114 -

Figure 6.8 The working principle of the SiO2/FGO/Au-Ag NP substrate. Adapted with permission from ref.[95] Copyright © 2011, American Chemical Society.- 116 -
Figure 6.9 (a) Absorption spectrum of the FGO/Au-Ag NP Raman substrate on glass measured in air. (b) The peak shift of the FGO/Au-Ag NP Raman substrate measured in solvents with different refractive indices. The peak position is linearly fitted with slope of 85.5 nm/RIU and R^2 of 0.9958.....- 117 -
Figure 7.1 Schematic illustration of the mixing (A) and bridging (B) assays for detection of BoLcA using two peptide-designs (1 and 2) and bio-functionalized AuNPs. Reprinted with permission from ref.[25] Copyright © 2014, American Chemical Society. .....- 123 -
Figure 7.2 (a) Calibration curve for the BoLcA concentrations by the bridging assay. (Error bars are the standard error of n measurements, $n \geq 3$) (b) Photograph of the navi-AuNP solutions with 10, 3, 1, 0.3, 0.1 and 0 nM of BoLcA from left to right. Adapted with permission from ref.[25] Copyright © 2014, American Chemical Society. .....- 124 -
Figure 7.3 (a) FESEM image of AuNPs in an aggregated dot. (b) FESEM images of AuNPs dispersed from (a) with addition of 10 mM GSH. .....- 126 -
Figure 7.4 Photos of the aggregated AuNP dots in different stage of dispersion with addition of GSH and BME (control experiment).....- 126 -
Figure 7.5 Structure of LPS and (B) Sensing principle of the peptide-GO assembled LPS sensor.....- 128 -
Figure 7.6 Detection of LPS in buffer containing LPS standards (a) Fluorescence titration spectra of peptide-GO assembled upon addition of 0 to 10 μM of LPS.

The inset shows the corresponding fluorescence change in absence (left) and in the presence of 8 μM LPS (right). (b) Calibration curve of fluorescence intensity change [(F- F0)-1] vs the concentration of LPS (0-20 nM). F0 and F are fluorescence intensities at 572 nm in the absence and the presence of LPS, respectively. .....- 129 -
Figure 7.7 Extinction spectra obtained in water/sucrose mixtures (0-50%) for individual gold nanoparticles; a) 25 nm, b) 50 nm, c) 100 nm and for particle coupling between; d) 25 nm + 25 nm, e) 50 nm + 25 nm and f) 100 nm + 25 nm. G) LSPR maximum in a-c and plasmon coupling LSPR maximum in d-f plotted as a function of refractive index. The sensitivities was obtained through linear fitting. Reprinted with permission from ref.[200] Copyright © 2013, Springer Science+Business Media New York.....- 130 -
Figure 7.8 Schematic illustration of the fabrication process of the high-density nanogaps of Au and Ag on Si wafer. (a) First-round Au or Ag NPs were deposited on Si wafer. (b) Second-round deposition of Ag or Ag NPs on the exposed Si region in (a). (c) Third-round deposition of Au or Ag NPs on the exposed Si region in (b). (d) Raman scattering from PATP on the substrate. Reproduced from ref.[191] with permission from The Royal Society of Chemistry.....- 132 -
Figure 7.9 Raman spectra of (a) methylene blue, (b) rhodamine 6G, (c) 3,5-dibromopyrene and (d) pyrene on the SERS substrate. Adapted from ref.[191] with permission from The Royal Society of Chemistry. .....- 133 -

Figure 7.10 Schematic illustration of the surface functionalization process of the glassy carbon electrode for DNA detection. Reprinted with permission from ref. [160] Copyright © 2011, Elsevier. ..... - 134 -

Figure 7.11 (A) Nyquist plots of GCE-APTES-rGO-ssDNA hybridized with target DNA at different concentrations: (a) 0, (b) 10^{-14}, (c) 10^{-13}, (d) 10^{-11}, (e) 10^{-9}, (f) 10^{-8}, (g) 10^{-7} and (h) 10^{-6} M. Inset: magnification of curves a, b and c. (B) Calibration curve and control experiment with 20-mer and 30-mer non-complementary DNAs. Adapted with permission from ref. [160] Copyright © 2011, Elsevier. ..... - 135 -

Figure 7.12 illustration of fabrication process of a solution-gated FET sensing device based on PtNPs/rGO films. Reproduced from ref.[265] with permission from The Royal Society of Chemistry. ..... - 137 -

Figure 7.13 (a) Real-time response of the hybridization of target DNA to probe DNA in PBS buffer (black line) and a control experiment result with addition of non-complementary DNA (red line). (b) Plot of conductance change at different concentrations of target DNA. Reproduced from ref.[265] with permission from The Royal Society of Chemistry. ..... - 137 -

List of Tables

Table 2.1 summary of nanostructures of various metals have been synthesized. Reprinted with permission from ref. [97] Copyright © 2009 WILEY-VCH Verlag GmbH & Co. KGaA, Weinheim. ..... - 21 -

Table 2.2 Summary of the refractive index sensitivity of various nanostructures- 25 -

Table 3.1 Refractive index sensitivity *S*, noise and signal-to-noise ratio (*S/N*) for the peak shift (λ), absorbance (*A*) and curvature (*K*), respectively. Two methods are used to calculate the noise for each variable. For the peak shift: the centroid (centre of gravity of peak) [56] and shift of peak maximum. For the absorption: the response for the fitted A_{max} and the response at of A at 546 nm. For the curvature K: the response for the fitted K_{max} and the response of K at 546 nm. ..... - 63 -

Chapter 1: Introduction

1.1 Background

Biosensors provide a quick and cheap alternative way of characterization and analysis as compared to standard analytical methods such as spectrometry, chromatography, biochemical or microbiological techniques. In the past few decades, biosensors have been quickly developed both in fundamental research and applications. Biosensors are widely explored and used in the areas of medical diagnosis, pharmaceutics and environmental monitoring, as well as food, forensic, sports and defense and military science etc. Many different sensing platforms including the enzyme-linked immunosorbent assay (ELISA), surface plasmon resonance (SPR) and electrochemical sensor have been developed and found practical applications in medical diagnosis, environmental monitoring, detection of explosives etc.[1,2]. The SPR sensor has been widely used for characterization of metal films, affinity analysis, drug screening and sensing etc.[3,4] Although conventional SPR sensor dominates the commercial instrumentation[5-8], the LSPR sensor based on noble metal nanoparticles have some additional advantages, for example, cheap instrumentation, better sensitivity for small molecules, and the flexibility to modify the sensing elements[2,9]. The frequency of the LSRP of noble metal nanoparticles is affected by many factors, including the size, shape, distance and surrounding medium etc.[10,11]. Compared to the refractive index monitoring in SPR, both the changes in distance between nanoparticles and the refractive index of surrounding medium can be used to monitor molecular interaction. I have built

a colorimetric sensor to MMP-7 using peptide functionalized AuNPs by tuning the inter-particle distance between the AuNPs. Presence of MMP-7 results in an aggregation of the AuNPs and a color change from red to blue. This colorimetric sensor enables a quick and easy detection of MMP-7, a cancer marker with the naked eye. In addition, the electromagnetic field around the nanoparticles can be used to enhance the Raman scattering of target/dye molecules, which could also be used to detect target molecules. This Raman scattering contains fingerprint information of the target, which is not available in LSPR sensing graph. I have fabricated a novel Raman substrate based on graphene oxide and Au-Ag alloy nanoparticles, which enable us to detect the Raman scattering from highly fluorescent molecules. With this substrate, the LSPR response and Raman scattering from target molecules can be monitored on the same device, therefore the reliability of the sensor could be improved. One of the limitations of LSPR sensor compared to SPR sensor, however, is the low refractive index sensitivity, which limit its applications in detecting molecules in low concentrations. To increase the refractive index sensitivity, I demonstrated that by assembling simple spherical AuNPs into certain preferred configurations the refractive index sensitivity can be significantly increased. Moreover, I have developed a new LPSR peak evaluation method where the shape of the LSPR peak is used to monitor the molecular interaction. This new method allows a much lower limit of detection as well as higher reliability.

1.2 Motivation

One of the missions of the Centre for Biomimetic Sensor Science (CBSS) is to develop new technology for diagnostic field tests. At CBSS we are particularly interested in developing sensors for targets in the biomedical and environmental sectors e.g. matrilysin, botulinum, glutathione, lipopolysaccharide endotoxins (Endotoxin), MRSA DNA and troponin I etc. The challenges in these areas are huge. First of all the tests must be sensitive enough to enable accurate detection of the analyte "the biomarker" at clinically relevant levels. Even more importantly, they must be robust to withstand harsh experimental conditions and they should possess a sufficiently long shelf life. This is particularly important when developing tests for the developing countries where access to basic lab infrastructure is spare or even non-existent. Other important key characteristics for commercial success of rapid diagnostic field tests are operational simplicity and low costs per tests.

For example, the traditional approach for rapid on-site testing of infectious diseases relies on antibodies as the key recognition elements. Antibodies work beautifully in tests performed in centralized laboratories or when the tests are performed under strictly controlled conditions. However, the inherent temperature instability of antibodies and their short shelf lives have rendered them impractical for on-site testing in tropical/sub-tropical areas where the doctors' offices/field stations often are lacking basic lab infrastructure, like refrigeration. Several commercial malaria tests based on antibody kits therefore have been withdrawn from the market because of variable quality, low reproducibility and a poor

predictive capacity. In addition, the continuous need of resupply of fresh, high quality, antibodies increases rapidly the costs/test.

1.3 Objective

We are at CBSS working on biosensors of various targets for field tests. Briefly, a biosensor for field test must satisfy the following criteria. Firstly, the sensor must be robust enough to withstand the harsh environmental conditions, such as high temperature and extreme pH etc. Secondly, the sensor must be easy to operate and require minimal instrumentation. Thirdly, the response from target molecules must be very reliable and false response/noises from contaminants and instruments must be easily discriminated.

1.4 Hypothesis

Biosensors comprise three major elements: the biological recognition element, the active materials and transducing mechanism. To make the biosensors suitable for field test all the three areas are considered. For example, for the biological element, I choose synthetic peptide other than antibodies as receptors for its excellent stability at extreme pH and temperatures. Similarly, AuNPs and graphene oxide are chosen as active materials for its chemical stability. Transducing mechanisms are also very important. For example, the colorimetric sensing enables a rapid test without instrument, which is very suitable for field test. By optimizing the biological element, active materials, transducing mechanisms and data analysis etc. the biosensors for different targets are designed.

1.5 Materials

The biological materials "recognition molecules" must be robust. We have chosen a concept based on non-natural recognition molecules to replace the fragile antibodies. The molecules of choice are synthetic polypeptides. These molecules can easily be modified with reactive groups for attachment the transducer material. Gold nanoparticles and graphene oxide have been chosen as the transducer materials because of their unique optical properties and the excellent stability. Both gold nanoparticles and graphene are very stable at extreme pH and at elevated temperatures.

1.6 Methods

The combination of synthetic peptides and gold nanoparticles/graphene oxide has been used in the sensor development.[12] These materials display excellent stability at extreme pH and temperatures. For gold nanoparticles, I choose the well-established spherical gold nanoparticles instead of other complicated fancy nanostructures because of reliability concern. Simple spherical gold nanoparticles has the advantages of easy preparation, narrow size distribution, low sample to sample variation etc., which allow us to reduce the chip to chip variation of the sensing response. I believe that sensor based on the simple system is more robust and reliable. However, the spherical gold nanoparticle shows relatively low refractive index sensitivity in comparison to fully optimized lab on a chip system based on more advanced nanostructures. To improve the sensitivity, two different strategies were employed. Firstly, a new peak analysis method based on peak shape has been developed, which allows me to push down the detection limit. Secondly, the effect of configuration of coupled gold nanoparticles was studied.

The sensitivity could be improved significantly by packing the individual nanoparticles into certain configurations/morphologies.

Another general strategy to improve reliability and robustness of the sensor is to allow for multi-parameter sensing. Two independent monitoring mechanisms introduced on a single chip enable us tracking more information from the responses. By analyzing two signals simultaneously, noise could be reduced and differentiated from response from the target molecules. For example, a hybrid sensor that combines plasmonic/colorimetric interrogation and Raman scattering is expected to be more reliable and robust than a sensor relying on one transducer principle. I have demonstrated that Graphene oxide/$Au_{0.7}Ag_{0.3}$ NP is a promising platform for this type of hybrid sensor.

Wet chemical synthesis, self-assembly and some basic surface chemistry were employed to fabricate the desired platform. Microscopy including atomic force microscope and electron microscope, imaging ellipsometry were employed to study the morphology and appearance of the fabricated platform. Spectroscopy including Raman scattering, UV/Vis, Fluorescence, MALDI-TOF, ellipsometry, and DLS have been utilized to characterize the properties and performances of the platform. Classical physical laws such as Maxwell equation, Mie theory, Clausius-Mossotti equation etc. were used to build physical models to explain some of the observed phenomena and improved performance. Mie theory and Finite Difference Time Domain (FDTD) method were used to numerically calculate and simulate the observed phenomena. Some biomarkers of medical relevance, e.g. matrilysin, botulinum, glutathione, lipopolysaccharide endotoxins,

MRSA DNA and troponin I etc. were used as target molecules in the sensor design.

Chapter 2: Literature Review

2.1 Biosensors

A chemical sensor is defined as a self-contained device that is capable of providing real time analytical information about the test samples, e.g. the concentration of one or more species in the sample.[13] The target species is commonly termed as the analyte. Biosensor is a type of chemical sensor in which the recognition system is based on biochemical or biological mechanisms.[13] A biosensor as a sensing device comprised of a specific biological recognition element or receptor and a transducer. The receptor recognizes a specific analyte, while the transducer converts the analyte-receptor interaction into a measurable and readable signal. Two important factors of biosensor are the sensitivity and selectivity. Sensitivity is the slope of the calibration curve i.e. how much does a change of concentration affect the change of receiving signal. Selectivity is the ability of a sensor to measure a concentration of a substance in presence of other interfering substances.

Biosensors provide a quick and cheap alternative way of characterization and analysis as compared to standard analytical methods based on techniques such as spectrometry, chromatography, biochemical or microbiological techniques. In the past few decades, biosensors are developed quickly both in fundamental research and applications. Biosensors are widely explored and used in the areas of medical diagnosis, pharmaceutics and environmental monitoring, as well as food, forensic, sports and defense and military science etc. The surface plasmon resonance (SPR) sensor has been widely used for affinity analysis and drug screening.[3,4] In the

medical and clinical sector, biological markers of various diseases have been detected to assist in diagnosis and treatment.[14,15] In pharmaceutical industry, the endotoxin levels of all injectable drugs and medical products have to be tested. [16,17] In the environmental sector, sensors are focused on the air and water pollution. Toxic gases released by vehicles and industrial production such as sulfur dioxide and nitrogen monoxide[18] and heavy metal ions[19] from industrial waste water such as mercury, lead and cadmium are of significant interest to detect. In food industry, the plasticizer in drinking bottles e.g. bisphenol A[20] and the illegal additives in milk powder e.g. melamine[21] are of huge concern. In forensics science, illegal drugs and biological markers left in the latent fingerprints of suspect criminals are detected to get more information of the criminals.[22] In sports science, every athlete has to undergo the urine test for the stimulants such as hormones and growth factors etc. before important games. [23] In defense and military, detection of explosives e.g. TNT[24] and biological toxins e.g. botulinum[25] are crucial to detect.

Many commercialized sensing platforms have been developed including enzyme-linked immunosorbent assay (ELISA),[26] SPR,[6] quartz crystal microbalance (QCM),[27] and electrochemical sensor[28] etc. Most of these sophisticated sensing platforms are available at test centers, laboratories and hospitals etc. Moreover, these biosensors generally require professional training on operation.

In addition to the above mentioned advanced sensing systems, many simple and portable biosensors/test kits have developed for the purpose of rapid on field testing. This type of biosensor has the advantages of easy to use, quick and

affordable. Many healthcare companies including Roche[29] and Abbot[30] have developed a portable glucose sensor with testing strip for blood glucose monitoring. With this sensor, the glucose level of patients with diabetes could be monitored easily at home. Another example of this type of on field test sensor is the pregnancy test strip, which is virtually a colorimetric sensor based on lateral flow device. Mirkin et al. developed a colorimetric sensor for quick DNA detection using gold nanoparticles.[31] Colorimetric sensors for quick detection of various pathogen infections are developed by Nanosphere using this technology. It is also worthwhile mentioning that some efforts have been made to miniaturize the advanced sensing platform and integrate it into consumable electronics. Filippini et al. has successfully developed a SPR platform using cell phone. [32]

A most ideal biosensor should satisfy/possess the following criteria:

- Robust (high operational reliability)
- High sensitivity
- High selectivity
- Easy to operate
- Label free monitoring
- Real time monitoring
- Multiplexing
- In flow and microfluidics
- Large scale fabrication
- Cheap to produce and operate

Depending on the transducing mechanisms used, sensors can be further divided into many types such as electrochemical sensors[28], fluorescence sensors,[33] QCM sensor,[27] electrical sensors[34] and optical biosensors[6] and enzymatic sensors[35,36] etc.

The enzyme-linked immunosorbent assay (ELISA) was developed based on the independent work of Peter Perlmann and Eva Engvall at Stockholm University in Sweden, and Anton Schuurs and Bauke van Weemen in the Netherlands in 1971.[36,37] ELISA is a "wet lab" analytical biochemistry assay, which could detect target molecules quantitatively and qualitatively based on color changes. ELISA use antibody linked enzymes to catalyze the oxidation of substrate e.g. ABTS to give color changes. Until now, it is one of the most established and widely used sensors. ELISA provides a very sensitive assay, yet it is a slow and labor intensive technique.

The surface plasmon resonance (SPR) sensor was first demonstrated in 1983 by Bo Liedberg et al. at Linköping university.[5,6] Since then SPR sensing has been receiving continuously growing attention from scientific community as well as industry.[3] It has been widely used for characterization of thin films, and for gas detection,[8] drug discovery[4] and bioassay.[7] The SPR sensor was developed into an established commercial tool for by Biacore,[38] which was later acquired by GE healthcare. The configuration of a SPR sensor setup is illustrated in Figure 2.1.

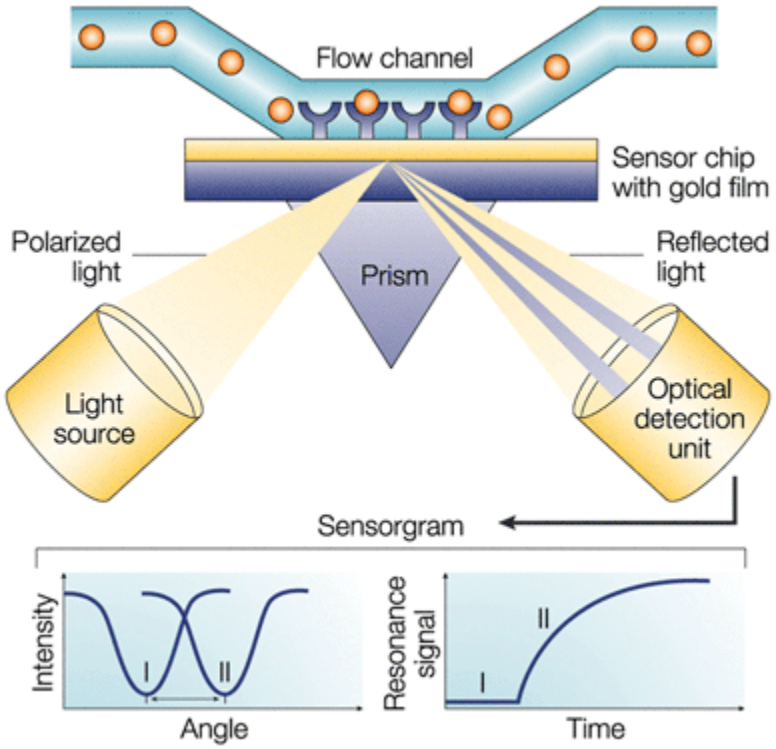

Figure 2.1 A typical SPR sensor setup consists of a sensor chip, a flow system and an optical detection system. Adapted by permission from Macmillan Publishers Ltd: Nature Reviews Drug Discovery with ref. [4] copyright©2002.

Surface plasmon is the oscillation of free electrons at the metal dielectric interface. The resonance angle and intensity of the surface plasmon (signal) at the metal dielectric interface is dependent on the refractive index of the bounding medium. The SPR sensor chip is modified with receptor molecules and the binding of target results in a change in refractive index at the interface, which could be monitored as shift in resonance angle and intensity of the resonance signal over time.

Recently, long-range surface plasmon resonance (LRSPR) is explored as a powerful biosensing technology.[39,40] It has substantially larger probing depth into

the medium compared with conventional SPR. The LRSPR sensor has similar sensitivity but much smaller SPR dip width than the SPR sensor. Thus figure of merit of the sensor (sensitivity/width) can be enhanced ~five times. The LRSPR sensor enables detection with higher resolution.

2.2 Localized surface plasmon resonance

Localized surface plasmon resonance (LSPR) is one of the most interesting phenomena occurring in the surface of gold nanostructures. When an electromagnetic radiation of an appropriate wavelength illuminates a gold nanostructure, the delocalised conduction electrons of the metal will begin to oscillate collectively relative to the lattice of positive nuclei with the frequency of the incoming light.[41] Figure 2.2 demonstrates this phenomenon for a gold nanoparticle. When light is illuminated on the particle, two types of interactions occur namely scattering and absorption. In the scattering process the incoming light is re-radiated in all directions at the same wavelength while in the absorption process, the energy is absorbed and converted into vibrations of the lattice (i.e. phonons). Together, these two processes are referred as extinction (extinction = absorption + scattering). When the frequency of light matches with the intrinsic frequency of the nanoparticle a resonance condition will occur, which is localized surface plasmon resonance. The resonance creates very strong localized electromagnetic field near the surface of the particle, which is widely explored for surface enhanced Raman scattering (SERS)[42] and enhanced fluorescence.[43] The resonance frequency/wavelength of plasmonic nanoparticles depends on many factors including size, shape, composition, inter-particle distance and medium

etc.[44] The LSPR peak shift induced by molecular binding[45] and aggregation[31] is therefore widely used to detect various biological target molecules.

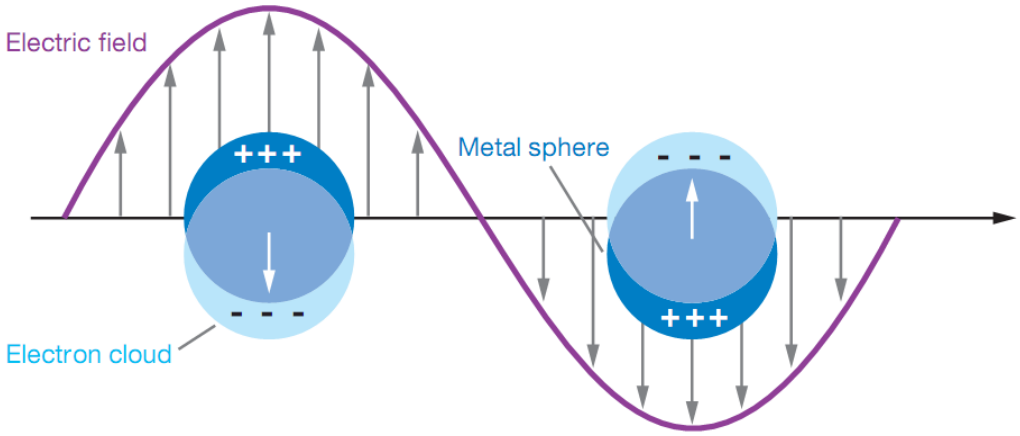

Figure 2.2 Illustration of the localized surface plasmon resonance. Free electrons in metal spheres oscillate with the electromagnetic (EM) filed. When the frequency of EM filed matches with the intrinsic frequency of metal sphere, a resonance occurs. Reprinted with permission from ref.[2] Copyright © 2007, Annual Reviews.

Compared to planar SPR, localized surface plasmon resonance (LSPR) of gold nanoparticles does not require expensive setup. In addition, the SPR has a larger extension of the evanescent field (probe depth) up to 200 nm, while the electromagnetic field in LSPR sensor is localized to the surface of particle with the probe depth of similar magnitude as the diameter of the nanoparticles. This difference makes the LSPR sensor very suitable for the detection of small molecules.[1,45,46] The LSPR sensors can be designed in many ways by monitoring the changes in refractive index[46], distance between particles[47] or surface enhanced Raman scattering[48].

The resonance frequency and electromagnetic field around a plasmonic nanoparticle can be calculated theoretically using Maxwell's equation with proper initial conditions and boundary conditions. For a spherical particle the Maxwell's equation is analytically solvable, which was first reported by Gustav Mie in 1908,[49] and further developed by Bohren and Huffman.[50] The absorption and scattering cross sections of a spherical particle can be calculated from Mie theory and their relation is shown in Eq.(2.1). For nanoparticle with other geometry, however, analytical solution of the Maxwell's equation is not possible. Two methods of numerical calculations are available for nanoparticles with arbitrary geometry, namely the discrete dipole approximation (DDA) method[51] and finite difference time domain (FDTD) method. [52] The DDA method can be implemented using an open source code, while the FDTD method can be performed using a commercial package from Lumerical solutions.

For spherical nanoparticles, both the absorption and scattering cross sections vary with the diameter *D* of the particle. While the absorption cross section scales with D^3 the scattering cross section scales with D^6. For particles smaller than 30 nm the contribution from scattering is much smaller than from absorption. Thus, the extinction cross section is approximately equivalent with the absorption cross section.

$$\sigma_{abs} = \frac{9V\varepsilon_m^{3/2}}{c}\frac{\omega\varepsilon_2(\omega)}{[\varepsilon_1(\omega)+2\varepsilon_m]^2+\varepsilon_2(\omega)^2} \qquad (2.1)$$

where, ω is the angular frequency of light, *V* is the volume of particle, *c* is the speed of light, ε_m is the real part of the permittivity of surrounding medium and

$\varepsilon_1(\omega)$, $\varepsilon_2(\omega)$ are the angular frequency dependent real and imaginary parts of the dielectric function, respectively.

The experimentally measured bulk dielectric function of gold by Johnson and Christy in 1972[53] is considered to be the most reliable one, and it is widely used in theoretical calculations. However, when the size of particle is reduced and becomes comparable to the mean free path of free electrons (~10 nm), the bulk dielectric function has to be modified to account for additional damping from the surface.[54] The size dependent phenomenological damping constant can be written as

$$\gamma(D) = \gamma_0 + 2\frac{Av_F}{D} \qquad (2.2)$$

where $\gamma_0$is bulk damping rate, D the diameter of particle, v_F the Fermi velocity of electrons. The dimension less constant A is experimentally determined to be 0.25.[54] The size dependent dielectric function[55] is described by

$$\varepsilon(\omega, D) = \varepsilon_{IB}(\omega) + 1 - \frac{\Omega_p^2}{\omega^2 + i\omega\gamma(D)} \qquad (2.3)$$

where Ω_p is the bulk plasma frequency, $\varepsilon_{IB}(\omega)$ is size independent term. The latter part is the Drude free electron term, which depends on the damping constant. For gold, v_F =1.4×10^{15} nm/s, $\hbar\gamma_0$ = 70 meV and $\hbar\Omega_p$ = 9.0 eV.

2.3 Effect of Shapes and Coupling

Nanostructures with anisotropic structures e.g. gold nanorods demonstrate different plasmonic properties from the isotropic spherical nanoparticles. Briefly, gold nanorods show two distinct LSPR peak, corresponding to the longitudinal

and transverse modes, respectively. The frequency of the two peaks is related to the size and aspect ratio of the rod. Both LSPR peaks can be used in sensing, however, the longitudinal mode was most widely used for its better refractive index sensitivity.[56] The sensitivity of longitudinal mode is also much better compared to that of spherical AuNPs. Other nanostructures with higher polarizability such as nanostars,[57] nanoshells[58], mushrooms[59], nanorings[60] and nanotriangles[61] etc are also widely explored for their better sensitivity.

In addition, the plasmonic property of AuNPs is influenced strongly by the coupling from neighboring AuNPs. Generally, when the AuNPs are brought into a close proximity of the size of AuNPs, coupling effect from neighboring AuNPs is very prominent. The plasmonic coupling induces a significant red shift of the LSPR peak. The significant shift of LSPR peak is able to be seen from the color changes by the naked eye. [44] Chad Mirkin et al. demonstrated the color of gold nanoparticles (AuNPs) could be tuned from red to blue by triggering the aggregation of AuNPs with complementary DNAs in 1996[62] and developed the first colorimetric sensor for DNAs in 1997.[31] Compared to other sensors, it allows a simple detection and eliminates the necessity of expensive instruments. Since its discovery, the aggregation of AuNPs has attracted significant research interest[63,64] and AuNP based colorimetric sensors have been developed rapidly and widely used for the detection of target molecules in the field of medical diagnosis,[65] pharmaceutics,[66] environmental monitoring,[67] food safety,[68] and military[69] etc. One mechanism to induce the aggregation of AuNPs involves using cross-linking molecules, such as complementary DNAs,[31] peptides[70] and

aptamer[71] etc. that bind to multiple AuNPs. This mechanism is widely used for detection of DNAs,[31,72] proteins,[47,73,74] metal ions,[67,75] enzymatic activity[76-78] etc. Another way to induce the aggregation involves reducing the repulsive force that keeps the AuNPs stable.[63] This mechanism is also widely used for detecting many target molecules[79-81] and enzymatic activity.[12]

In addition to the color changes, the refractive index sensitivity of the coupling induced peak is also improved compared to the individual particles. El-sayed et al. demonstrated that with simulation that the coupling between two nanoparticles could improve the refractive index sensitivity, which is exponentially related to the inter-particle distance.[82] Naomi Halas et al. studied the refractive index sensitivity of a different coupling (Fano Resonance) theoretically and experimentally.[83,84] The fano resonance demonstrated a much better sensitivity and also sharper peak compared to the LSPR peak of individual particles. Alternatively, physicists also explored the coupling of novel sub-micron plasmonic patterns using lithography techniques,[85-87] which is mostly known as meta-materials.

2.4 Synthesis of gold nanoparticles

Gold nanoparticles with different morphologies have attracted considerable interests in biomedical applications.[88] The resonance frequency and electromagnetic field of plasmonic nanostructure depends strongly on the shape.[44] Typical nanostructures of interest in biosensing include nanospheres,[89] nanorods,[90,91] nanoshells,[58] nanocube,[92] nanostars,[93] pyramid[94] nanodisk and bimetallic nanoparticles[95,96] etc. These nanostructures can be synthesized using

wet chemical methods,[97] as well lithography methods.[98] There are generally four protocols for the wet chemical synthesis of these structures: direct reduction, seed mediated approach, templated methods and co-reduction.

Different nanostructures have different properties. Generally, silver nanoparticles have better sensitivity than gold, but poor chemical stability.[99] Some gold nanostructures, such as gold nanorods also have better refractive index sensitivity than the spherical particle, however, they are capped with some surfactant (CTAB), which make them very difficult to modify with biological molecules.[100] In addition, other type of complicated gold nanostructures may also have advantages in sensitivity, but also different other problems, such as the complicated process and large variation in the shape and size etc. All these problems results in a large variation and low repeatability of LSPR sensor. On the other hand, gold spherical nanoparticles with uniform size and shape can be synthesized easily with sodium citrate as capping layer. They are very stable and easy to modify with the standard thiol-gold chemistry. Gold nanospheres can be synthesized by direct reduction of gold salt to produce particles of various sizes and of high uniformity[89,101]. In a typical reaction, dissolved gold salt ions (such as $HAuCl_4$) (Au^{3+}) are reduced to gold atoms (Au) in the presence of a capping agent or surfactant to prevent aggregation. In the most commonly used method, sodium citrate is used as both the reducing agent and capping agent. The size of the nanoparticles can be tuned by changing the ratio of the gold ions to reducing agent. Depending on the size of the gold particle, strong extinction occurs between 500 and 600 nm. Nanorod, nanocube and other structures with

anisotropic properties are typically synthesized by a seed-mediated, solution-phase method. Typically seeds with a size of 3-5 nm were first synthesized by reducing gold ions using sodium borohydride. The preformed small gold seeds are added to a series of growth solutions containing gold ions and surfactants. By adjusting the concentrations and type of reagents and the size of the initial gold seeds, it is possible to obtain different gold nanostructures[97,102]. Nanostructures with cavities such as nanoshell, nanocages are typically synthesized by templated method[58]. With this method, gold nanoshells and nanocages can be created by hollowing out the interior of a sacrificial template of silver nanoparticles or nanocubes. Depending on the shape of the silver template, other gold nanostructures with hollow interiors can also be formed. Bimetallic nanoparticles can be obtained by reducing two different metal ions simultaneously.[92,95] Gold-silver alloy nanoparticles with different ratios were synthesized by co-reduction of gold and silver salt in sodium citrate solution[103]. Noble metal nanostructures of various shapes that can be synthesized with wet chemistry are summarized in Table 2.1.[97]

Table 2.1 summary of nanostructures of various metals have been synthesized. Reprinted with permission from ref. [97] Copyright © 2009 WILEY-VCH Verlag GmbH & Co. KGaA, Weinheim.

Structures	Shapes	Schematic drawings	Metals
single-crystal	perfect/truncated cube[a]		Pd, Ag, Au, Pt, Cu, Rh, Bi, Fe
	perfect/truncated octahedron[a]		Pd, Ag, Au, Pt
	perfect/truncated tetrahedron[a]		Ag, Au, Pt, Rh
	rectangular bar		Pd, Ag, Pt
	octagonal rod		Pd, Au, Fe, Co, Ni
	rectangular or octagonal wire		Pb, In, Sn, Sb, Fe, Co
singly twinned	right bipyramid		Pd, Ag
	beam		Ag
multiply twinned	decahedron[a]		Pd, Ag, Au
	icosahedron[a]		Pd, Au
	five-fold twinned pentagonal rod		Pd, Ag, Au, Cu
	five-fold twinned pentagonal wire	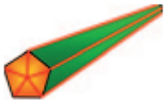	Ag, Au, Cu
	triangular/hexagonal plate		Pd, Ag, Au, Cu, Pb, Bi, Co, Ni
	disc		Sn, Co

2.5 Refractive Index Sensing

The resonance frequency/wavelength of AuNPs depends on the refractive index of surrounding medium.[41] The absorbance of the AuNPs can be described by Mie theory, see Eq. 2.1.

The resonance conditions occur when,

$\varepsilon_1(\lambda) = -2\varepsilon_m$ (2.4)

The permittivity of surrounding medium is related to refractive index (n) through,

$\varepsilon_m = n^2$ (2.5).

It is therefore obvious that the peak wavelength of the LSPR peak of AuNPs depends on the refractive index of surrounding medium. A typical refractive index sensor is illustrated below in Figure 2.3.[1]

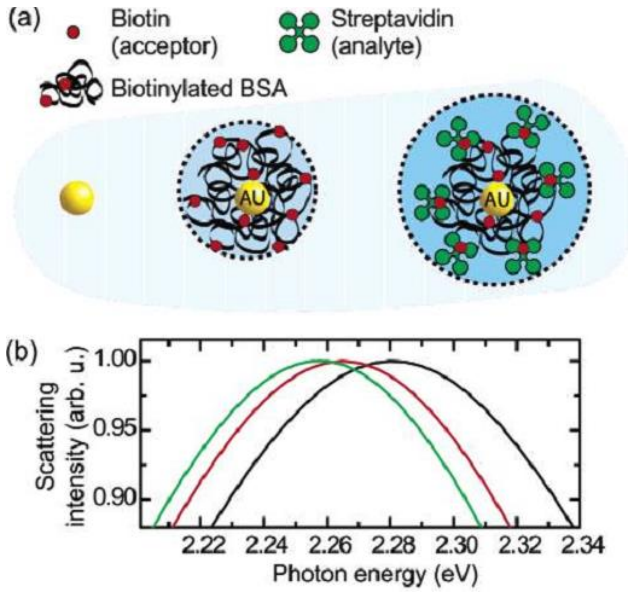

Figure 2.3 (a) Configuration of a refractive index sensor for streptavidin based on AuNPs (b) Response of resonance energy with receptor and target molecules. Adapted with permission from ref.[1] Copyright ©2003 American Chemical Society.

Receptor molecules (biotin) with specific binding site of the target molecule (streptavidin) were first immobilized on the AuNPs. The binding of target molecule to the AuNPs changes the refractive index of the surrounding medium, which results in the red shift of LSPR peak. The peak shift and extinction at peak maximum induced by the binding were used to monitor the presence and quantity of target molecules. The LSPR refractive index sensors can be fabricated into chips and the detection of molecular binding is similar to that of planar SPR.

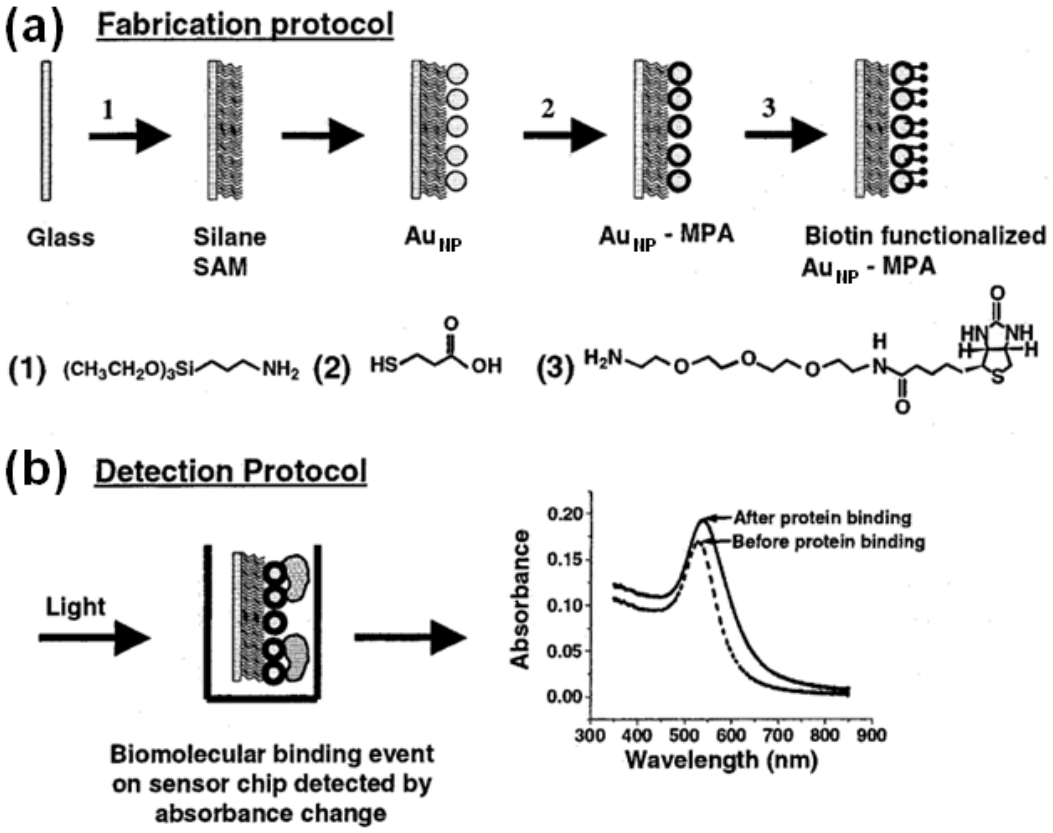

Figure 2.4 (a) Fabrication protocol of LSPR sensor (b) Detection principle of LSPR sensor. Adapted with permission from ref.[45] Copyright ©2003 American Chemical Society.

Figure 2.4 shows the fabrication protocol of a LSPR sensor by assembling AuNPs onto glass slide followed by surface functionalization. The molecular binding to receptor molecules induces an increase in the peak absorbance as well as a red shift of the spectrum. [45,46]

The absorption spectra of the LSPR sensor after addition of 10 μg/mL fibrinogen and 100 μg/mL fibrinogen are shown in Figure 2.5 (a). The real time adsorption of fibrinogen with different concentrations to the biotin functionalized AuNPs is shown in Figure 2.5 (b).

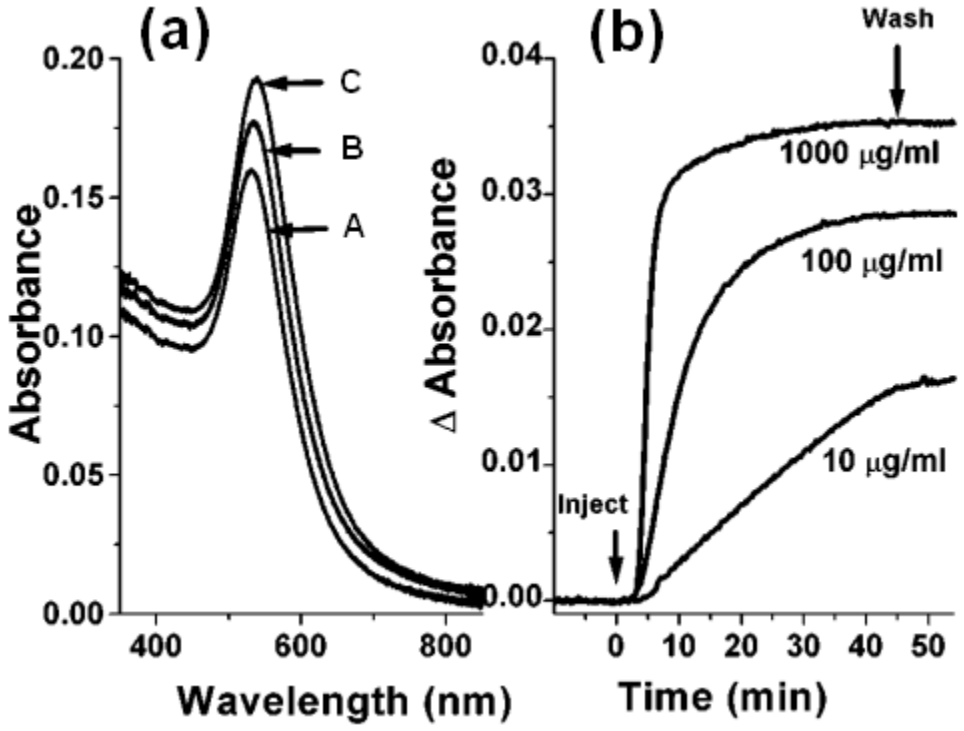

Figure 2.5 (a) Absorption spectra of biotin functionalized AuNPs after addition of 0 μg/mL (A), 10 μg/mL (B) and 100 μg/mL fibrinogen (C), respectively. (b) Changes in absorbance at 550 nm as a function of time with the adsorption of fibrinogen. Adapted with permission from ref.[45] Copyright ©2003 American Chemical Society.

The refractive index sensitivity of the LSPR sensor is characterized by the peak shift induced by one refractive index unit (nm/RIU). The sensitivity varies a lot with the size and shape of the nanoparticles. Generally nanostructures with higher polarizability show higher sensitivity.[82] The refractive index sensitivity of some nanostructures is summarized in Table 2.2.

Table 2.2 Summary of the refractive index sensitivity of various nanostructures

Nanostructures	**Refractive index sensitivity (nm/RIU)**
AuNPs 15 nm	44[93]
AuNPs 50 nm	60[104]
Ag Triangle	200[105,106]
Au Nanorod (aspect ratio 2.4)	195[93]
Au Nanorod (aspect ratio 3)	400[107]
Au Nanoshell 50 nm	400[104]
Bipyramid	540[93]
Branches	703[93]
Au Nanostar	218[108]
Au coated silver prism	425[109]
Au Nanocube	161[110]
Au Nanobars	339[110]

In addition to the shape of the nanostructures, it was also reported that the coupling between nanoparticles could also enhance the refractive index sensitivity. El-Sayed et al. demonstrated with a AuNP dimer that the sensitivity increases exponentially with the decreasing inter-particle distance.[82] For a 40 nm AuNP dimer, the sensitivity could be increased from 77 nm/RIU to 172 nm by decreasing the inter-particle distance to 4 nm. Takumi et al. demonstrated using coupled nanoparticle array that the sensitivity can be increased to ~170 nm/RIU from ~30 nm/RIU.[111] Liu et al. demonstrated with a coupled nanoring structure that the refractive index sensitivity can be as high as 1200 nm/RIU.[112]

2.6 Colorimetric Sensing

Compared to other types of sensors, colorimetric sensor does not require any sophisticated equipment. The response is simply changes in colors, which sometimes can be read by the naked eyes. Therefore, the detection method is very easy to operate for people without professional training. In addition, the plasmonic nanoparticles based colorimetric assay can be very quick and cheap. As a result, the colorimetric sensor is an attractive assay for applications in regions with limited resources. It is also a promising assay for field test where instrument is not easily accessed. Even for central laboratories/hospitals where a lot of facilities are available, the colorimetric assay is also a complementary technique. It can be used as a quick test or prescreening assay before more advanced and expensive test. There are many types of colorimetric assay formats developed, such as plasmonic nanoparticles based colorimetric assay[31] and fluorescence based colorimetric assay.[113]

The plasmonic nanoparticles based colorimetric assay utilizes typically the phenomenon of the inter-particle distance dependent surface plasmon resonance. The LSPR peak wavelength of AuNPs is influenced by the inter-particle distance between them[114-116]. Compared to refractive index, the LSPR peak shift is much more sensitive to the inter-particle distance, therefore by tuning the distance the peak shift could be large enough to be seen by the naked eye.[31,47] Controlled aggregation of AuNPs by chemical/biological molecules provides an easy way to tune the inter-particle distance and it is widely used in colorimetric sensing. The aggregation of AuNPs is characterized by a red to blue color transition. Mirkin et

al. reported the first colorimetric sensors using the controlled aggregation of AuNPs by complementary DNAs.[31] The principle of the colorimetric sensor is illustrated in Figure 2.6.

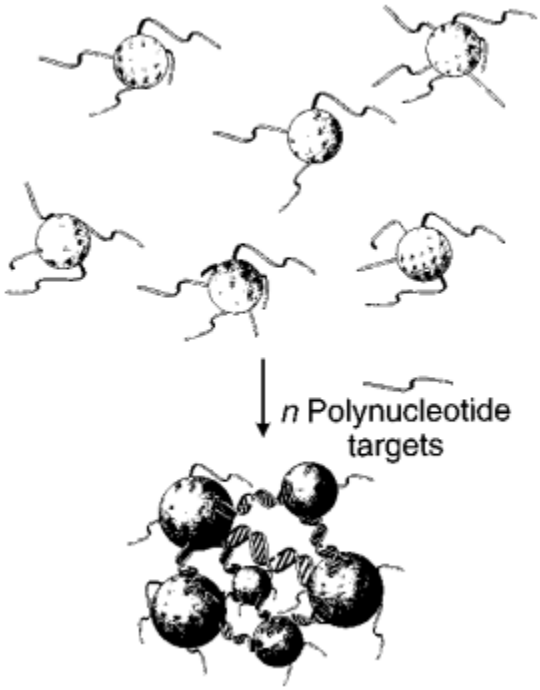

Figure 2.6 Illustration of the colorimetric sensor for DNA. AuNPs are functionalized with probe DNAs which keep the AuNPs stable and dispersed. The target DNA could bind to 2 probe DNAs, resulting in aggregation of the AuNPs. Reprinted with permission from ref.[31] Copyright © 1997, American Association for the Advancement of Science.

Since the first report of the colorimetric sensor using controlled aggregation, tremendous research work has been done on both fundamental study as well as sensors for different targets. Liedberg et al. use synthetic complementary peptides to control the aggregation of AuNPs.[117] Su et al. developed a colorimetric sensor for Pb^{2+} using reduced glutathione functionalized AuNPs.[118] Xu et al. developed a colorimetric assay for melamine.[119] Zare et al. developed the colorimetric assay to

study the protein conformational changes.[120] Stevens et al. developed a colorimetric sensor for blood coagulation Factor XIII activity using peptide functionalized AuNPs.[77] Feng et al. developed a sensor for cadmium(II) (Cd^{2+}) using AuNPs functionalized with 4-amino-3-hydrazino-5-mercapto-1,2,4-triazole.[19] A photo image of the AuNPs with different concentrations of Cd^{2+} is shown in Figure 2.7. It is very obvious that the color changes can be used quantitatively detect the concentration of Cd^{2+}.

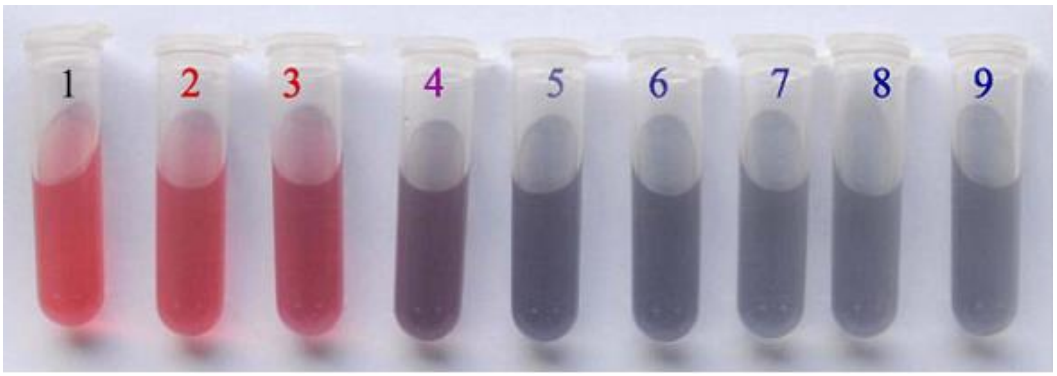

Figure 2.7 The concentrations of Cd^{2+} in tubes 1 to 9 are 0, 0.06, 0.12, 0.18, 0.24, 0.30, 0.36, 0.42, and 0.48 μM, respectively. Reprinted with permission from ref.[19] Copyright © 2013, Springer-Verlag Wien.

In addition to controlled aggregation of AuNPs, a few research groups also explored the induced dispersion of pre-aggregated AuNPs. Stevens et al. demonstrated a very sensitive assay for a-antichymotrypsin prostate specific antigen (nACT-PSA) based on the re-dispersion of AuNPs upon the hydrolysis of an immobilized oligopeptide.[121] On the contrast to controlled aggregation, the re-dispersion of aggregated AuNPs results in a color change from blue to red. The principle of this type of colorimetric sensor is illustrated in Figure 2.8.

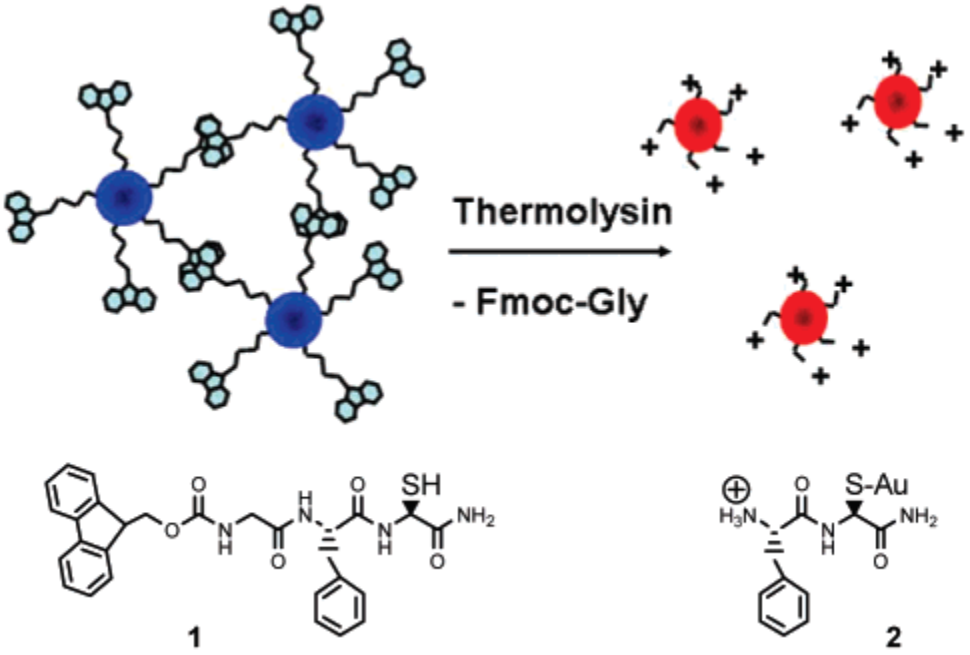

Figure 2.8 Illustration of the protease triggered dispersion of aggregated AuNPs. 1: intact oligopeptide and 2: digested oligopeptide. Reprinted with permission from ref.[121] Copyright © 2007, American Chemical Society.

In addition to the plasmonic nanoparticles based colorimetric assay, fluorescence is also used for colorimetric sensing. The fluorescence assay can be categorized into two categories, the fluorescence turn on sensor and the fluorescence turn off sensor. A typical fluorescence turn on sensor utilized a fluorescence dye and fluorescence quencher, where the fluorescence is quenched initially and restored when target molecules are present. Commonly used fluorescence quenching materials include Noble metal nanoparticles,[122] carbon nanotubes[123] and graphene[33] etc. Figure 2.9 shows a typical fluorescence sensor for protein using AuNPs as fluorescence quencher. The AuNPs are firstly functionalized with receptor molecules and on which polymer dyes are physically adsorbed. The

fluorescence of the polymer dye is quenched by the AuNP. The binding of protein to the receptor molecules replace the polymer dyes and release them from the AuNP, which in turn increases the fluorescence and color.

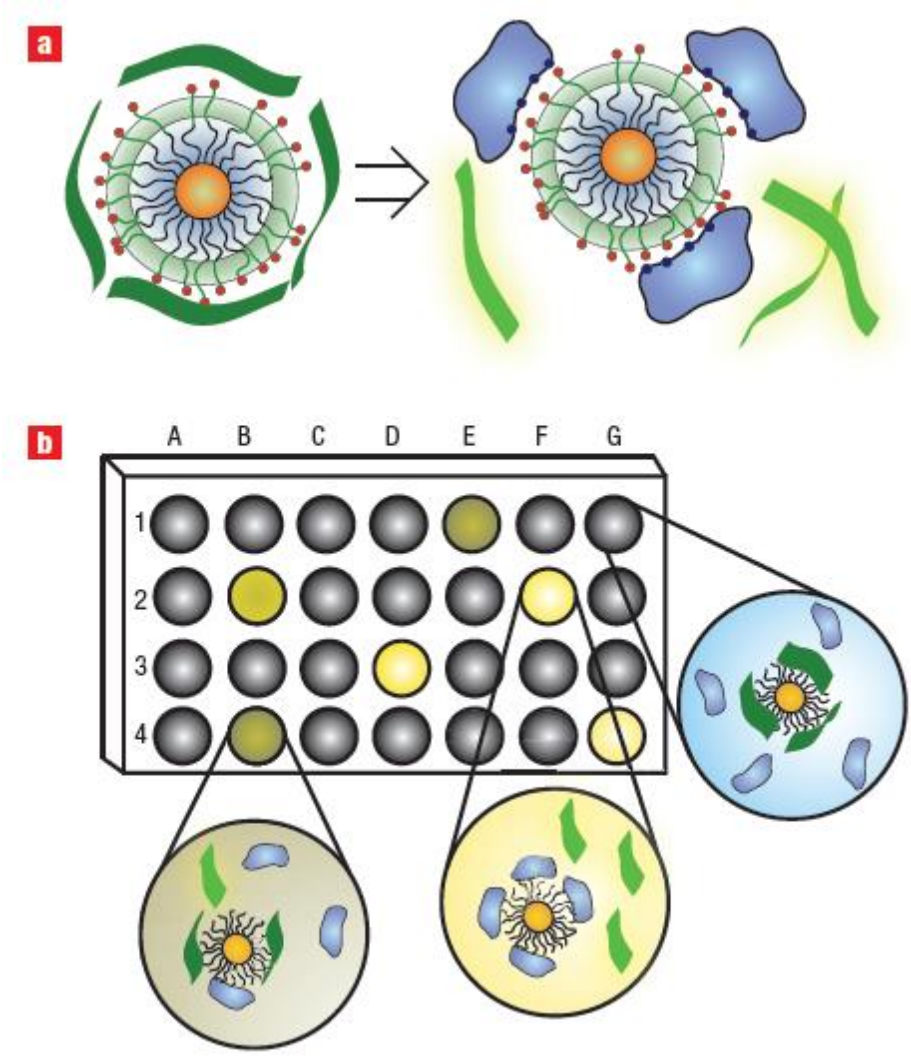

Figure 2.9 Illustration of the working principle of the colorimetric sensor. (a) Displacement of polymer dyes by protein increase the fluorescence of the dye. (b) Fluorescence pattern generation by protein adsorption to AuNPs with different polymer dyes conjugates. Reprinted with permission from ref.[122] Copyright © 2007, Rights Managed by Nature Publishing Group.

In addition to AuNPs, graphene is also widely used in fluorescence turn on sensor for its super fluorescence quenching property. Lu et al. demonstrated the graphene based fluorescence turn on platform for DNA detection, Figure 2.10. [33] Briefly, the dye labeled single strand DNAs were firstly attached to graphene oxide through electrostatic attraction. The fluorescence of dyes is completely quenched by the graphene oxide (off state). The hybridization with complementary DNAs release the dye labeled DNAs from the graphene oxide surface, resulting in an increase of fluorescence (on state). The graphene based platform is widely explored for sensors of different target molecules ranging from protein,[124] metal ions,[125] enzymatic activity[126] etc.

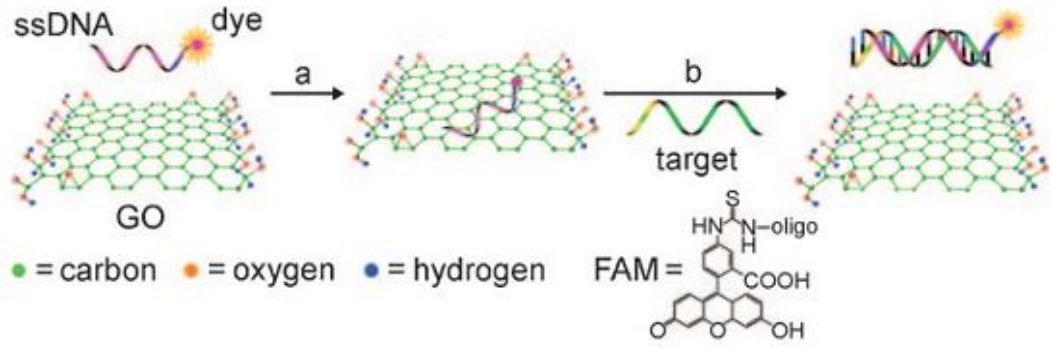

Figure 2.10 Illustration of the principle of detection of DNA. Dye labeled probe DNA is physically adsorbed on the GO surface, where the fluorescence of dye is quenched by GO. Hybridization of target DNA release the dye labeled probe DNA from the GO surface and the fluorescence recovers. Reprinted with permission from ref.[33]Copyright © 2009 WILEY-VCH Verlag GmbH & Co. KGaA, Weinheim.

2.7 Surface enhanced Raman scattering based biosensors

Raman scattering was discovered by Sir C. V. Raman in 1928.[127] Since then it is developed into a useful spectroscopic tool to observe vibrational, rotational, and

other low-frequency modes in molecules. It relies on inelastic scattering of monochromatic light, usually from a laser in the UV, visible, and near infrared range. The laser light interacts with molecular vibrations or phonons resulting in the shift of the energy of the laser photons. The shift in energy gives fingerprint of the vibrational modes of the particular system. It is similar to infrared absorption spectroscopy but gives complementary information. Different scattering and absorption process is illustrated with vibrational levels in Figure 2.11. In a typical measurement, the sample is illuminated with a laser beam. Scattered light is collected with a lens and sent through a monochromator. The elastic Rayleigh scattering is filtered out while the rest of the collected light is dispersed onto a detector. Spontaneous Raman scattering is generally very weak, and the main difficulty of Raman spectroscopy is separating the weak inelastically scattered light from the intense Rayleigh scattering and fluorescence.

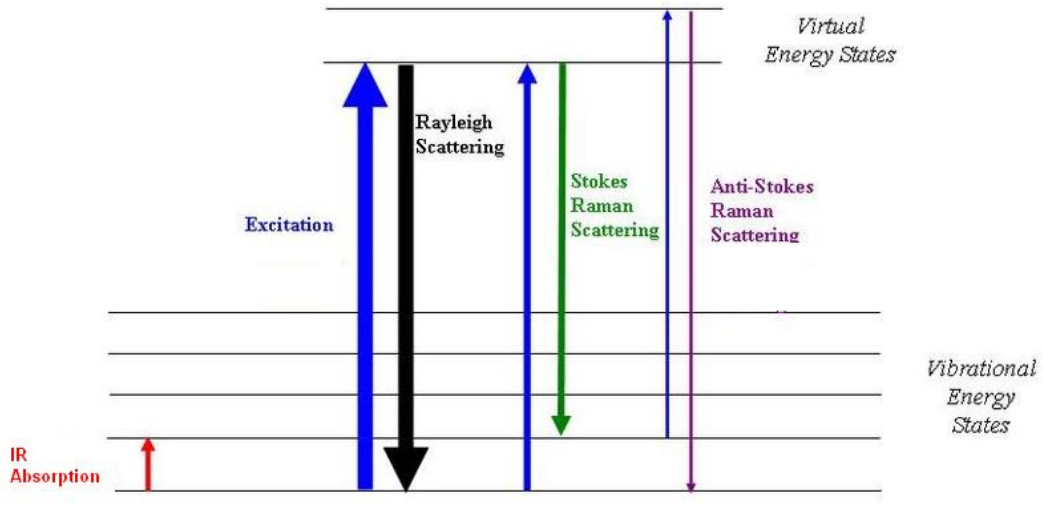

Figure 2.11 Illustration of Raman scattering, Rayleigh scattering, IR absorption and energy levels.

Surface enhanced Raman scattering (SERS) was discovered by Fleischmann et al. accidently in 1974[128] when they observed intense Raman scattering from pyridine adsorbed onto a roughened silver electrode. The rational to roughen the electrode is to increase its surface area and thus the number of molecules adsorbed. This silver electrode did enhance the Raman scattering significantly, although the enhancement is not mainly due to the increasing number of adsorbed molecules. Jeanmaire and Van Duyne tentatively proposed an electric field enhancement mechanism in 1977,[129] where the Raman scattering is enhanced by the local electromagnetic field of the plasmonic nanostructures. Raman cross section of ordinary molecules is very small ~10^{-30} cm^2, without enhancement it is almost impossible to detect the Raman scattering. In the past few decades, tremendous attempt has been put to develop surface enhanced Raman scattering (SERS) substrate. Different metal nanostructures were explored as substrates to enhance Raman scattering, such as nanogaps, triangles, dimers, nanorods, nanorices, nanoshells, nanorings, nanocrescents, nanostars, and nanoflowers etc.[130-136] The enhancement factor of silver particle can be as high as 10^{14} to 10^{15} and the detection of single molecules is possible.[137]

Electromagnetic enhancement in theory should be the same for Raman scattering of all molecules adsorbed on the same particle, however, the molecules CO and N_2 differ by a factor of 200 in SERS intensities under the same experimental conditions. This observation leads to another mechanism of Raman enhancement, namely chemical enhancement. Chemical enhancement theory suggest that new electronic states form from chemi-sorption serve as resonant intermediate states,

which possess higher cross section of Raman scattering.[138] Later it was found that graphene which is not plasmonic active in the visible range also could enhance the Raman scattering by chemical enhancement mechanism.[139]

The SERS effect of noble metal particles are widely used in biological sensing. Mirkin et al. developed a SERS platform based on for DNAs, Figure 2.12[48]. Briefly, one of the probe DNA was first immobilized on substrate, while the other one labeled with Raman dye was immobilized on AgNPs. Target DNA, which is complementary to both of the probes when introduced to the sensor could bring the AgNPs onto the substrate. The Raman scattering of the labeled dye was then monitored. The intensity of the Raman characteristic peak of the dye could be used to quantitatively study the concentration of target molecules. It is worthwhile to note that in this sensor, the dye cy3 is used as Raman tags because of its higher Raman cross section. Normal biological molecules have much smaller Raman cross section.

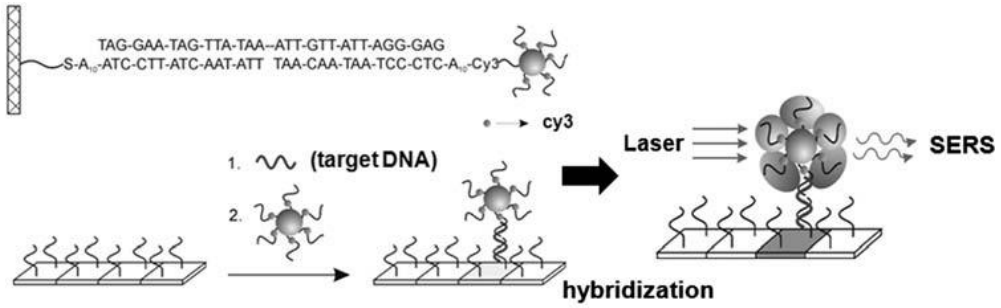

Figure 2.12 A sensor for DNAs by characterizing SERS response. Probe DNA is first immobilized on the substrate to allow target DNA hybridization. A second DNA which could bind to the target DNA is labeled with dyes and immobilized on AuNPs (AuNP-DNA-dye). The intensity of SERS spectrum from the AuNP-DNA-dye is used to monitor the concentration of target DNA. Reprinted with permission from ref.[48] Copyright © 2002, American Association for the Advancement of Science.

Common biological molecules such as proteins and DNAs/RNAs are also Raman active. There are 20 natural amino acids in proteins, of which the phenylalanine, tryptophan, histidine, alanine, leucine and tyrosine are Raman active.[140-142] All the fives nucleotides consist of DNAs/RNAs, adenine, guanine, thymine, cytosine and uracil are Raman active.[143,144] Many chemicals like drugs (cocaine), explosives (TNT) also have their unique Raman characteristic peaks. In principle, it is therefore possible to detect these target molecules directly using SERS. Bell et al. developed a direct label free SERS platform for deoxyadenosine - monophosphate (dAMP) using aggregated AgNPs.[143] The SERS spectra of different concentrations of dAMP as well as the calibration curve are shown in Figure 2.13. The detection limit using this platform is 3 ppb.

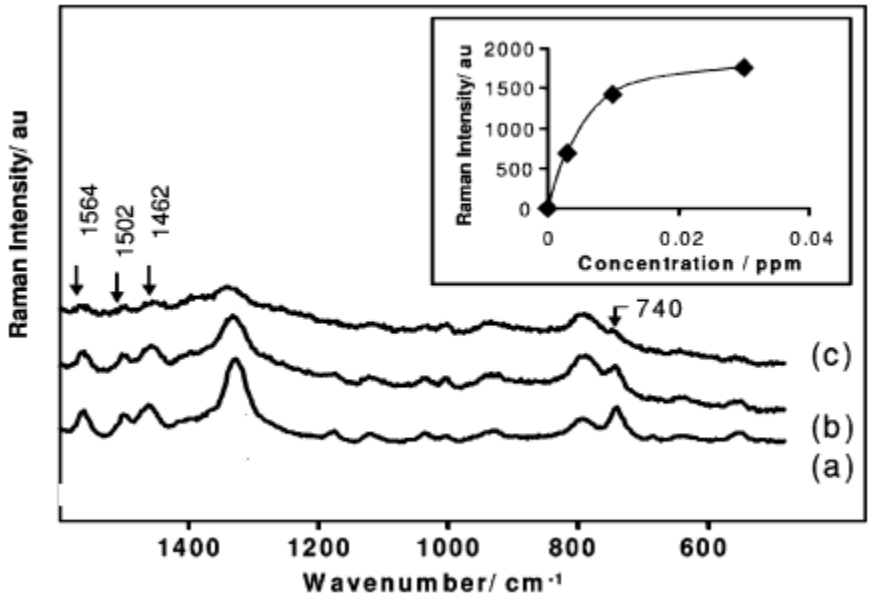

Figure 2.13 SERS spectra of dAMP of different concentrations: (a)0.03 (b) 0.01 (c) 0.001 ppm. Inset shows the calibration curve. Reprinted with permission from ref.[143] Copyright © 2006, American Chemical Society.

2.8 Evaluation of LSPR peaks

As have discussed previously in section 2.4 and 2.5, the LSPR peak shift with refractive index and inter-particle distances. Peak shift is widely used to track the response from molecular binding and aggregation.[25,45,145] In real detection, however, the minute shift induced by molecular binding is difficult to monitor, especially for molecules with low molecular weight. The problem is partly due to the poor resolution of peak position due to the equipment. Another source of noise may also come from the chemical variation of the sample. Other parameters besides peak shift have been explored to improve the signal-to-noise ratio.

Nath et al. reported that extinction is better than peak position to track the binding of proteins due to its smaller noise.[45] Höök et al. demonstrated that by fitting the absorption spectra with polynomial function, the noise of extinction could be further reduced.[146] Höök et al. further demonstrate that the centroid (center of gravity) of the fitted absorption spectra shows even smaller noise. This method offers a precision in measuring LSPR shifts of 5×10^{-4} nm for bulk ensemble measurements. The total experimental peak uncertainty also comes from instrumental factors including spectrometer resolution, microscope focus control, and physical stability and analytical factors as well as sample variations. With nanorod and dark field microscopy system a total uncertainty in peak shift of ~0.3 nm was achieved using this method. [56]

On the other hand, aggregation of AuNPs induces a significant broadening of peak due to the variations in different aggregated states. The broadening of LSPR peak makes the determination of peak position very difficult. Stevens et al. use

the A/D ratio to study the aggregation of AuNPs induced by peptide.[64] In the particular study, the A/D ratio is defined as the ratio of the integrals from 550 to 700 nm and 490 to 540 nm. The calculation of A/D ratio is illustrated in Figure 2.14.

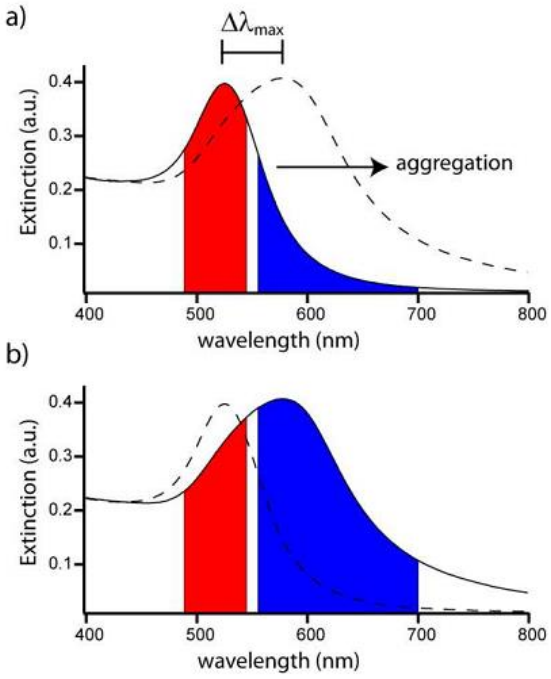

Figure 2.14 The area in red is denoted D (dispersed) which is the integration from 490 to 540 nm. The area in blue is denoted A (aggregated) which is the integration from 550 to 700 nm. The spectra in a) and b) show the change in the A/D ratio for dispersed and aggregated particles, respectively. Reprinted with permission from ref.[64] Copyright © 2011, American Chemical Society.

2.9 Graphene and graphene based sensors

Graphene, a single layer of hexagonally arranged sp^2 carbon atoms was discovered in 2004 by Andre Geim and Konstantin Novoselov.[147-149] They received Noble Prize in physics in 2010 for the discovery of the novel 2D carbon materials. Since its discovery it has been attracted tremendous research interests both in fundamental research and applications due to its unique electronic,

quantum confinement, optical, and mechanical properties. [150-152] One of the most remarkable properties of graphene is the unique band structure at Dirac point that charge carriers behave as massless relativistic particles, and under ambient conditions they can move with little scattering. This phenomenon enables an electronic device with ultrahigh carrier mobility and at room-temperature mobility of ~10 000 cm^{-2} s^{-1} are measured.[147] To further increase the speed of electronic device, traditional silicon electronic device has limited room because the size of the device is approaching the quantum tunneling range. The graphene device, however, due to its ultrahigh carrier mobility opens up a new avenue for future high performance electronic devices. Another interesting property of graphene is its fluorescence quenching property due to resonance energy transfer. Compared to other quenching materials such as noble metals, graphene shows a larger quenching distance up to 30 nm.[152] In addition, the fluorescence quenching efficiency of graphene is one order of magnitude higher than that of gold.[153]

Different methods have been invented for production of graphene. Commonly used method include mechanical cleavage from graphite,[148] chemical vapor deposition (CVD)[154] and chemically oxidation and reduction from graphite.[155] The mechanical cleavage method simply use scotch tape to peel a layer of graphene sheet off the graphite. Different layers of graphene sheets could be produced using this method. It produces the pristine graphene with the best quality, however, this method yields graphene sheet with small sizes, which limit its applications in device fabrication. This method is most often used to produce high quality graphene for fundamental research.

Chemical vapor deposition (CVD) has been used to grow single and multiple layers of graphene of large size on metal surfaces, e.g. Ni and Cu.[154] Large area of epitaxial graphene films up to a few micrometers in size can be obtained and subsequently transferred to other substrates. The CVD method, however, requires the expensive CVD system and it is also not easy for large-scale fabrication. [156]

The oxidation and exfoliation of graphite oxide (GO) from graphite, followed by the chemical reduction has been developed to prepare reduced graphene oxide (rGO) sheets or chemically functionalized graphene (CFG).[157] This method produces rGO through a solution process which is easily scaled up. In addition, compared to pure graphene, the rGO also contains some functional groups such as hydroxyl, carboxylic group and epoxy group, which can be used for surface modification and functionalization.[158] Reduced graphene oxide (rGO), has become a promising material for biotechnology and biosensing application due to its superior characteristics such as large surface area, good water solubility, biocompatibility, easy surface modification, low manufacturing cost and good thermal stability etc.[156]

Many types of biosensors have been developed using graphene including electrical,[159] fluorescence[33] and electrochemical sensor[160] etc. Electrical sensor is based on a field effect transistor (FET) device where the graphene is used as active conducting layer. The graphene layer is functionalized with receptor molecules and the binding of target molecules changes the conductivity of the graphene layer, which is reflected as a change in current. This platform enables a label free, real time and sensitive assay. Electrical sensors have been widely used

for detection of DNAs,[161] proteins[162] , gas[18] and metals ions[163] etc. Chen et al. demonstrated an electrical assay using FET device for IgG, Figure 2.15.[164]

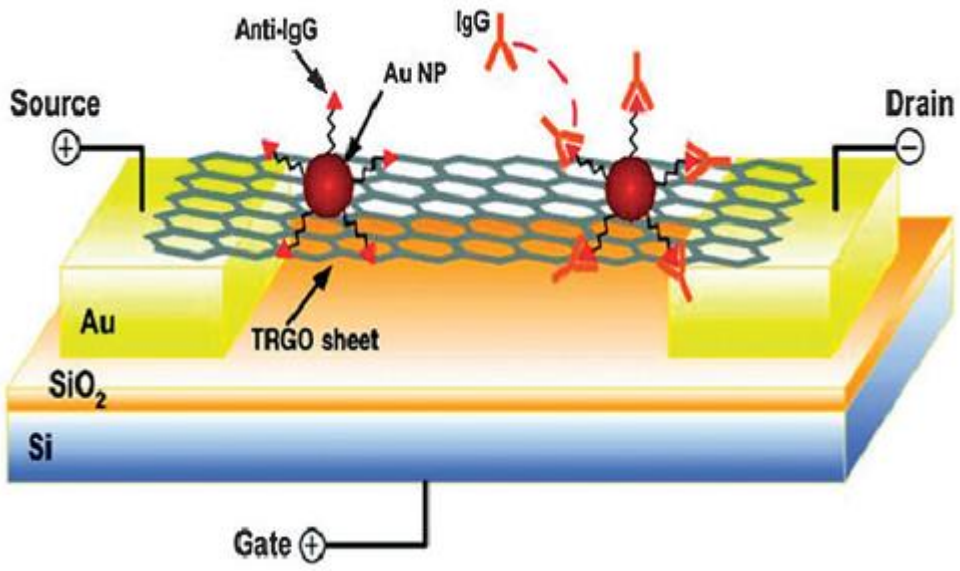

Figure 2.15 Illustration of a FET sensor based on a suspended thermally reduced graphene oxide (TRGO) for immunoglobulin G (IgG). Anti-IgG molecules are immobilized on the TRGO sheet through gold nanoparticles (AuNPs). Adapted with permission from ref.[164] Copyright © 2010 WILEY-VCH Verlag GmbH & Co. KGaA, Weinheim.

Due to its excellent fluorescence quenching ability, graphene is also widely used as substrate in a fluorescence resonance energy transfer (FRET) sensor. The principle of this sensor can be found in previous discussion in 2.6.

In addition, graphene has quickly become an attractive material for electrochemical sensors because of its unique electrochemical properties. Graphene has a large electrochemical potential window (~ 2.5 V in 0.1 mM phosphate buffer saline solution),[165] therefore, the detection of molecules that have high oxidation or reduction potential (e.g., nucleic acids) become possible.

Moreover, edges and defects on graphene could also enhance the electron transfer rate.[166] It has been demonstrated that the electron transfer rate of $Fe^{3+}/^{2+}$ on RGO electrode is one order of magnitude higher than that of glassy carbon electrode.[166] As a 2D material, graphene has extremely high surface-to-volume ratio (theoretically, 2600 m^2g^{-1}), which provide a large effective reaction area. Electrochemical sensors for many different target molecules have been developed with graphene as electrode. Xu et al. fabricated a H_2O_2 sensor using a RGO–chitosan composite as electrode, which is entrapped with hemoglobin (Hb) molecules.[167] This sensor shows a lower limit of detection (LOD) (0.51 μM) and a wider linear range (6.5–230 μM) compared to other electrodes. Kang et al. reported a sensor for glucose using GOD–RGO–chitosan as electrode, which exhibited a wider linear range (from 0.08 mM to 12 mM) and lower LOD (0.02 mM) compared to the sensors using other nanostructured materials.[168] Graphene based electrochemical sensors have also been used to detect various protein biomarkers. Su et al. reported a label-free immunosensor for cancer marker alpha fetoprotein (AFP).[169] Yang et al. reported a ultrasensitive electrochemical sensor for prostate-specific antigen (PSA) (marker for prostate cancer) using RGO modified electrode.[162] One of the main advantages of the electrochemical sensor compared to other types of sensor is that the device can be miniaturized and automated easily.

2.10 Biosensing Recognition Scheme

Specificity of biosensor is achieved by a receptor or recognition system. Most commonly used recognition system is the antibody-antigen. Antibody is a natural

protein, which contains one or many specific binding sites for antigen. It is an important natural defense mechanism in human body to help immobilize and remove the outside body (antigen) from the body. Generally, the affinity between antibody and antigen is very high. Antibody is widely used in biosensing and bioanalytics, e.g. the most commonly used ELISA assay.

However, one problem of antibody is that it is a natural protein, which suffers from the stability issue from environment. Normally, proteins are very sensitivity to pH, temperature etc. The extreme pH and temperature may induce a conformational change of the antibody and thus change its binding affinity. As a result, many synthetic receptors were invented, including DNA/PNAs,[63,72] aptamers,[15,71] and synthetic peptides[170,171] etc. These synthetic receptors have much better stability with environment.

Synthetic peptide is a short chain of amino acids linked by covalent amide bonds in a specific sequence manner which can be chemically synthesized by solid phase peptide synthesis. By designing, or modifying the peptide sequence, length and/or functional groups, synthetic peptide can specifically bind to a variety of biomolecules down to low nano-molar affinity. Recent advances in phage display technology, combinatorial peptide chemistry and biochemistry have led to the development of peptides as drugs and biological tools as potential better alternative to antibodies [172]. For biosensing applications, most critical problems of enzymatic and antibody-based biosensors are lack of stability/robustness and short shelf life [173]. In this regard, synthetic peptide has several important advantages compared to antibody as receptor. These include; stability and

robustness in high or low pH and high temperature, cheap and fast production, easy modification and optimization for affinity or for probe/functional moiety attachment, high purity (chromatographically pure >95 %) and low batch to batch variation [172].

Synthetic peptides with affinity to different molecules have been explored extensively. Liedberg et al. designed a helix-loop-helix peptide (JR2E) which could form a dimer itself at lower pH[174] and zinc ions.[47] The JR2E peptide could also form a heterodimer with its complementary peptide, JR2K.[70] The peptide JR2E is modified with a cysteine at the loop (JR2EC) to allow for immobilization on the AuNPs. The sequence of JR2EC and its complementary peptide JR2KC is shown in Figure 2.16. The JR2EC peptide has been used as scaffold for receptor molecules[47] as well as to control the aggregation of AuNPs.[12,75,175]

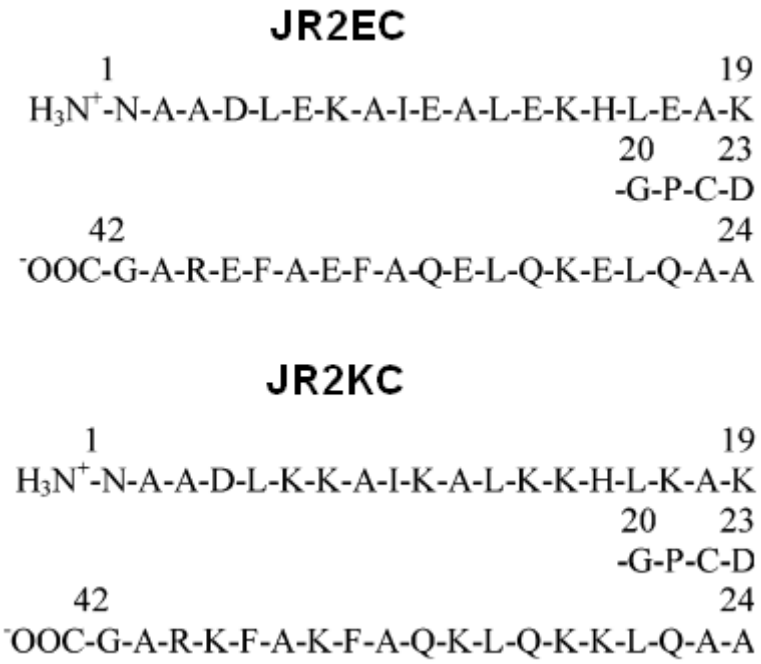

Figure 2.16 sequence of JR2EC and JR2KC. Adapted with permission from ref.[174] Copyright © 2005, American Chemical Society.

Peptide receptors for other chemical and biomarkers are also extensively explored. Takashi Takagi et al. reported a peptide binder (KC-13) for bacteria endotoxin or lipopolysaccharide (LPS). [176] Lipopolysaccharide (LPS) is a major component in the outer cell membrane of Gram-negative bacteria. It is a very powerful and toxic inflammatory stimulator which induces host monocytes and macrophages to secrete a wide range of inflammatory cytokines including interleukins-1, tumor necrosis factor-α, and interleukin-8 etc.[177-179] The binding affinity of the peptide KC-13 to LPS measured with SPR is ~0.1 to 10 nM. The sequence of the KC-13 is KKNYSSSISSIHC. Lee et al. reported a peptide binder for 2,4,6-Trinitrotoluene (TNT), a regulated explosive.[24] With this short peptide (WHW) as

receptor, an electrical sensor using carbon nanotube enable a sensitive detection of TNT with detection limit of 1 fM. Zhang et al. developed a peptide binder for troponin I (FYSHSFHENWPSK).[180] With this peptide as recognition element a sensitive electro-generated chemiluminescence sensor was fabricated for troponin I. The detection limit of this sensor is 0.12 ng/mL, which is lower than the level of troponin I in serum when cardiac events occur (5-50 ng/mL).

2.11 Synopsis of following chapters

In chapter 3 I have described a novel analysis method of LSPR peak using the shape of the peak instead of peak shift and extinction. The curvature of the LSPR peak is the maximum of the absolute value of the 2nd order derivative of the LSPR spectrum.

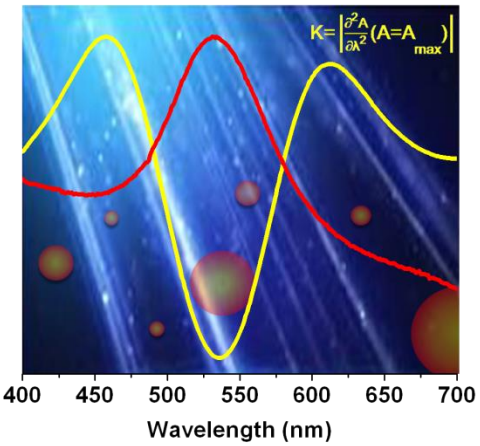

Figure 2.17 Illustration of the curvature of the LSPR peak of AuNPs.

The curvature takes into account the overall peak instead of value at single point. Compared to peak shift and extinction, this method shows better resolution to

refractive index. It is also less affected errors, such as shift of spectra in horizontal and vertical direction, tilt of spectra etc. induced by instruments and environments.

In chapter 4 I studied the effect of configuration of coupled AuNPs on the refractive index sensitivity. It is known previously that the coupling of AuNPs could enhance the refractive index sensitivity and the coupling is depends on the inter-particle distance. It is interesting that the coupling of AuNPs strongly depends on the position of neighbouring AuNPs.

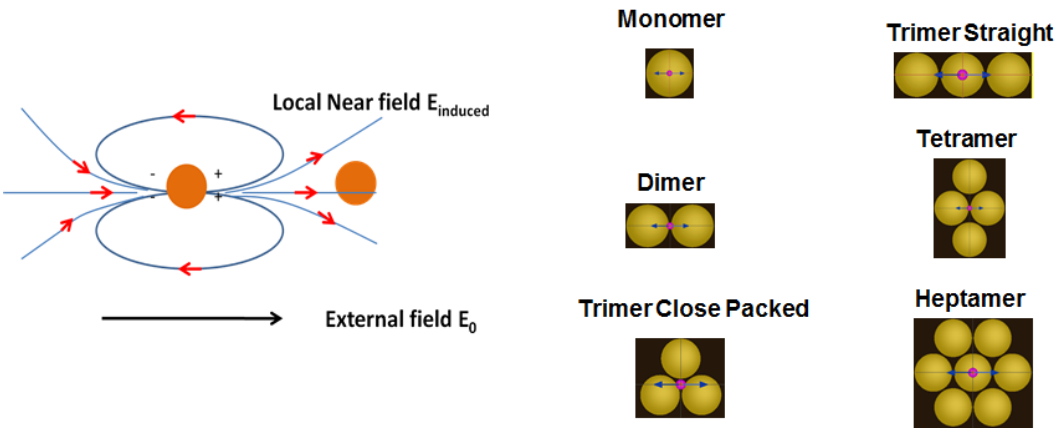

Figure 2.18 Effect of local electrical field on the AuNPs depends on the position of the neighboring AuNPs. Illustration of AuNP and AuNP clusters with different configurations.

From the study, it is concluded that AuNP clusters in linear configuration shows the best sensitivity.

In chapter 5, I developed a colorimetric sensor for metalloproteinase 7 (MMP-7) using the aggregation of peptide functionalized AuNPs. MMP-7 is an enzyme which is related to many cancers. A designed peptide substrate containing the

cleavage sites were immobilized onto AuNPs. The peptide bears 5 negative charges at neutral pH, which keep the AuNPs stable. With the presence of MMP-7, however, the peptide were digested into pieces and the segment left on AuNPs bears only 1 negative charge. The decrease in surface charge leads to the aggregation of AuNPs, which can be seen from the red to blue color changes by naked eyes.

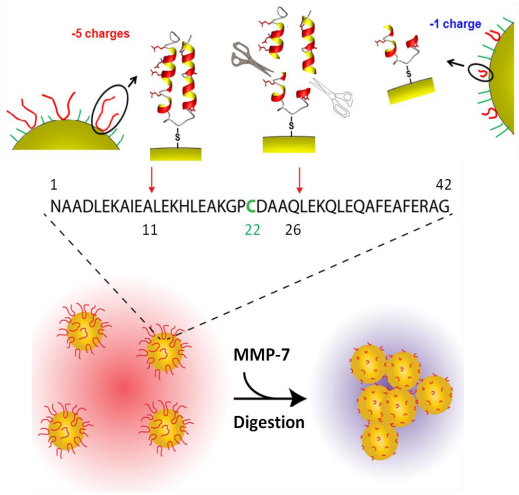

Figure 2.19 Illustration of the colorimetric sensor of MMP-7: digestion of peptide on AuNPs leads to an aggregation of AuNPs and color changes.

In Chapter 6, I presented a potential hybrid sensing platform utilizing two independent transducing mechanisms, namely LSPR and Raman scattering, respectively. For biological molecules, the Raman scattering is very week compared to fluorescence. To detect Raman scattering, a novel substrate based on graphene and $Au_{0.7}Ag_{0.3}$ NP composite was fabricated. With this substrate, Raman scattering is significantly enhanced by $Au_{0.7}Ag_{0.3}$ NP, while the fluorescence is quenched by graphene.

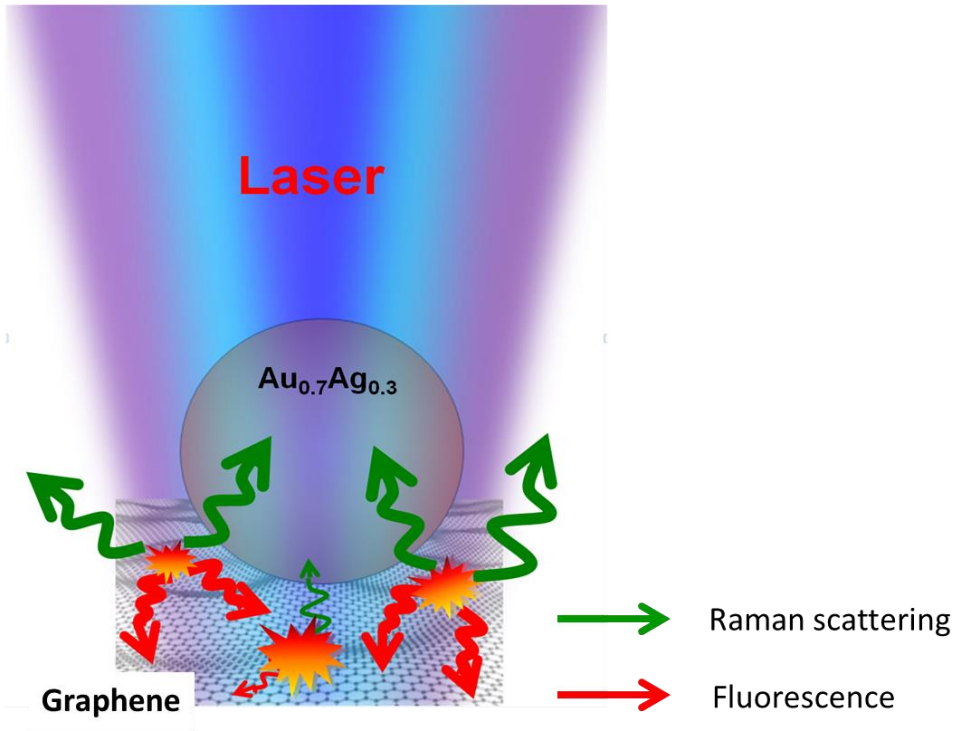

Figure 2.20 Illustration of the enhancement of Raman scattering from $Au_{0.7}Ag_{0.3}$ NPs and fluorescence quenching from graphene.

In Chapter 7, I described a few collaborative projects on biological sensing, including:

- 7.1 Bio-functionalized gold nanoparticles for colorimetric sensing of botulinum neurotoxin A light chain
- 7.2 Gold aggredots for colorimetric G6PD deficiency sensing
- 7.3 Peptide-assembled graphene oxide as fluorescent turn-on sensor for specific and sensitive lipopolysaccharide detection

- 7.4 Optimizing the refractive index sensitivity of plasmonically coupled gold nanoparticles
- 7.5 High-density metallic nanogaps fabricated on solid substrates used for surface enhanced Raman scattering
- 7.6 Label-free, electrochemical detection of methicillin-resistant staphylococcus aureus DNA with reduced graphene oxide modified electrodes
- 7.7 Real-time DNA detection using Pt nanoparticle-decorated reduced graphene oxide field-effect transistors

Chapter 3: Refractive index sensing using the curvature of the LSPR peak

The collective oscillation of free electrons in the conduction bands of gold and other noble metals is known as surface plasmon resonance (SPR). Since the first report of SPR sensing in 1983,[6] it has been widely explored and developed into a well-established commercial tool.[5,7,181] Recently, noble metal nanoparticles have attracted tremendous interest in both fundamental[64,182-187] and applied research including sensing,[45,188-190] surface enhanced Raman scattering (SERS),[48,95,191] and photovoltaic device[192,193] etc. Contrary to propagating surface plasmon waves, the electron plasma oscillation in nanoparticles is localized to the particle, a phenomenon referred to localized surface plasmon resonance (LSPR).[44] The LSPR resonance frequency/wavelength of the nano-sized noble metals depends on their size, shape, composition, inter-particle distance and the medium they are embedded/dissolved in.[183] Biomolecular sensing by LSPR sensors mostly relies on the peak shift or extinction changes induced by refractive index changes or inter-particle aggregation phenomena occurring in response to molecular recognition and/or attachment/bridging phenomena.[72,76,87,194] The refractive index sensitivity of LSPR sensors depends on the polarizability of the nano-sized plasmonic structure/particles, which commonly varies from a few tens to a few hundred nm/RIU.[93] Despite the many advantages over propagating (planar) SPR sensors in terms of spatial resolution and cost, the refractive index sensitivity of LSPR sensors is still about 4 orders of magnitude smaller than of planar SPR.[9] In addition, the ability to resolve minute changes in the LSPR peak

position/extinction is limited by instrumental/chemical noise, e.g. from the light source and/or detector. As a result, detecting targets at ultralow concentrations using LSPR is very demanding especially for low molecular weight molecules. Many efforts have been undertaken to increase the sensitivity of LSPR sensors by synthesizing novel nano-materials with higher polarizability, such as nanorods,[195] nanodisks,[196] nanoshells[58] and nanotriangles[197] etc. Physicists also have explored the potential of meta-materials by fabricating novel sub-micron plasmonic patterns using lithography techniques.[85,86] Although these efforts improve the refractive index sensitivity of LSPR sensors to some extent, they also bring many problems such as high cost, low yield and tedious processing.

In this contribution, we report a new strategy to monitor changes in the shape of LSPR peak of gold nanoparticles (AuNPs). Contrary to peak shifts or extinction changes that monitors the changes of the peak maximum at a certain point, the curvature of the LSPR peak takes into account the overall peak shape. Our theoretical and experimental findings demonstrate that the curvature (2^{nd} order derivative at peak maximum) is approximately linearly related to refractive index in regimes relevant to sensing.

3.1 Sensing principle: the relationship between curvature and refractive index

The real and imaginary parts of the size-corrected dielectric function of 13 nm AuNPs from Johnson and Christy are plotted in Figure 3.1(a). For AuNPs in the 10-30 nm range, localized surface plasmon resonance occurs at ~ 520 nm.[183] In a

small range (±40 nm) around the LSPR peak, the real and imaginary parts of the dielectric function can to be approximated with simple functions. As illustrated in Figure 3.1(b), the real part of dielectric function is well approximated with a linear function while the imaginary part can be fitted with a reciprocal function, see Eq.(3.1) and Eq.(3.2), respectively.

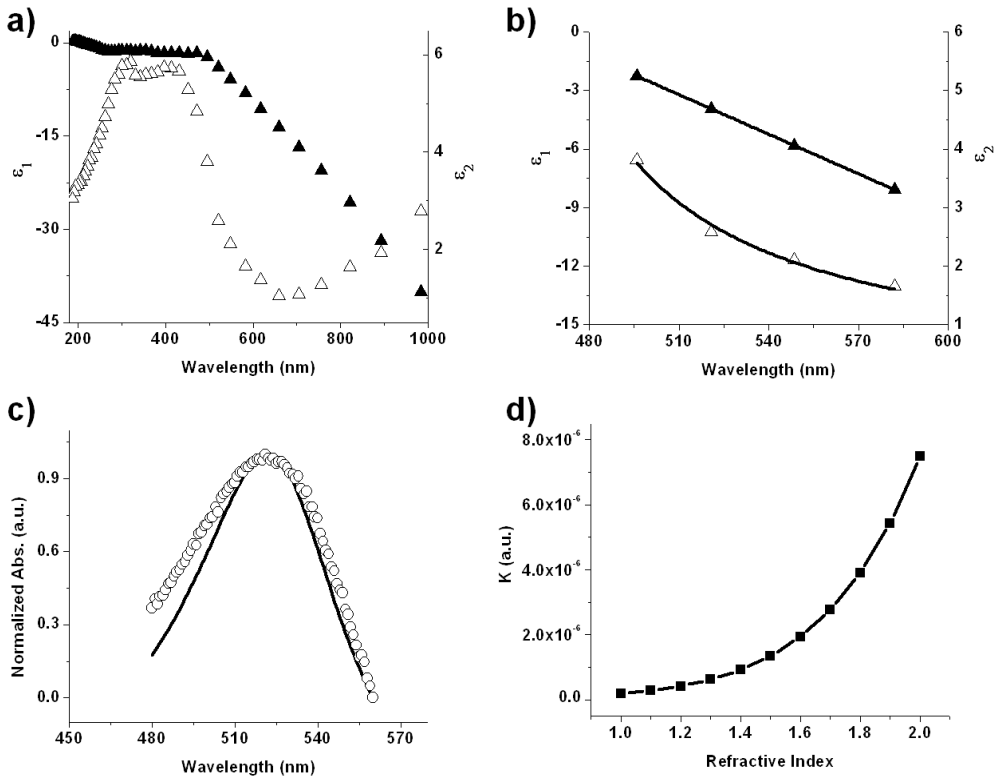

Figure 3.1 (a) Real (filled triangle) and imaginary (open triangle) Johnson and Christy dielectric function of 13 nm gold nanoparticles (AuNPs) corrected for the size dependent surface damping. (b) Real (filled triangle) and imaginary (open triangle) dielectric function of 13 nm AuNPs in (a) near the LSPR peak. The real part is fitted with a linear function, Eq.(3.5) while the imaginary part is fitted with a reciprocal function, Eq.(3.6). Experimentally determined fitting constants are: a_1 =31.27, b_1= -0.0676, R^2=0.9999, a_2 =-1.799, b_2=0.00416, R^2=0.9864. (c) Measured absorption spectrum of 13 nm AuNPs in solution (open circles) and calculated absorption spectrum (solid line) by Mie theory using size corrected dielectric function fitted with the functions in (b), Eq.(3.10). Both spectra show a LSPR peak at ~ 521.0 nm. (d) Calculated changes in curvature K for AuNPs exposed to different media with refractive indices varying from 1 to 2, Eq.(3.15).

It should be stressed that the strategy used here to approximate dielectric functions is not necessarily the only way. Polynomial approximations of dielectric functions also have been employed elsewhere.[198] The particular set of approximations used herein was chosen for the sake of easy derivation of the 2nd order derivatives.

$$\varepsilon_1(\lambda) = a_1 + b_1\lambda \qquad (3.1)$$

$$\varepsilon_2(\lambda) = \frac{1}{a_2 + b_2\lambda} \qquad (3.2)$$

Fitted constants (see legend of Figure 3.1) are used in the calculation of the absorption spectrum and curvature. From the Beer–Lambert law, the absorption of any material is related to the absorption cross section σ_{abs} by

$$A = Nl\sigma_{abs}\,, \qquad (3.3)$$

where N is number density of absorbers and l is path length. Furthermore, the angular frequency is related to the wavelength through the speed of light in the medium (c/n), Eq.(3.4), and the permittivity of the solvent is related to the refractive index, Eq.(3.5).

$$\omega = \frac{2\pi c}{\lambda n} \qquad (3.4)$$

$$\varepsilon_m = n^2 \qquad (3.5)$$

From above equations, the wavelength and refractive index dependent absorbance of a 13 nm AuNPs can be derived

$$A(\lambda, n) = \frac{18\pi V n^2 N l}{\lambda} \frac{(a_2 + b_2\lambda)}{(a_2 + b_2\lambda)^2 (b_1\lambda + a_1 + 2n^2)^2 + 1}. \qquad (3.6)$$

The calculated (solid line) and the experimentally measured (open circles) absorbance spectrum in water are shown in Figure 3.1(c). The calculated spectrum matches quite well with the experimentally determined one. Both spectra show a LSPR peak at ~ 521 nm. The measured spectrum, however, suffers from a heterogeneous broadening or Gaussian broadening, which is always observed for real samples with size/shape variation.[54]

The curvature is related to the sharpness of the peak and mathematically it can be defined as the absolute value of the second order partial derivative of absorbance with wavelength at the peak position.

$$K = \left| \frac{\partial^2 A}{\partial \lambda^2} (A = A_{max}) \right| \qquad (3.7)$$

From Mie theory, the LSPR peak of AuNPs occur at

$$\varepsilon_1(\lambda) + 2\varepsilon_m = 0 \qquad (3.8)$$

The curvature as a function of wavelength can be writes as,

$$K(\lambda) = 36\pi V N l \left[\frac{b_1^2 n^2 (a_2 + b_2\lambda)^3}{\lambda} + \frac{b_2 n^2}{\lambda^2} - \frac{n^2 (a_2 + b_2\lambda)}{\lambda^3} \right]. \qquad (3.9)$$

From Eq (3.5), (3.6), and (3.8), λ can be expressed as

$$\lambda = -\frac{2n^2 + a_1}{b_1}. \qquad (3.10)$$

By inserting Eq.(3.14) in Eq.(3.9) *K(n)* can be written as

$$K(n) = 36\pi VNl\left\{-\frac{b_1^3 n^2\left[a_2 - \frac{b_2}{b_1}(2n^2+a_1)\right]^3}{2n^2+a_1} + \frac{{b_1}^2 b_2 n^2}{(2n^2+a_1)^2} + \frac{{b_1}^3 n^2\left[a_2 + \frac{b_2}{b_1}(2n^2+a_1)\right]}{(2n^2+a_1)^3}\right\}. \quad (3.11)$$

The calculated curvature K as a function of refractive index n in the range from 1 to 2 is plotted in Figure 3.1(d).

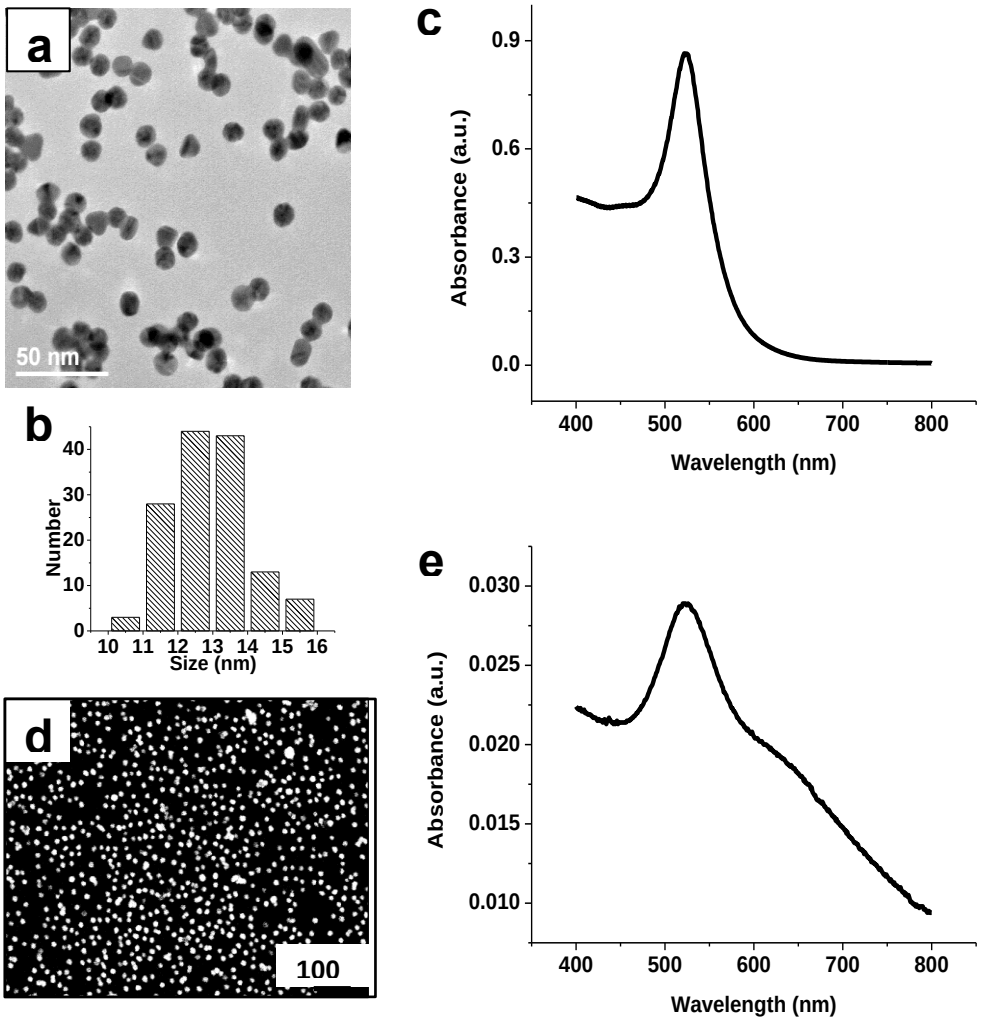

Figure 3.2 (a) Transmission electron microscope (TEM) image of as prepared AuNPs. (b) Histogram of the size distribution of AuNPs shown in (a). (c) Absorption spectrum of AuNPs in solution. (d) Scanning electron microscope (SEM) image of AuNPs assembled on glass substrate. (e) Absorption spectrum of AuNP SAMs on glass in air.

Gold nanoparticles with a size of ~13 nm were synthesized by reduction of chloroauric acid ($HAuCl_4$) with sodium citrate.[89] The size of the AuNPs can be tuned by the ratio of sodium citrate to chloroauric acid. Figure 3.2(a) shows a Transmission Electron Microscope (TEM) image of the as synthesized AuNPs and their size distribution is summarized in the histogram plot in Figure 3.2(b). Most of the AuNPs have a size between 11 and 14 nm, with an average size of 12.9 nm and standard deviation of 1.1 nm, respectively. The absorption spectrum of the AuNPs in solution is shown in Figure 3.2(c). A prominent peak is observed at 521 nm, which is due to the localized surface plasmon resonance. The peak is sharp, indicating narrow distribution of size and shape of the AuNPs, which also agrees with the observations of TEM images, Figure 3.2 (a) and (b). The AuNPs are negatively charged due to the capping agent, sodium citrate, and the Zeta-potential of the AuNPs equals -37 mV. Nanoparticle assemblies were obtained by attaching the AuNPs to glass substrate.[45,199] Briefly, the glass substrate was first functionalized with (3-Aminopropyl)triethoxysilane (APTES) which bears positive charges from the primary amine group. Citrate capped AuNPs adsorbs via electrostatic attraction to the positively charged APTES surface. Figure 3.2(d) shows the secondary electron image of a typical AuNP assembly on APTES-modified glass. The AuNPs are evenly distributed on the glass substrate, with a few exceptions where aggregation is observed. The absorption spectrum of the AuNP assemblies measured in air is shown in Figure 3.2(e). The absorption spectrum of the AuNP assemblies resembles that of AuNPs in solution Figure 3.2(c), except for a slight broadening and the appearance of a shoulder between

600 and 700 nm. This shoulder is attributed to the small fraction of aggregated AuNPs in the sample. Its presence has a marginal effect in the analysis of peak shift, absorption and curvature of the peak at 521 nm, because the two LSPR peaks are well separated from each other.

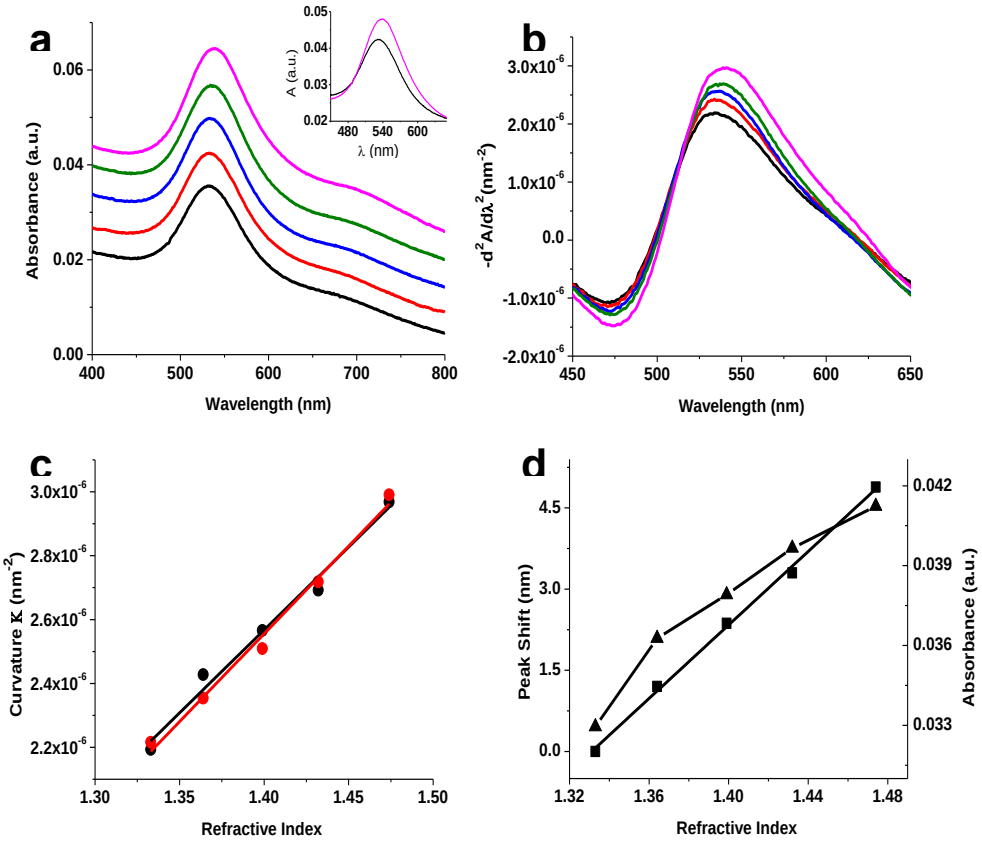

Figure 3.3 (a) Absorption spectra of AuNP SAMs on glass substrate immersed in solvents with different refractive indices: 1.333 (black), 1.364 (red), 1.399 (blue), 1.432 (green) and 1.474 (purple), respectively. Spectra are offset in purpose for better visualization. Inset: zoom in absorption spectra of AuNPs in solvent with refractive index 1.333 (black) and 1.474 (purple). (b) Second order derivatives of absorption spectra in (a). (c) Experimental (black circles/line) and calculated (red circles/line) curvature of AuNPs immersed in media with different refractive index. Experimental (black) and calculated (red) data are fitted linear function to yield a slope of 5.19×10^{-6} $nm^{-2}RIU^{-1}$ (R^2=0.9804) and 5.49×10^{-6} $nm^{-2}RIU^{-1}$ (R^2=0.9876), respectively. (d) Experimentally measured peak shift (squares) and absorbance (triangles) at different refractive indices. The peak shift is fitted linearly, with a slope of 34 nm/RIU (R^2=0.9970).

The effect of refractive index on the LSPR response was investigated experimentally by measuring the absorption spectra of AuNPs in solvents with different refractive indices varying from 1.333 to 1.474 (prepared by varying the concentration of glycerol in water), Figure 3.3(a). As the refractive index increases, the LSPR peak shifts towards the red, the absorbance values and the sharpness of the LSPR peak increase (sharpness = A_{max}/FWHM), Figure 3.3(a) inset. Second order differentiation with wavelength was performed on the curves in Figure 3.3(a) and the corresponding curves are plotted in Figure 3.3(b).

Generally, the 2nd order derivatives are related to the sharpness of the curve. Local maxima are observed in the spectra of the 2nd order derivatives at the LSPR peak wavelength, the absolute value of which is defined as the curvature, see Eq.(11) and Figure 3.3(b). The curvature of AuNPs on APTES-modified glass in solvents of different refractive indices (black circle) is plotted in Figure 3.3(c).

The experimental measured curvature (black circles) matches well with the calculated values (red circles). In the small range between 1.333 and 1.474, both the experimental measured and calculated curvature can be approximated by a linear function Figure 3.3(c). The slope of measured curvature with refractive index is 5.19×10^{-6} $nm^{-2}RIU^{-1}$, which is very similar to the calculated one 5.49×10^{-6} $nm^{-2}RIU^{-1}$.

The corresponding peak shift (squares) and absorption (triangles) are plotted in Figure 3.3(d). The peak shift increases linearly with refractive index, with a

sensitivity of 34 nm/RIU, which is in line with observations reported elsewhere.[93] The absorption, on the other hand increases rapidly for small refractive index changes but appears to start leveling off when the refractive index increases further, above n=1.36.

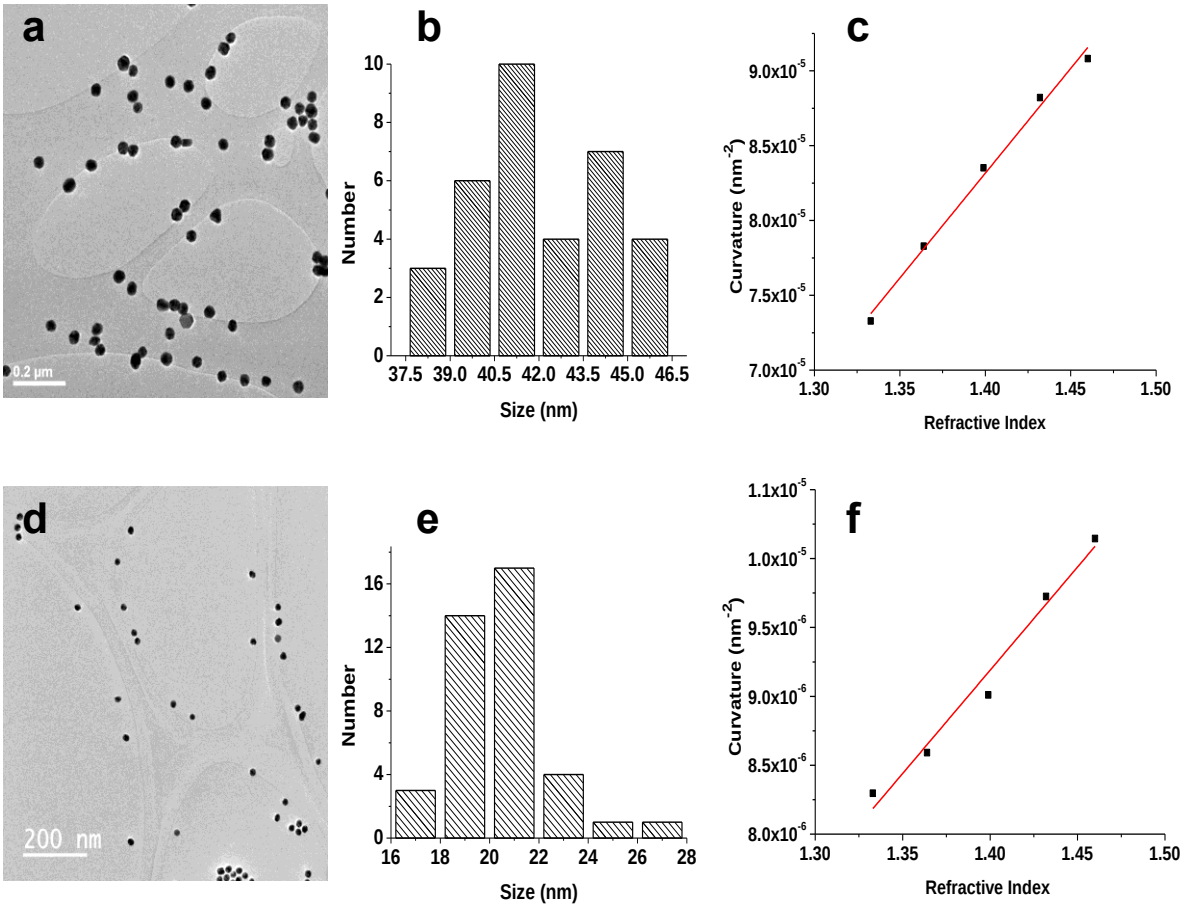

Figure 3.4 (a) TEM image of 40 nm sized AuNPs . (b) Size distribution of the 40 nm AuNPs in (a). (c) the curvature of 40 nm AuNP assemblies measured at different refractive index (black dots) and linear fitting (red line). The slope of the fitted line is 1.4×10^{-4} nm^{-2}RIU^{-1} and R^2 equals 0.9910. (d) TEM image of 20 nm sized AuNPs . (e) Size distribution of the 20 nm AuNPs in (d). (f) the curvature of 20 nm AuNP assemblies measured at different refractive index (black dots) and linear fitting (red line). The slope of the fitted line is 1.5×10^{-5} nm^{-2}RIU^{-1} and R^2 equals 0.9726.

The linear relationship between curvature and refractive index is not limited to 13 nm AuNPs. To illustrate the universal relationship, AuNPs with a size of 40 nm and 20 nm were also used to study the response of curvature with refractive index. The TEM image of 40 nm AuNPs is shown in Figure 3.4(a) and the distribution of size is plotted in Figure 3.4(b). The average size of the AuNP is 41.8 nm and standard deviation is 1.9 nm.

The curvature of the 40 nm AuNP assemblies exposed to solvents with different refractive index is plotted and linearly fitted in Figure 3.4(c). It is very clear that in the range between 1.333 and 1.474, the curvature is approximately a linear function of refractive index, with a slope of 1.4×10^{-4} $nm^{-2}RIU^{-1}$. Figure 3.4(d) and 3.4(e) shows the TEM image and size distribution of 20 nm AuNPs. The average size of the AuNP is 20.6 nm and standard deviation is 1.8 nm. The curvature of the 20 nm AuNP assemblies in different solvents is plotted and fitted linearly in Figure 3.4(f). Similar to 13 nm and 40 nm AuNP the curvature of 20 nm AuNP is also a linear function of refractive index. The fitted slope of the curvature with respect to the refractive index is 1.5×10^{-5} $nm^{-2}RIU^{-1}$.

3.2 Comparison of curvature to traditional peak shift and extinction techniques

In addition to sensitivity, the noise level is an equally important factor in sensing. To compare the performance of peak shift, absorption and curvature in LSPR sensing, the signal-to-noise ratio (S/N) is calculated, which is defined as response per refractive index unit (sensitivity) divided by the noise level. The sensitivities and noise levels shown in Table 3.1 are derived from the experimentally

measured data. The sensitivity obtained S from four distinct AuNP assemblies on glass with different surface densities (see Figure 3.5) are used to determine the sensitivity. The noise levels are calculated as the standard deviation from 20 measurements on the AuNP samples. Compared to the sensitivity, the noise level is much more sensitive to the method used to evaluate the LSPR peak, e.g. maximum of measured value or fitted maximum. Accordingly, two different common methods are used to evaluate the noise of each variable.

The absorption spectra of the four samples in different solvents from 1.333 to 1.474 are shown in Figure 3.5(a)-(d), respectively. From the absorbance values, it is very obvious that AuNPs on sample 4 are more densely packed than on the others, Figure 3.5(d). The surface density of AuNPs of sample 1 is the lowest of the four, while sample 2 and sample 3 are quite similar. FESEM images on the four samples are shown in Figure 3.5(e)-(h), respectively. The surface density of the four samples calculated from FESEM images are 156/μm^2, 197/μm^2, 180/μm^2 and 463/μm^2, respectively. Table 3.1 summarizes the sensitivity of four different samples in Figure 3.5, noise and the S/N ratio, respectively.

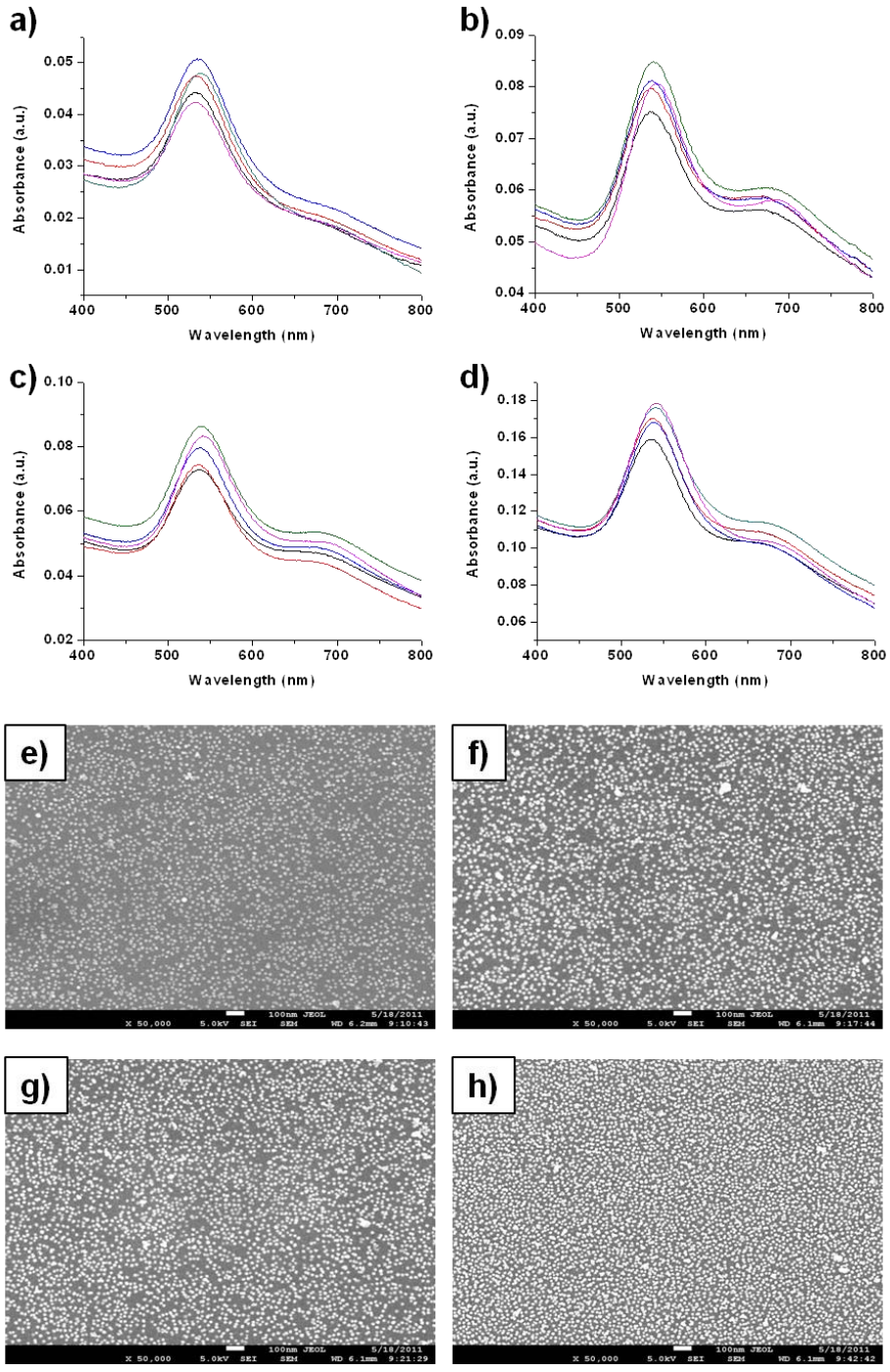

Figure 3.5 (a)-(d) absorption spectrum of AuNP sample 1, 2, 3 and 4 in different solvents with refractive indices from 1.333 to 1.474, respectively. (e)-(h) FESEM image of AuNP sample 1,2,3 and 4, respectively.

Table 3.1 Refractive index sensitivity *S*, noise and signal-to-noise ratio (*S/N*) for the peak shift (λ), absorbance (*A*) and curvature (*K*), respectively. Two methods are used to calculate the noise for each variable. For the peak shift: the centroid (centre of gravity of peak) [56] and shift of peak maximum. For the absorption: the response for the fitted A_{max} and the response at of A at 546 nm. For the curvature K: the response for the fitted K_{max} and the response of K at 546 nm.

Sample Sensitivity S	λ_{max} ***(nm/RIU)***		A_{max} ***(RIU^{-1})***		K_{max} ***(nm^{-2}RIU^{-1})***	
1	34.4		0.0436		5.19×10^{-6}	
2	31.6		0.0733		6.84×10^{-6}	
3	27.7		0.0490		5.67×10^{-6}	
4	43.8		0.1260		1.63×10^{-5}	
Noise N	$\lambda_{centroid}$ ***(nm)***	λ_{max} ***(nm)***	A_{max}	***A(546)***	K_{max} ***(nm^{-2})***	***K(546) (nm^{-2})***
	0.2	0.68	1.23×10^{-4}	1.72×10^{-4}	9.46×10^{-9}	1.29×10^{-8}
Sample S/N ratio	$\lambda_{centroid}$ ***(RIU^{-1})***	λ_{max} ***(RIU^{-1})***	A_{max} ***(RIU^{-1})***	***A(546) (RIU^{-1})***	K_{max} ***(RIU^{-1})***	***K(546) (RIU^{-1})***
1	172.2	50.6	353.7	253.4	548.5	401.6
2	158.1	46.5	594.9	426.2	723.2	529.6
3	138.7	40.8	397.3	284.7	598.8	438.5
4	219.0	64.4	1022.6	732.6	1722.5	1261.3

The S/N ratio (calculated from the optimized noise) of peak shift, absorbance value and curvature of four distinct samples, (Figure 3.5) are plotted in Figure 3.6, respectively. For all the four samples, the S/N of peak shift is the lowest among the three, which is due to the high noise of peak position. The big variation in peak position originates not only from the instrumental noise, but also from the

sample itself. The S/N of absorption is significantly improved as compared to the peak shift. This phenomenon has been observed and used for sensing by other investigators.[56] The S/N ratio of curvature is however, better than both the peak shift and absorption. It is worthwhile noticing though that the S/N varies from sample to sample. Sample 4 shows consistently improved S/N ratio in peak shift, absorption and curvature than other three samples. We propose that the higher S/N ratio in sample 4 is due to an inter-particle coupling effect originating from the higher surface density of AuNPs, Figure 3.5. This enhancement of refractive index sensitivity has been reported theoretically and experimentally elsewhere.[200] For the sake of sensing, the higher S/N ratio of curvature translates into a lower LOD, *caeteris paribus*.

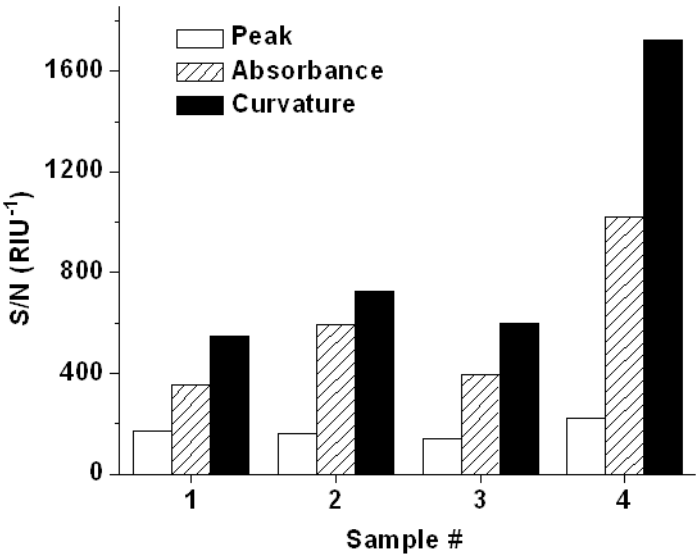

Figure 3.6 The S/N ratio of peak shift, absorbance and curvature of four different AuNP assemblies calculated from optimized noise levels, respectively.

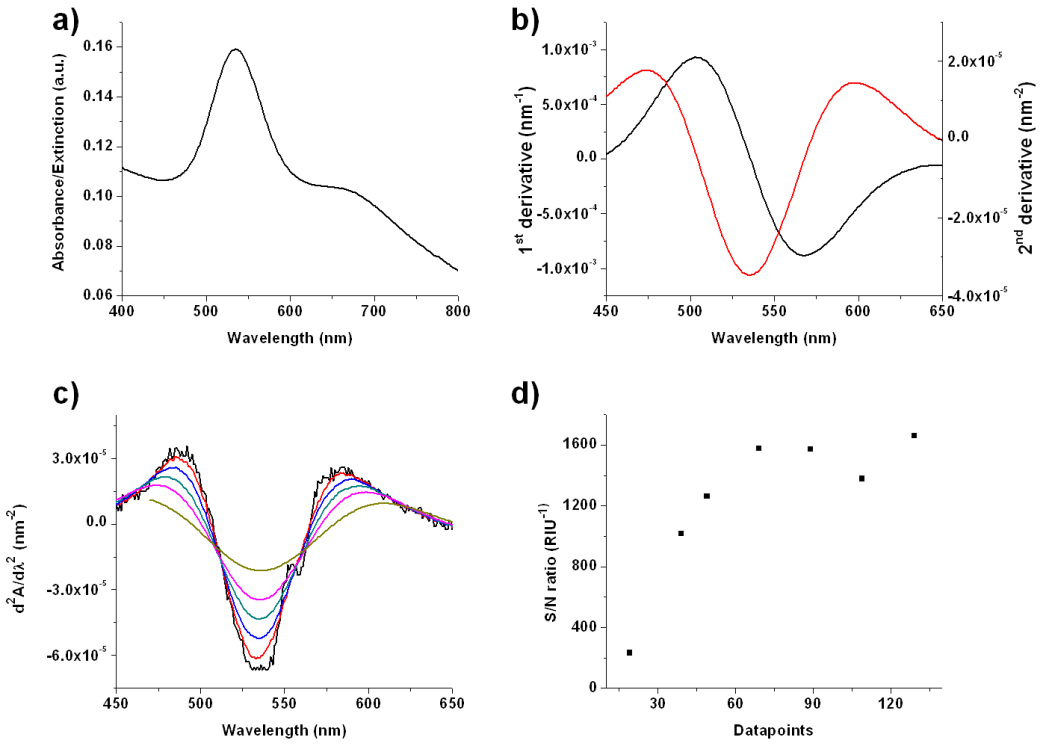

Figure 3.7 (a) Extinction spectrum of AuNP assemblies on glass measured in water. (b) The first (black) and second order (red) derivatives of the spectrum in (a). (c) The second order derivative of spectrum in (a) with 9 (black), 19 (red), 29 (blue), 39 (cyan), 49 (pink) and 69 (brown) data points used in the calculation of derivatives. (d) S/N ratio with bulk refractive index of curvature calculated using different number of data points.

An absorption spectrum of a typical AuNP assembly on glass is shown in Figure 3.7(a). The first and second order derivatives of the spectrum with wavelength are shown in Figure 3.7(b). Second order derivatives are calculated from two sequential first order derivatives. The derivative spectrum depends strongly on the number of data points utilized for the calculations. Figure 3.7(c) shows the second order derivative the absorption spectrum in (a) calculated using different numbers of data points from 9 to 69. As the number of data points increases, the spectrum of second order derivatives becomes smooth, which helps to reduce the noise. In

addition, the amplitude of the second order derivatives also becomes smaller with the increasing data points used. The S/N ratio of curvature with bulk refractive index is plotted in Figure 3.7(d). The S/N ratio increases quickly with the increasing number of data points used below 69 points, after which the S/N ratio is not very sensitive to the number of data points used.

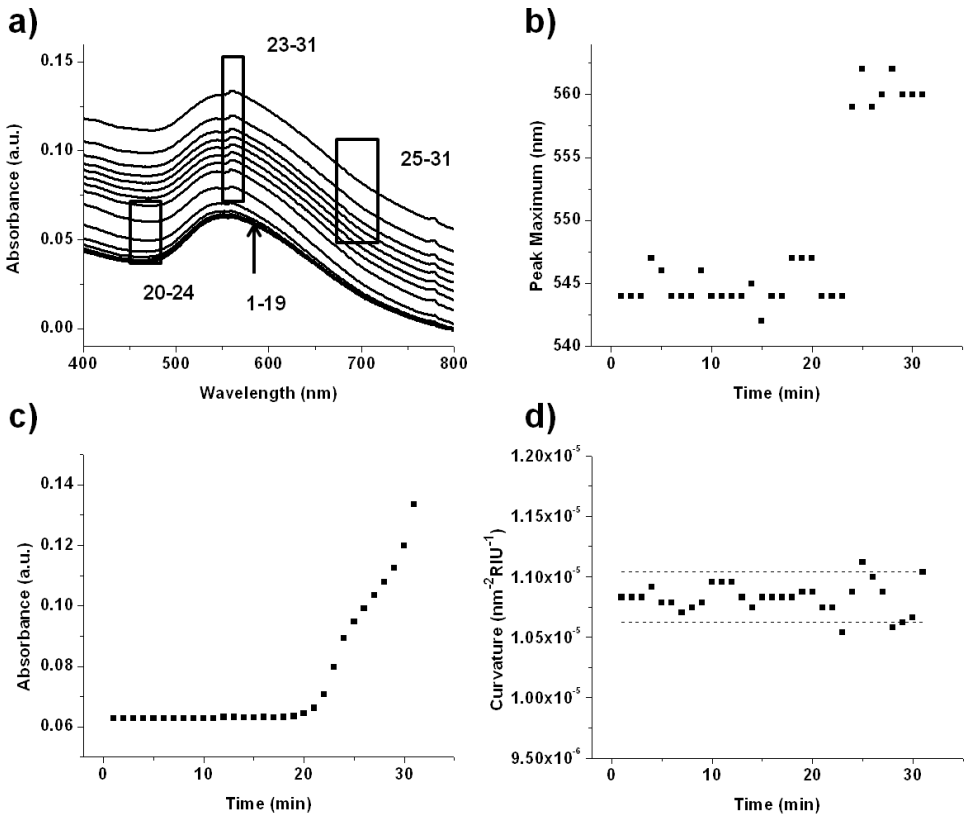

Figure 3.8 (a) 31 absorption spectra of AuNP on glass immersed in water measured over time. The time interval of measurement is 1 min. Arrow: stable baselines are observed from time 1 to 19 min. Errors occurs at time 20 min for some particular reasons. Left rectangle: spectra start to tilt from spectrum 20. Right rectangle: spectra shift upwards. Middle rectangle: a step-like feature appears near the peak maximum. (b) Evolution of peak shift (the maximum) over time. (c) Evolution of absorption over time. (d) Evolution of curvature over time. Dashed lines: 3 time the standard deviation (3σ) of baseline from 1 to 19 min.

In addition to noise (normal variation), other errors/artifacts (abnormal variations) may also be present in the absorption spectra. In a typical absorption measurement, errors in absorption and peak position are inevitably present and occur from time to time most frequently due to instrumental instabilities. Other errors are of chemical nature and might arise from non-specific adsorption of contaminants. These errors may shift the absorption spectrum in wavelength (horizontal direction) or absorption (vertical direction), tilt the overall spectra or produce sharp spikes/steps etc. The instrumental and/or chemical errors could make a measurement based on single point recording inaccurate. Fortunately, such errors do not affect the curvature as long as the overall peak shape remain unchanged. A series of absorption spectra displaying typical errors are depicted in Figure 3.8(a).

The absorption spectra overlap during the first 19 min of measurement. For some unknown reasons the spectra start to tilt and shift vertically after 20 min. Three kinds of errors associated with the measurements are recognized. Tilt of spectra occurs first (20-24), where the absorption values at lower wavelengths increase more than those at longer wavelengths. After the initial tilting, the spectra uniformly shift upwards at all wavelengths (25-31). In addition, some sharp step-like features are also observed near the peak maximum (23-31). The evolution of peak shift, absorption and curvature of the spectra in Figure 3.8 (a) are plotted in Figure 3.8(b), (c) and (d), respectively. From Figure 3.8(b) and (c), it is obvious that these errors move the response signal away from stable baseline. Interestingly, these errors have very limited effects on curvature, Figure 3.8(d). The curvature is

very stable and no significant trend of deviation from baseline can be observed. The significance of variation is illustrated using 3 times of the standard deviation (3σ) of baseline (dotted lines). When the spectra are stable (1-19 min), the value of curvature oscillate inside the channel formed by 3σ. When the errors start to become visible in the spectra, 3 cases of breaking of the channel formed by 3σ are observed at 23, 25 and 28 min, respectively. Interestingly, the curvature values go back immediately after breaking the 3σ lines, and thus it can not be considered as a signal of new trend. Instead, the effect of these errors on curvature can be better described as the increase in the magnitude of oscillation. This interesting phenomenon can be explained by Eq.(3.11). Mathematically, the overall shift of peak position σ_λ or absorption σ_A ca be describes as a zero order change and the tilt as a first order change ($k\lambda+\sigma_A$). They are both eliminated completely in a second order derivatives, Eq.(3.11).

3.3 Response to small molecule binding and biosensor development

To illustrate the advantages of curvature in monitoring of molecular binding, a small thiol molecule (SH-PEG$_7$-COOH, M_w=458.6) which readily adsorbs to AuNPs through the -SH moiety was used. In a typical experiment, the AuNP assemblies on glass were incubated in 10 μM SH-PEG$_7$-COOH and the adsorption process was monitored over time.

The evolution of the LSPR peak shape and absorption is shown in Figure 3.9(a), and it is obvious that the absorption increases and the LSPR peak also become

narrower with time. Figure 3.9(b) summarizes the response of the peak shift, and a red shift of the LSPR peak (about 1nm) can be clearly seen after a few minutes. In the first 8 min of adsorption, the peak shift is not distinguishable due to the high noise level. Figure 3.9(c) shows the response of absorbance due to the adsorption of the thiol molecule on the AuNP surface. The binding of the thiol molecule induce a significant increase in the absorbance over the time.

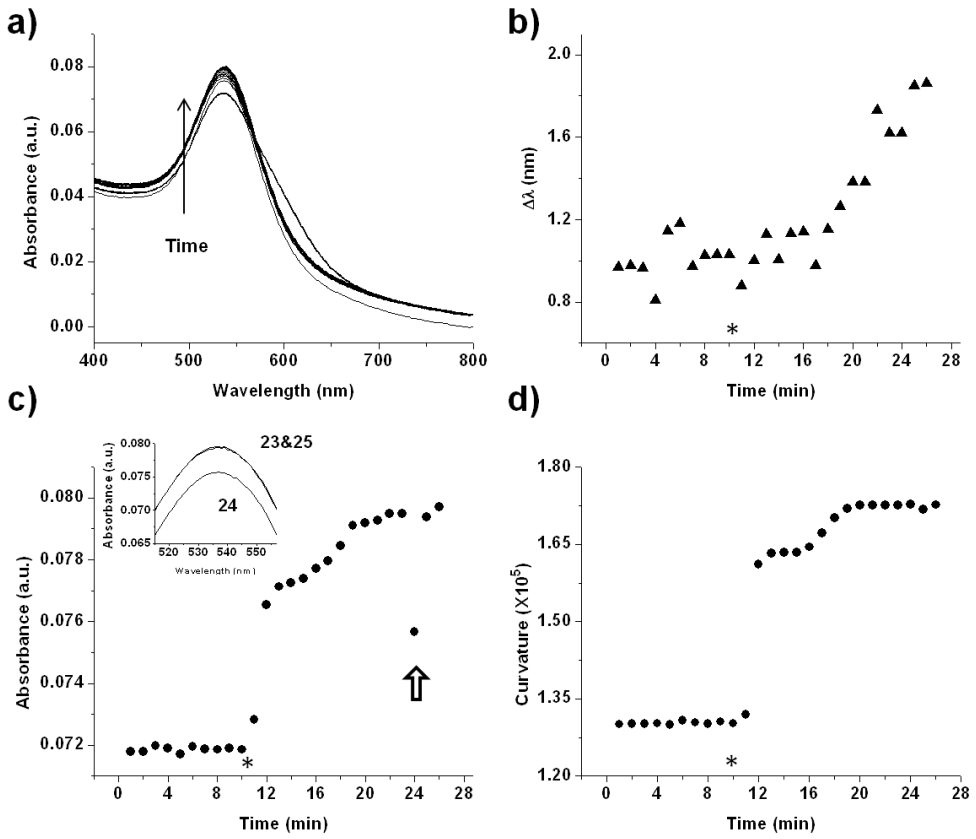

Figure 3.9 (a) Evolution of absorption spectra of AuNP assemblies on glass upon incubation of 10 μM SH-PEG_7-COOH. The SH-PEG_7-COOH was introduced after 10 min stabilization. (b) Peak shift of the absorption spectra in (a) at different time of incubation. (c) Absorbance of the absorption spectra in (a) at different time of incubation. An overall shift down of spectrum occurs at time 24 min, see inset (23, 24 and 25 min). (d) Curvature of the absorption spectra in (a) at different time of incubation.

At time 24 min, there is a spike due to the overall shift down of the absorption spectrum, see inset. Figure 3.9(d) shows the response of curvature. The S/N ratio of this particular monolayer forming molecule obtained for peak shift, absorption and curvature equals 7.4, 87.6 and 179.2, respectively. The binding of the thiol molecules appears to saturate after 20 min adsorption. Further addition of 10 μM SH-PEG_7-COOH molecule did not introduce any further changes. This suggests that with curvature it is able to accurately monitor the adsorption process of this small thiol molecule. The ability to monitor small molecules using nanoparticles is advantageous compared to traditional planar SPR sensors due to the localization of the field from the plasmon. The improvement of S/N ratio of curvature over absorption and peak shift comes from two factors. Firstly, the noise level of curvature is lower than that of peak shift and absorption, because it eliminates some 0^{th} and 1^{st} order variations in peak shift and absorption, Eq. (3.11). Secondly, the sensitivity to refractive index is higher than absorbance because it captures both changes in absorbance and width of peak. As shown in Figure 3.9(a), with molecular binding of the thiol molecule, both the increase in height and decrease in width contribute the response of curvature. In addition, the sharp feature in absorbance due to instrumentation imperfections at time at 24 min (see arrow in Figure 3.9(c)) didn't show up in the curvature, which is consistent with the observation in Figure 3.8.

To demonstrate the capability of curvature as an analytical tool in biosensor, a prototype LSPR sensor for GSH was developed. Human cells can contain up to 10 mM of reduced glutathione (GSH) which serves as an antioxidant in protecting

cells from oxidative stress [201]. Detection of reduced glutathione is important for the diagnosis of glucose-6-phosphate dehydrogenase deficiency, a disease affecting over 400 million people worldwide[202]. Disease carriers are extremely sensitive to oxidative substances such as quinine derivatives that are used to treat malaria, of which with exposure to, can lead to lethal hemolytic anaemia. Detecting glutathione is challenging due to the small size (M_w=307.32 g/mol), which only consists of three amino acids. Herein, LSPR sensor based on 13 nm AuNPs together with curvature were utilized to monitor the binding of GSH.

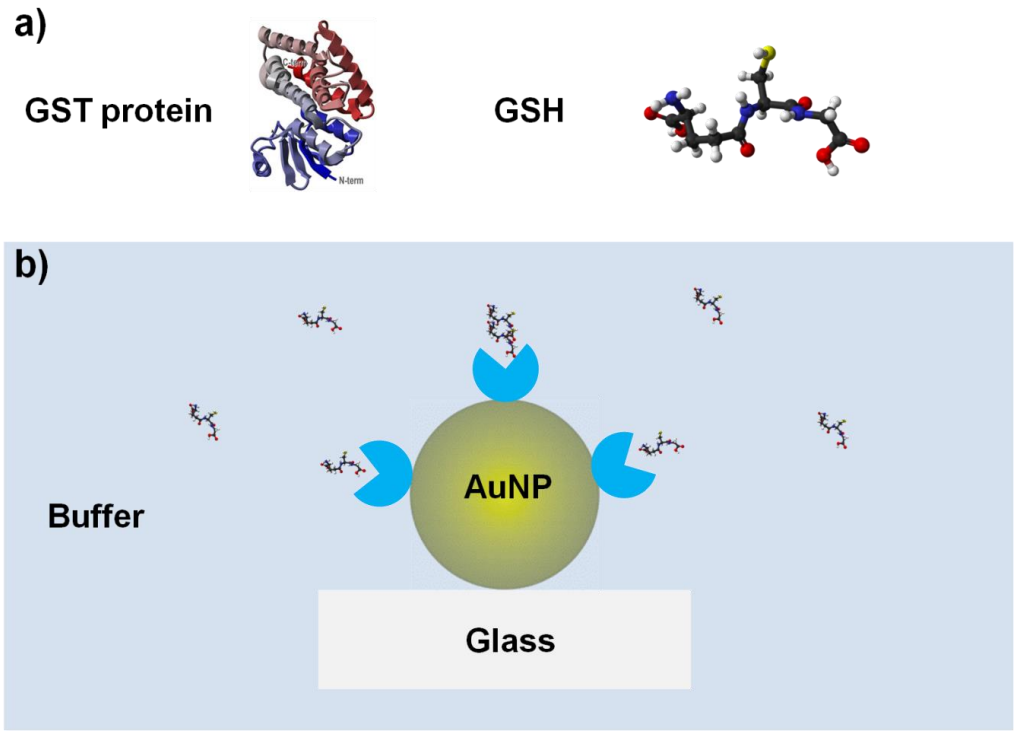

Figure 3.10 (a) GST protein (monomer) and GSH molecule. (b) Illustration of the LSPR sensor for GSH.

To achieve specificity in our assay, we utilize the dimeric glutathione-S-transferase (GST) protein (Figure 3.10(a) of *schistosoma japonicum* which is

extremely specific to reduced glutathione[203] as a receptor. The structure of the GST protein monomer and GSH is shown in Figure 3.10 (a) and the LSPR sensor for GSH is illustrated in Figure 3.10 (b).

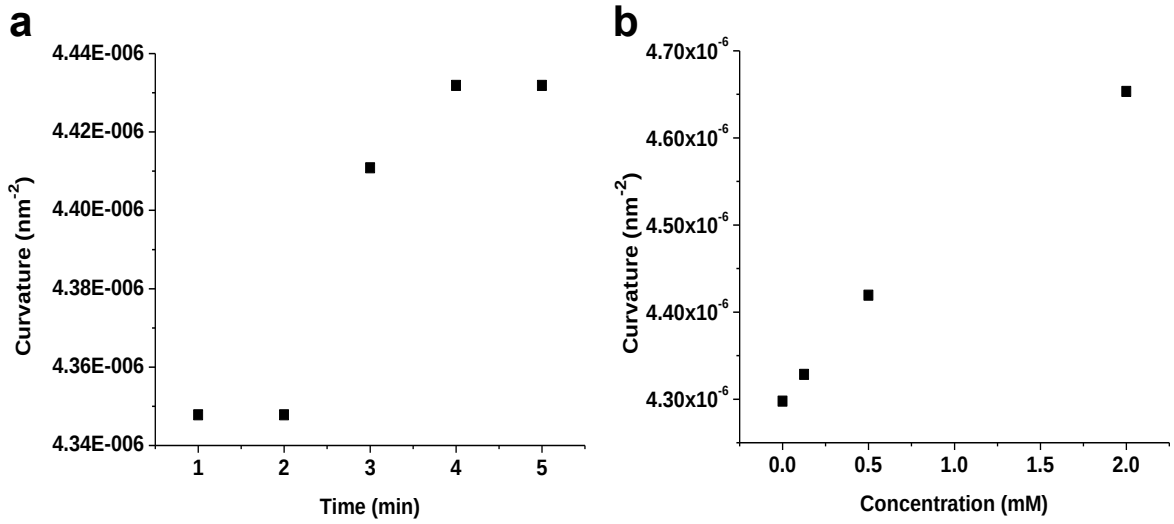

Figure 3.11 (a) curvature of 13 nm AuNP assembly on glass with addition of 0.5 mM GSH at time 2 min. (b) Curvature of 13 nm AuNP assembly with different concentrations of GSH.

The binding of GSH to GST protein induced an increase in curvature and the kinetics of binding is very quick. Figure 3.11(a) shows a real time binding curve of 0.5 mM GSH. The binding reach equilibrium very quickly in ~3 min. Figure 3.11(b) shows the curvature of AuNPs with different concentrations of GSH. From the curve we can see that the LSPR sensor is very sensitive to the concentrations from 0.1 mM to 2 mM. The concentration of GSH in red blood cell is round 10 mM. Therefore, LSPR sensor with curvature is sensitive enough to monitor the levels and binding kinetics of GSH in clinical relevant concentrations.

3.4 Experimental Section

Sodium citrate tribasic dehydrate (99%), gold (III) chloride trihydrate (99.9%), (3-Aminopropyl)triethoxysilane (APTES) (97%) and glycerol (99%) were purchased from Sigma Aldrich. Microscope slides from Sail Brand were used as glass substrates. Thiol PEG7 acid (O-(2-Carboxyethyl)-O'-(2-mercaptoethyl)-heptaethylene glycol) was purchased from Polypure AS, Norway. Gold nanoparticles with the size of 20 nm and 40 nm were purchased from BBI solutions. Reduced glutathione GSH was purchased from Sigma Aldrich.

Gold nanoparticles were synthesized by reduction of $HAuCl_4$ using Trisodium citrate.[89] In a typical synthesis, 90 mL Milli-Q water and 10 mL 10 mM $HAuCl_4$ were mixed and heated to above 100 ℃ under reflux for 2 hrs. Aqueous solution of 10 mL 77.6 mM. Trisodium citrate was added quickly to the reflux solution by piston and needle. The color of the solution changes from pale yellow to red in c.a. 10 s. Heating was maintained for another 15 min before cooling down to room temperature in air. The gold nanoparticles were stored in 4 ℃ fridge for future use. A Joel 2100 transmission electron microscope (TEM) was used to characterize the size of the nanoparticles and their distribution. Absorption spectra of AuNPs in solution were measured with a Perkin Elmer absorption spectrometer Lambda 35. Zeta-potential of the citrate capped AuNPs was measured using the spectrometer from Malvern Instrument. The size of AuNPs was derived from TEM images using the software image J and the distribution and standard deviation were calculated from over 200 randomly chosen individual particles.

Pieces of glass substrate with 2×0.5 cm^2 were cut from microscope slides and incubated in a mixture of water, 30% H_2O_2 and 25% ammonia solution (5:1:1 in volume) at 80 ^oC for 10 min for remove contaminants. Then they were rinsed copiously with Milli-Q water for a few times. After the cleaning, the glass substrates were dried by nitrogen gas. The cleaned glass substrates were incubated with 1% (volume) of APTES in 99.9% ethanol for 30 min for surface functionalization. After functionalization, the substrates were rinsed with Milli-Q water and dried in nitrogen gas. A drop of as synthesized AuNPs (200 μL) was casted onto the APTES modified glass surface and incubated for 30 min to 4 hr to generate different amount of surface density. After incubation, the glass substrates with AuNPs were rinsed with Milli-Q water and dried with nitrogen gas. Secondary electron images on the AuNP coated glass were conducted on Joel 7600F field emission scanning electron microscope (FESEM), and a thin layer of platinum coating was applied to avoid charging effect. Absorption spectra were measured by immersing the substrate into a PMMA cuvette containing 1 mL solution using Perkin Elma absorption spectrometer. White light source was used and the resolution of light used in the measurement is 1 nm. Solvents with different refractive indices were prepared by mixtures of water and glycerol. Volume fractions of glycerol in the five solvents are 0%, 25%, 50%, 75% and 100%, respectively. Thiol PEG_7 solution was diluted in cuvette from stock a solution of 1mM.

GST protein was over expressed in E.Coli BL21 (DE3) Plyss bacteria transformed with pET-41B plasmid encoding a GST protein with 2 tandem histidine tags

(approx 36 kDa protein products). As the GST-gene is driven by a lac-operon, initiation of protein expression was carried out with the use of 1mM IPTG at a bacterial culture optical density of 0.8. Induction was carried out for 4 hours at 37℃ before bacterial cells were harvested by centrifugation (7000 x g), and stored at -80℃ for further downstream purification. GST protein was purified through the 6x histidine tag on the c-terminus of the protein. Bacterial Pellets with the expressed protein of interest, was re-suspended in ice cold lysis buffer (50mM Phosphate, 300mM NaCl, 20mM Imidazole, 1mM Betamercaptoethanol) and sonicated for 10 minutes on ice to break the bacterial cells to release the protein of interest into solution. Unlysed cells and cellular debris was removed via centrifugation (10,000 x G, 20 minutes) and the supernatant 0.2um filtered (Sartorius) before loading onto Nickel affinity chromatography resin for affinity purification. Dimeric GST protein was immobilized onto the AuNPs directly by incubating the AuNPs in 100 μM dimeric GST protein solution for 30 min followed by careful rinse with DI water. The GSH target molecules were introduced into the PMMA cuvette and measured every minute. Analytical derivation of derivatives and numerical calculations of absorption cross section were performed using the software Mathematica 9.

3.5 Conclusions

A new strategy to monitor LPSR responses utilizing the shape of LSPR peak (curvature) is reported. The relationship between the curvature of the LSPR peak and the refractive index of the surrounding medium is investigated theoretically and experimentally. In a narrow regime relevant to biomolecular sensing, the

curvature of the LSPR peak can be approximated with a linear function of the refractive index. From a typical adsorption experiment of a small thiol molecule it is demonstrated that monitoring of the curvature offers improved S/N ratio and reliability over monitoring of absorbance and peak shift. The proposed strategy to follow adsorption phenomena in real time offers a convenient way to push the limit of detection and improve the reliability of LSPR sensing. We furthermore demonstrate that with curvature the LSPR sensor could monitor sub-monolayer adsorption of small molecules, which could be useful in biological sensing and drug screening. A prototype LSPR sensor utilizing curvature for reduced glutathione (GSH) was developed. The curvature is not sensitive to the tilt, shift and sharp spikes in the absorption spectra, which could be helpful in monitoring interaction in complicated matrix, e.g. serum, juice etc. We also anticipate that the use of curvature can improve the read out of other transducers technologies based on monitoring the movement of a resonance or absorption feature over time.

Chapter 4: Effect of Configurations on the Refractive index Sensitivity of Coupled Gold Nanoparticles

4.1 Configurations of coupled AuNPs on 2D plane

The LSPR resonance frequency of gold nanostructures is dependent on the refractive index of medium.[44] In a typical sensor, the binding of target molecules could change the refractive index and thus lead to detectable LSPR peak shift. The sensitivity of the sensor is measured by the amount of peak shift per unit change of refractive index (nm/RIU). For spherical gold nanoparticles, the sensitivity is relatively small[45,46], which limits its applications to detect target molecules at low concentrations. To improve the sensitivity, nanostructures with higher polarizability have been synthesized, such as gold nanorod, gold nanoshell etc.[58,93] In addition, plasmonic coupling between two adjacent plasmonic particles also could enhance the sensitivity.[82] The coupling strength between adjacent gold nanoparticles depends on the inter-particle distance has been shown theoretically and experimentally.[114,200] Herein, we demonstrate that the coupling strength and thus refractive index sensitivity is also influenced significantly by the configuration of the gold nanoparticles. Figure 4.1(a) shows the effect of an external field (black arrow) and the local induced field (the blue line and red arrow) near a gold nanoparticle. It is clear that the external field is uniform in intensity and direction, whereas the induced local field has different intensity and direction at different places. As a result, for the right nanoparticle, the total electric field it feels depends not only on the distance from the left particle but also the position where it is located. Figure 4.1(b) shows a heptamer with equal

inter-particle distances, with an external excitation in the direction of blue arrow. The total electric field equals the external electric field plus the local near field of all the neighbors. Because of the different position of the surrounding particles, their contribution to the total electric field of the centre particle is different. The position dependent local near field intensity and direction determines that different configurations of AuNP clusters have different optical properties.

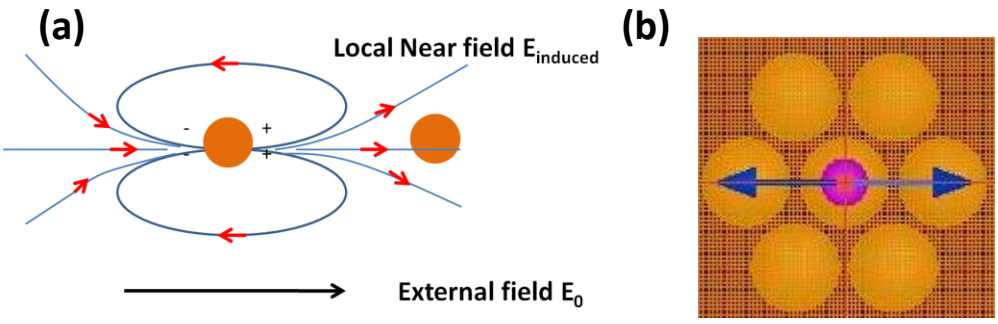

Figure 4.1 (a) Illustration of the effect of near field from surrounding AuNP. (b) Simplification of a high density AuNP SAMs into a heptamer configuration.

When exposed to external electric field, AuNPs are polarized into electric dipoles, which can be described by Eq. (4.1). The effective electric field on one AuNP can be calculated by summation of external field with the electric field from the induced electric dipoles from all the surrounding AuNPs, Eq. (4.2)

$$\mu = \alpha \varepsilon_m E_0 \qquad (4.1)$$

where, μ is dipole moment, α is polarizability, ε_m is the permittivity of surrounding medium, E_0 is external electric field.

$$E = E_0 + \sum_{i=1}^{n} \frac{\mu_i}{2\pi\varepsilon_m\varepsilon_0 d_i^3} \qquad (4.2)$$

Where, E is the effective electric field on AuNP, ε_0 is the permittivity of vacuum, d is centre to centre distance, n is the number of surrounding particles.

FDTD (Finite difference time domain) simulation is used to simulate the sensitivity AuNP clusters with different configurations shown in Figure 4.2.

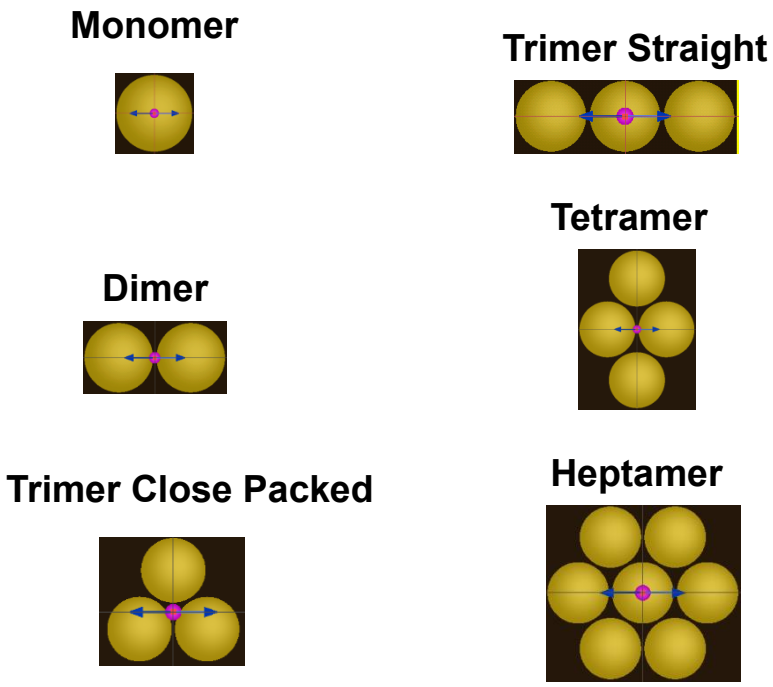

Figure 4.2 Different configurations of AuNP clusters used in simulation at different surrounding media. The size of AuNP is 40 nm and inter-particle distance is 2 nm.

In a typical simulation, AuNP clusters with 1 AuNP (monomer), 2 AuNPs (Dimer), 3 AuNPs (trimer straight, trimer close), 4 AuNPs (tetramer) and 7 AuNPs (heptamer) were calculated in 4 different refractive index media with indices 1, 1.2, 1.4 and 1.6, respectively. For all the different configurations, the

separation of AuNPs is kept at 2 nm. Among the clusters, the AuNP monomer is simulated using Mie theory due to its spherical geometry.

Figure 4.3 shows the electric field distribution at resonance condition around a monomer (a) and a heptamer (b) with a diameter of 40 nm and gap of 2 nm. From the field distribution, we could see that in heptamer the strongly coupling from the surrounding particles increase the electric field intensity significantly compared to the single particle in (a).

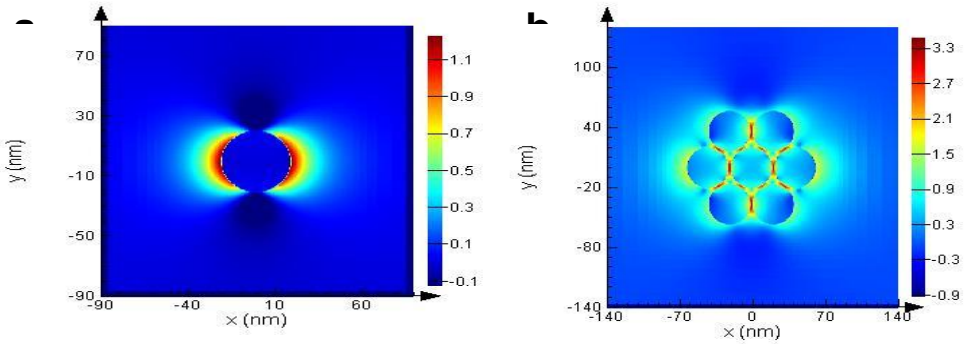

Figure 4.3 Electro-magnetic field strength around a single AuNP (a) and a heptamer (b). The color bar is in $\log_{10}$ scale.

Simulated extinction spectra of various AuNP clusters exposed to medium with different refractive indices are shown in Figure 4.4. Peak shift at different refractive indices at plotted and linearly fitted in Figure 4.5(a). The refractive index sensitivity of different AuNP clusters is summarized in Figure 4.5(b).

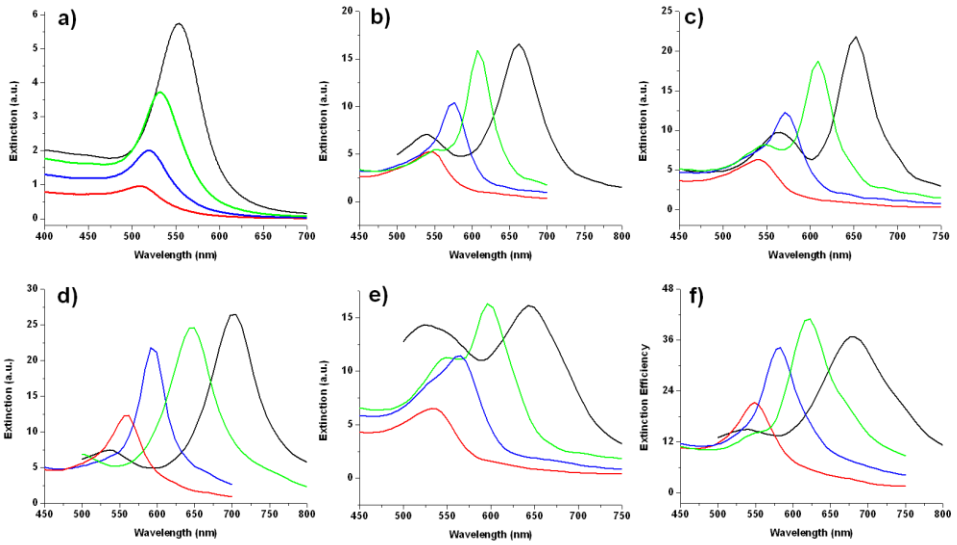

Figure 4.4 Simulated extinction spectra of different AuNP clusters illustrated in Figure 4.2 at different refractive indices: red 1.0, blue 1.2, green 1.4 and black 1.6. (a) monomer, (b) dimer, (c) trimer close, (d) trimer straight, (e) tetramer and (f) heptamer.

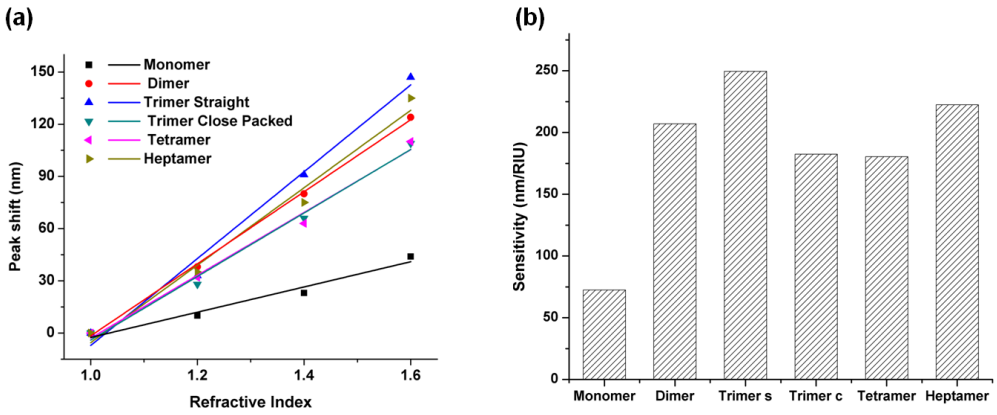

Figure 4.5 Peak shift at different refractive indices of various AuNP clusters are shown in (a) and the sensitivity is summarized in (b).

Figure 4.5 shows that trimer with straight configuration offers the highest sensitivity, followed by the close packed and parallel configurations. A general

rule for configuration is that adding a particle in the direction that is parallel to external field will improve the sensitivity, whereas adding a particle in the direction that is perpendicular to the external field will reduce the sensitivity.

From the simulation, it is clear that the trimer in straight form and heptamer show very good sensitivity. However, it is very difficult to fabricate samples with these configurations experimentally. Traditional optical lithography technique has the difficulty in resolution. E-beam lithography has the difficulty to generate samples in large area for sensing applications. From an application point of view, a closely packed AuNP SAMs is a good approximation of the heptamer and it is also easy to fabricate by self-assembly technique. The approximation of whole close pack SAM as heptamer is reasonable considering the fact that the electric filed decay very fast with distance from the AuNP surface and the interaction between AuNPs are negligible beyond the nearest neighbors. Two AuNP SAMs with low and high density of AuNPs are fabricated in the FESEM image of them are shown in Figure 4.6(a) and (b), respectively.

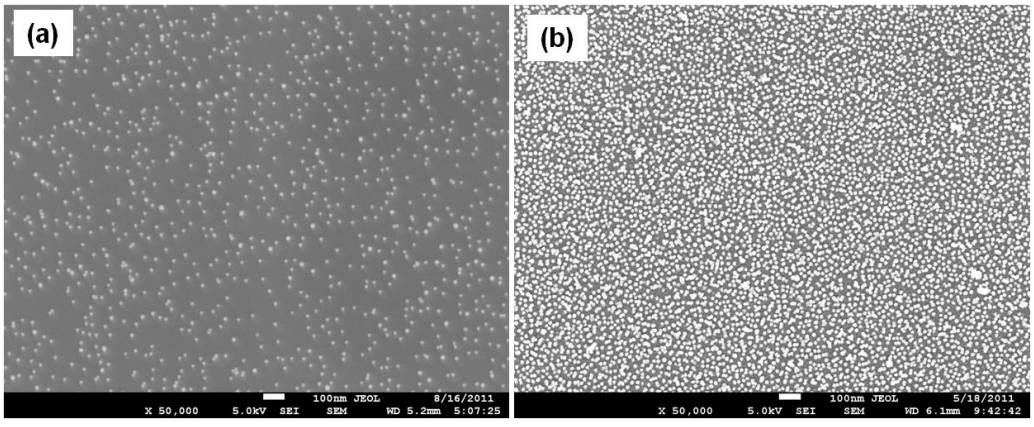

Figure 4.6 (a) 13 nm AuNPs assembled on APTES modified glass with low density (b) 13 nm AuNPs assembled on APTES modified glass with high density.

The absorption spectra of the low and high density AuNP SAMs exposed to solvents with different refractive indices from 1.333 to 1.474 are shown in Figure 4.7(a) and (b), respectively.

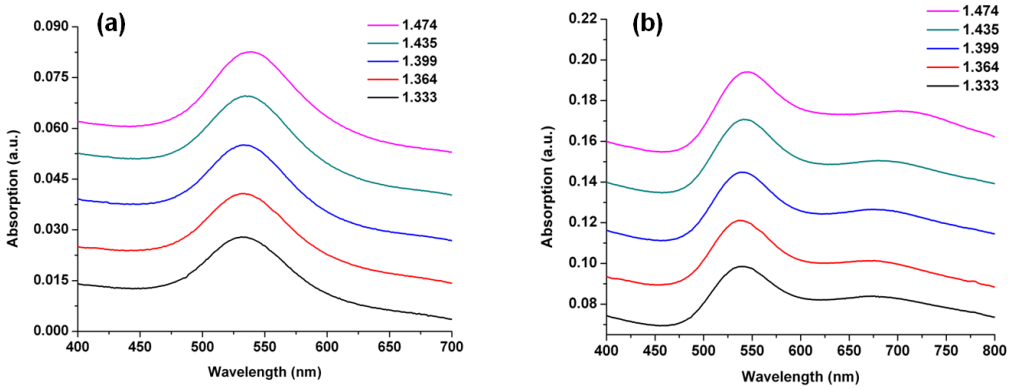

Figure 4.7 (a) Absorption spectra of low density AuNP SAMs in solvents with different refractive indices. (b) Absorption spectra of high density AuNP SAMs in solvents with different refractive indices.

Upon gradually increasing the refractive index from 1.333 to 1.474, the LSPR peak of the low density SAMs in Figure 4.7 (a) shows a slight red shift from 520 nm. On the other hand, with the same increase of refractive index, the LSPR peak in high density SAMs in Figure 4.7 (b) shows a much larger shift, which is attributed to inter-particle coupling. The peak shift for the low density samples at different refractive index is plotted and fitted linearly in Figure 4.8. The sensitivity of the high density samples is 269.7 nm/RIU, which represents a 7 times improvement from that of the low density sample, 38.4 nm/RIU. It is worthwhile mentioning that the coupling peak in the high density sample is very broad due to the large variation in inter-particle distance in the sample. Generally,

the broadening is not desirable in sensing as it reduces the figure of merit (FOM). Coupled nanostructures with uniform gaps can be fabricated using e-beam lithography. With this technology, a sharp coupling peak is expected and it could result in a higher FOM.

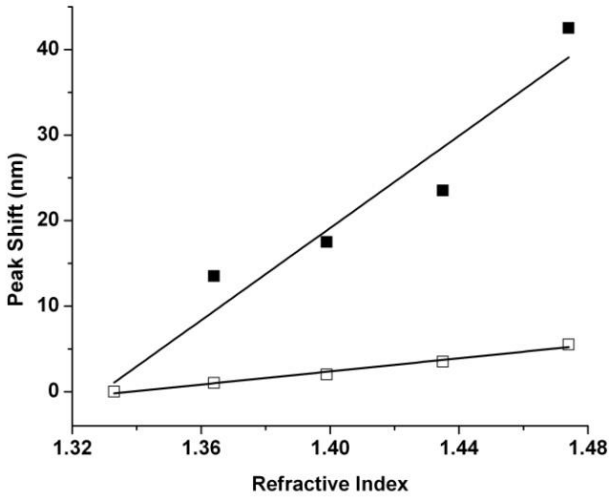

Figure 4.8 Peak shift of individual peak in low density SAMs (open square) and linear fitting with slope of 38.4 nm/RIU and R2 of 0.9801. The coupling peak (solid square) in high density SAMs and linear fitting with slope of 269.7 nm/RIU and R2 of 0.9213.

In addition to the 2D clusters I also studied 3D clusters theoretically and experimentally in collaboration with Erik Martinsson in Linköping University. This part of work has been published on *Plasmonics*, and it will be discussed briefly in Chapter 7.

4.2 Experimental Section

Gold spherical nanoparticles with 13 nm diameter are synthesized with sodium citrate as reducing agent[89,204]. The negatively charged AuNPs were coated onto

APTES (3-aminopropyltriethoxysilane) modified glass slide and the density can be controlled by the immersion time[199]. The AuNP SAMs are characterized by FESEM Joel 7600F and UV-Vis absorption spectrometer lambda 35. Absorption spectra are measured by immersing the substrate in PMMA cuvette containing solvents with different refractive indices. The refractive indices are tuned from 1.333 to 1.474 by fraction of glycerol. Simulations are conducted with commercial package FDTD Lumerical. Bulk dielectric function of gold measured by Johnson and Christy in 1972[53] were used in the calculation.

4.3 Conclusions

In summary, the sensitivity of AuNP clusters with different configurations has been studied theoretically. The sensitivity of LSPR sensor can be significantly increased by packing spherical AuNPs into larger configurations together. In 2D plane, the straight and close packed AuNPs demonstrate the highest sensitivity. Experimentally, by forming close packed AuNP SAMs of spherical AuNPs the sensitivity could be improved by 7 times compared to individual AuNPs. The closed packed SAMs provide an easy-to-prepare platform to LSPR sensor with high sensitivity. With e-beam lithography, linear nanostructures with uniform gaps could give even better sensitivity and figure of merit.

Chapter 5: Controlled aggregation of gold nanoparticles and colorimetric Sensor for matrix metalloproteinase 7 (MMP-7)

5.1 Controlled aggregation by complementary peptide and salt

The localized surface plasmon resonance (LSPR) of gold nanoparticles (AuNPs) is strongly dependent on the inter-particle distance. Controlled aggregation of AuNPs provides a straightforward means of tuning the inter-particle distance and thus the optical properties of AuNPs. Recently, controlled aggregation of AuNPs attracts tremendous interest in colorimetric sensing and self-assembly etc. In this study, two strategies to control the aggregation of AuNPs are recognized and utilized for colorimetric sensing, Figure 5.1.

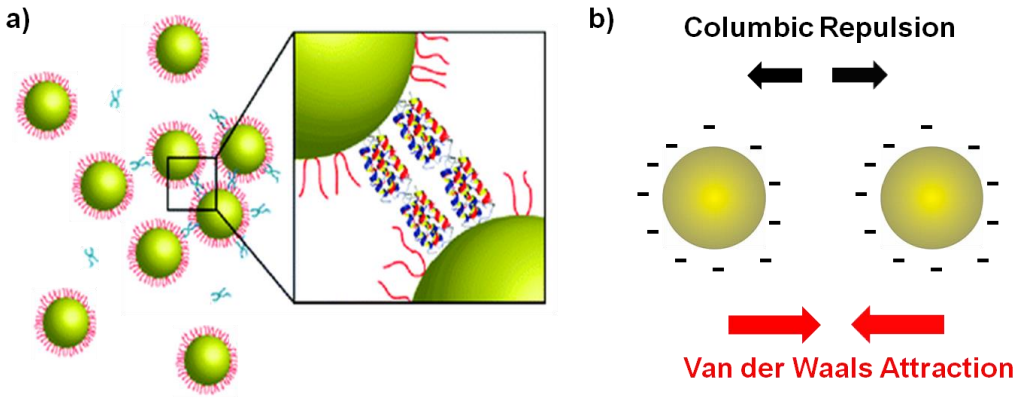

Figure 5.1 (a) Illustration of the aggregation of AuNPs induced by cross-linking molecules. Adapted with permission from ref.[64] Copyright © 2011, American Chemical Society. (b) Illustration of the forces that keep the AuNPs stable in solution. In equilibrium the Van der Waals attraction force between AuNPs equals the columbic repulsive force between charged layers.

The aggregation of AuNPs can be controlled by cross-linking molecules (Type I), such as DNAs, peptides, and proteins etc. Alternatively, the aggregation can be induced by increasing the attractive force or decreasing the repulsive force

between AuNPs (Type II). The repulsive force between AuNPs can be easily reduced by reducing the charges of capping layers.

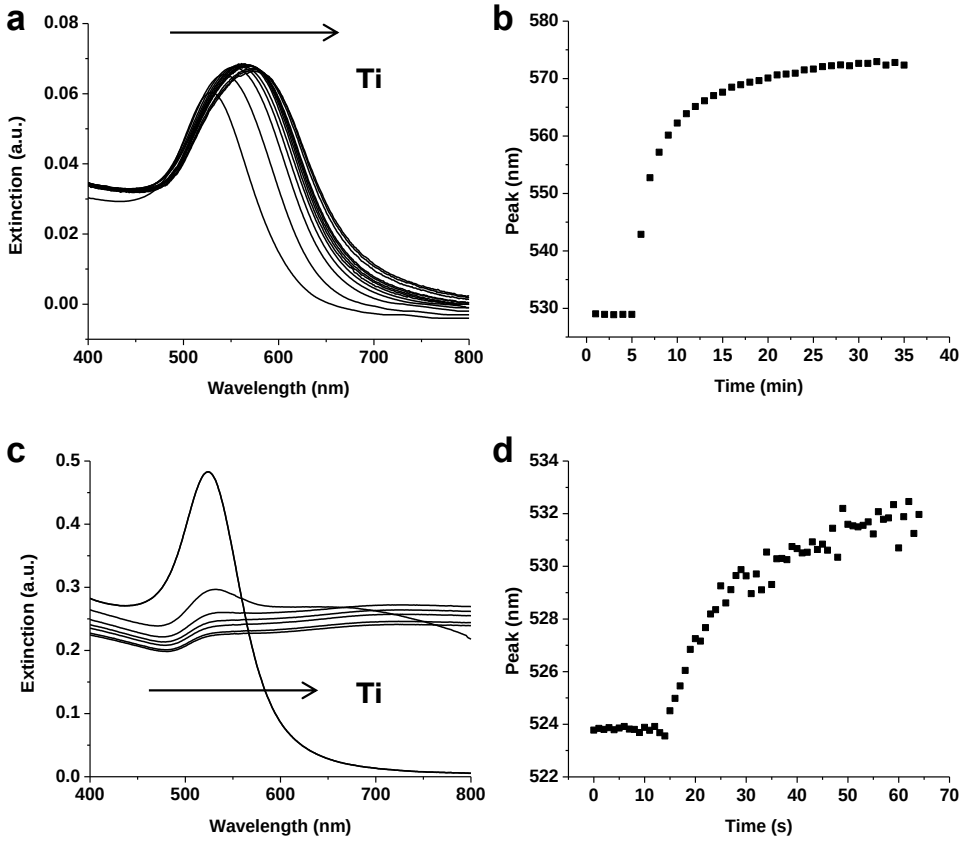

Figure 5.2 (a) Extinction spectra of 20 nm JR2EC functionalized AuNPs with addition of 25 nM $JR2KC_2$ peptide. (b) Peak position of the extinction spectra in (a) after addition of $JR2KC_2$ at different time. (c) Extinction spectra of 20 nm AuNPs with addition of 50 mM NaCl. (d) (b) Peak position of the extinction spectra in (c) after addition of 50 mM NaCl.

Synthetic complementary peptide pairs ($JR2KC_2$ and JR2EC) are able to induce the type I aggregation. Figure 5.2(a) shows the extinction spectra of JR2EC functionalized 20 nm AuNPs with addition of 25 nM $JR2KC_2$. The aggregation gradually shifts the extinction spectra towards red. Figure 5.2(b) summarizes the

evolution of peak position with time. On the other hand, to induce type II aggregation, the columbic repulsive force could be easily reduced, for example by increasing ionic strength to screen the surface charges. Figure 5.2(c) shows the extinction spectra induced by induced by 50 mM NaCl. Similarly, the extinction spectra shift towards red. However, a significant decrease in the intensity of extinction spectra is also observed. The decrease of intensity upon addition of NaCl may come from two factors. Firstly, the precipitate of AuNPs to the bottom of cuvette reduced the concentrations of AuNPs. Secondly, the aggregation created a large variation of different sized aggregates, which appeared as many different but smaller peaks. Figure 5.2(d) summarizes the peak position of the extinction spectra with time.

The peak shift (color shift) of extinction spectra induced by aggregation can be used to monitor bimolecular interaction. Colorimetric sensors utilizing aggregation induced color shift for two target molecules have been developed, namely botulinum and matrix metalloproteinase 7 (MMP-7). Botulinum neurotoxin is considered as one of the most toxic food-borne substances and is a potential bio-weapon accessible to terrorists. The development of an accurate, convenient and rapid assay for botulinum neurotoxins is very important for addressing biosafety concerns. Herein, novel biotinylated peptide substrates designed to mimic synaptosomal-associated protein 25 (SNAP-25) are utilized in gold nanoparticle-based assays for colorimetric detection of botulinum neurotoxin serotype A light chain (BoLcA). The colorimetric sensor for botulinum is based on type I aggregation, where biotinylated peptide is used as a cross-linking

molecule. This work is collaborated with Xiaohu Liu in CBSS, NTU and it will be discussed briefly in Chapter 7. MMP-7 is a zinc dependent endopeptidase, which could degrade extracellular matrix proteins. Its presence and levels is related to many human diseases, e.g. salivary cancers. A colorimetric sensor based on peptide functionalized AuNPs was developed for detect MMP-7. The digestion of peptide decreases the charges and thus the repulsive force of AuNPs, leading to type II aggregation. In addition, the dispersion of AuNPs from previously aggregated particles is also explored and a colorimetric sensor for reduced glutathione (GSH) has been developed in collaboration with Dr. Chia Wei Sheng in CBSS. The presence of GSH changes the color of the sample from colorless to red. This work will be discussed briefly in Chapter 7.

5.2 Colorimetric sensor for MMP-7

Matrix metalloproteinases (MMPs) belong to a group of zinc-dependent endopeptidases which primarily involved in the degrading of the extracellular matrix proteins. Matrix metalloproteinases (MMPs) have attracted considerable attention during recent years because of their large influence on cell behaviour and involvement in numerous human diseases, such as cancer, AIDS, inflammation etc.[205-208] Among those, the concentration of MMP-7 is considered to be an indicator of salivary gland cancer[209] and it also contribute to invasive growth and metastasis of colon caricinoma.[210] Therefore, there is a great need for rapid, specific and sensitive assays MMPs at clinically relevant concentrations for early diagnostics and as a tool for drug screening and development of therapeutics. Over the past decades, many methods have been developed to detect

and study MMPs, including gel electrophoresis,[211,212] enzyme-linked immunosorbent assay (ELISA)[35] and Förster resonance energy transfer (FRET).[113,213] However, these methods are very complicated and require complicated instruments and dedicated laboratories to carry out the test.

The structure of MMP-7 rendered with pyMOL based on PDB data is shown in Figure 5.3(a) and the MALDI-TOF spectrum of MMP-7 is shown in Figure 5.3(b). MMP-7 has a molecular weight of ~19kD and there are two zinc ions and two calcium ions associated with it.

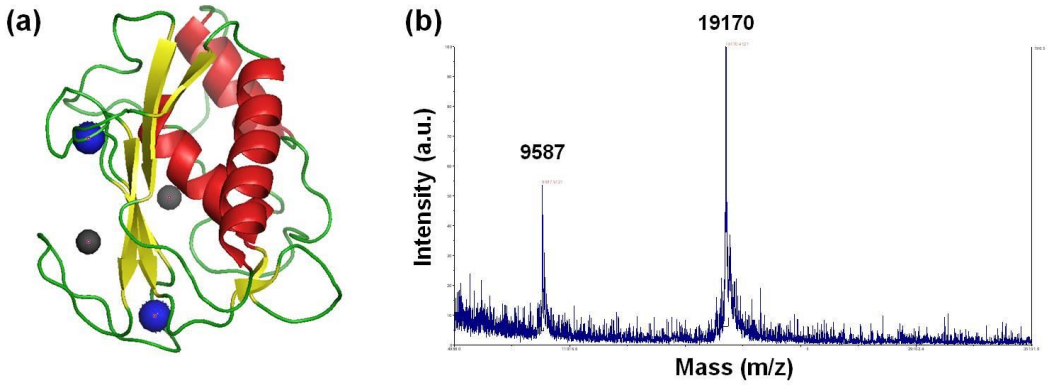

Figure 5.3 (a) Structure of MMP-7 rendered with pyMOL based on PDB data. Bule balls stand for zinc ions and black balls stand for calcium ions. (b) MALDI-TOF spectrum of MMP-7. Reproduced from ref.[12]with permission from The Royal Society of Chemistry.

Gold nanoparticles due to its unique optical and chemical properties[214] have been widely explored for colorimetric detection of DNA,[31,215] proteins,[47] enzymes,[170,216,217] toxic molecules,[68,218,219] and ions[220] as well as for other applications.[95,221,222] Stevens et al. demonstrated a very sensitive assay for a-antichymotrypsin prostate specific antigen (nACT-PSA) based on the re-dispersion of AuNPs upon the hydrolysis of an immobilized oligopeptide.[121] Guarise et al. explored a approach using peptide-based protease substrates with

both C- and N-terminal cysteinyl groups that induced bridging aggregation of AuNPs unless digested by the corresponding protease.[223] This strategy however, used unmodified gold nanoparticles, which is less stable in suspension as they are susceptible to unspecific adsorption of contaminants and other molecular species present in the sample.

Herein, a robust and rapid colorimetric assay for the matrix metalloproteinase matrilysin (MMP-7) was developed using AuNPs with synthetic polypeptide as substrate. The polypeptide (JR2EC) is composed of 42 amino acids and bears 5 negative charges at pH 7. It contains two specific recognition and digestion sites (Ala-Leu and Ala-Gln-Leu) for MMP-7 at position 11 and 26.[174] A cysteine was introduced in position 22[64] to facilitate immobilization to the AuNP surface through thiol-gold chemistry. The peptide functionalized AuNPs are highly stable even at physiological salt concentration.[216] Digestion of the immobilized peptide at specific sites by MMP-7 decreased the net charge of peptide from -5 to -1, which drastically reduced the columbic repulsive force between AuNPs and thus the stability of the AuNPs in suspension. The aggregation of AuNPs upon exposure to MMP-7 results in a distinct concentration dependent LSPR shift, which enables a quantitative monitoring of the presence and activity of the protease. The principle of this colorimetric detection is illustrated in Figure 5.4.

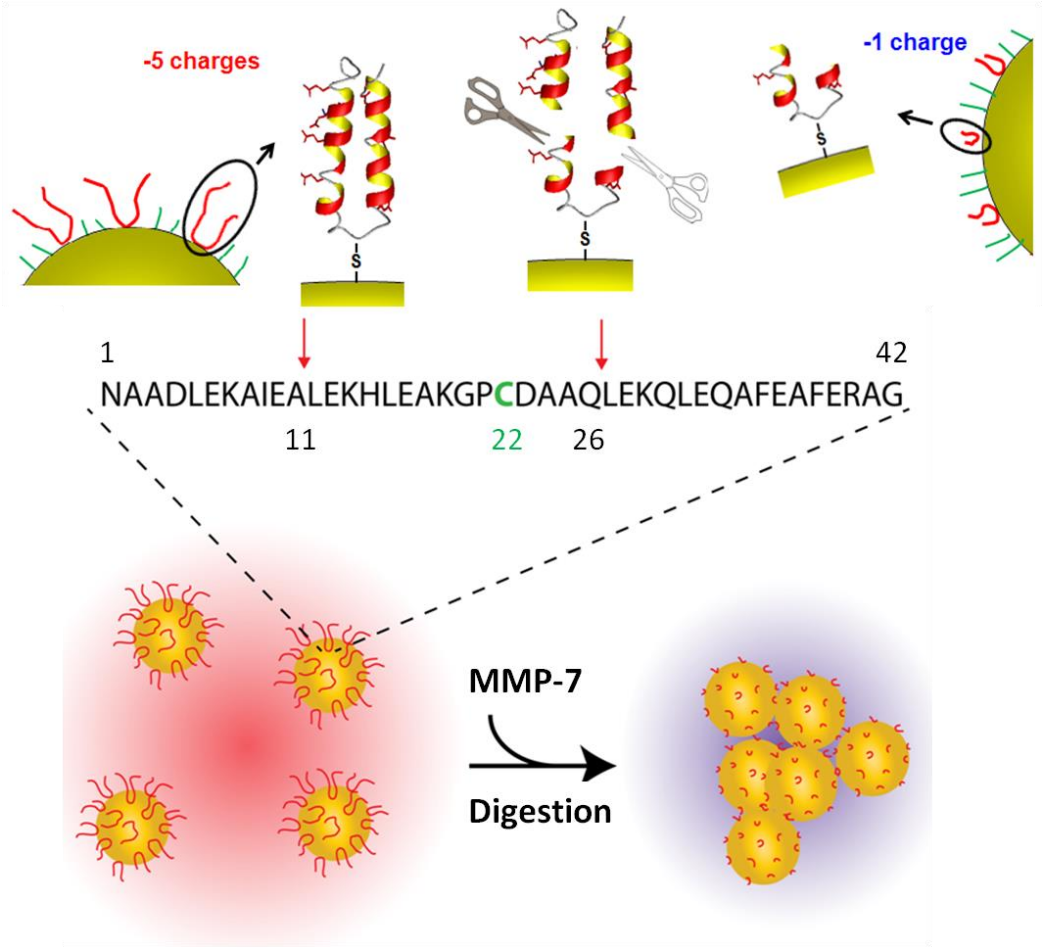

Figure 5.4 Working mechanisms of the colorimetric sensor. The JR2EC peptide contains a cysteine group at position 22 (green), and two digestion sites at 11 and 26 (red arrow). Adapted from ref.[12]with permission from The Royal Society of Chemistry.

To verify the effective digestion of the JR2EC peptide, MALDI-TOF spectroscopy was conducted to observe the mass of peptide before and after digestion. Before digestion the peptide shows a prominent peak 4584 m/z, which corresponds to the mass of peptide (Figure 5.5(a), black). After digestion with MMP-7 the intensity of peak at 4584 m/z decrease and at the same time many small segments at 1368 m/z, 1609 m/z, 1866 m/z, 2736 m/z, 2950 m/z, 3457 m/z are observed (Figure 5.5(a), red). The mass of segments confirms the digestion

sites of position 11 (Ala-Leu) and 26 (Ala-Gln-Leu). The first cleavage site Ala-Leu has been reported previously,[113] and the activity of MMP-7 (k_{cat}/K_m) on the peptide substrate containing the Ala-Leu (HO-Ser-Arg-Trp-Leu-**Ala-Leu**-Pro-Arg-DNP) is 1.9×10^5 $M^{-1}s^{-1}$.[224] The second cleavage site, Ala-Gln-Leu, occurs at the amide bond between Gln and Leu at position 26. Interestingly, the site Gln-Leu is not a digestion site of MMP-7. Moreover, the Gln-Leu bond at the position 30 of the same peptide was not digested at all. It is thus proposed that the second cleavage site is still Ala-Leu, with the Gln in between acting as a spacer. This is in line with the findings in previous work which suggested that Dpa (3-(2,4-Dinitrophenyl)-L-2,3,diaminopropionic acid) could serve as spacer between Ala and Leu. The acitivity of MMP-7 (k_{cat}/k_m) on the peptide substrate containing Ala-Dpa-Leu with Dpa as spacer (H_2N-Arg-**Ala-Dpa-Leu**-Gly-Leu-Pro-MCA) is 1.7×10^5 $M^{-1}s^{-1}$.[224] When both sites at position 11 and 26 are cleaved by MMP-7, the peptide fragment remaining on the AuNPs consist of 15 amino acids. The net charge of the peptide segment of 15 amino acids left on the AuNPs is -1 at pH 7. Compared to the intact 42-mer peptide JR2EC, the net charges decrease significantly from -5 to -1 after digestion with MMP-7. In addition to charges, after 27 amino acids have been cleaved off the JR2EC peptide, the length of peptide segment left on AuNPs is roughly 1/3 of the intact JR2EC peptide (15/42).

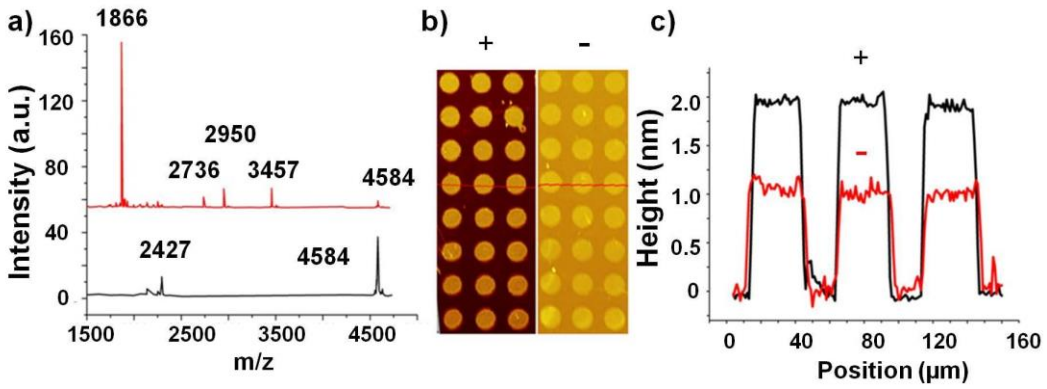

Figure 5.5 (a) MALDI-TOF spectra of the intact JR2EC peptide (black) and JR2EC peptide after incubation with 1 μg/mL MMP-7 for 2 hr at 25 ℃ in PBS buffer with pH 7.4 (red); b) Ellipsometric image of the patterns of JR2EC peptide on gold surface before (+) and after (-) digestion with MMP-7; c) Height profile of JR2EC patterns on gold thin film along the red line in (b) before (black) and after the digestion of MMP-7 (red). The thicknesses reported in the profiles are measured with respect to the hydroxyl-terminated thiol frames. Adapted from ref.[12]with permission from The Royal Society of Chemistry.

The change in length of peptide can be measured with ellipsometry by immobilizing the peptide on gold film. To immobilize the JR2EC onto gold film, firstly the HO-EG_6-C_{11}-S-S-C11-EG_6-NHCO-Maleimide was patterned onto the 200 nm thick gold film by micro contact printing using PDMS stamp and SH-$(CH_2)_{16}$-OH was used to cover other areas. The JR2EC was immobilized on the patterned area through chemical bonding between cysteine and maleimide. Figure 5.5(b) and (c) show the ellipsometric 2D images and height profiles along the red line, respectively of JR2EC patterns on gold surface before and after incubation with 1 μg/mL MMP-7 for 2 hrs. Figure 5.5(c) shows that the total thickness of the pattern decreased from ~2 nm to ~1 nm. After subtracting the thickness difference of ~0.5 nm (HO-EG_6-C_{11}-S-S-C_{11}-EG_6-NHCO-Maleimide is ~0.5 nm thicker than SH-$(CH_2)_{16}$-OH), the thickness of JR2EC layer decreases from 1.5 nm to 0.5 nm.

This change in thickness is consistent with the change in mass from MALDI-TOF data on the free peptide that roughly 2/3 of the peptide was removed from the surface. Most importantly, these data verify that MMP-7 was able to digest JR2EC peptide when immobilized on a gold surface.

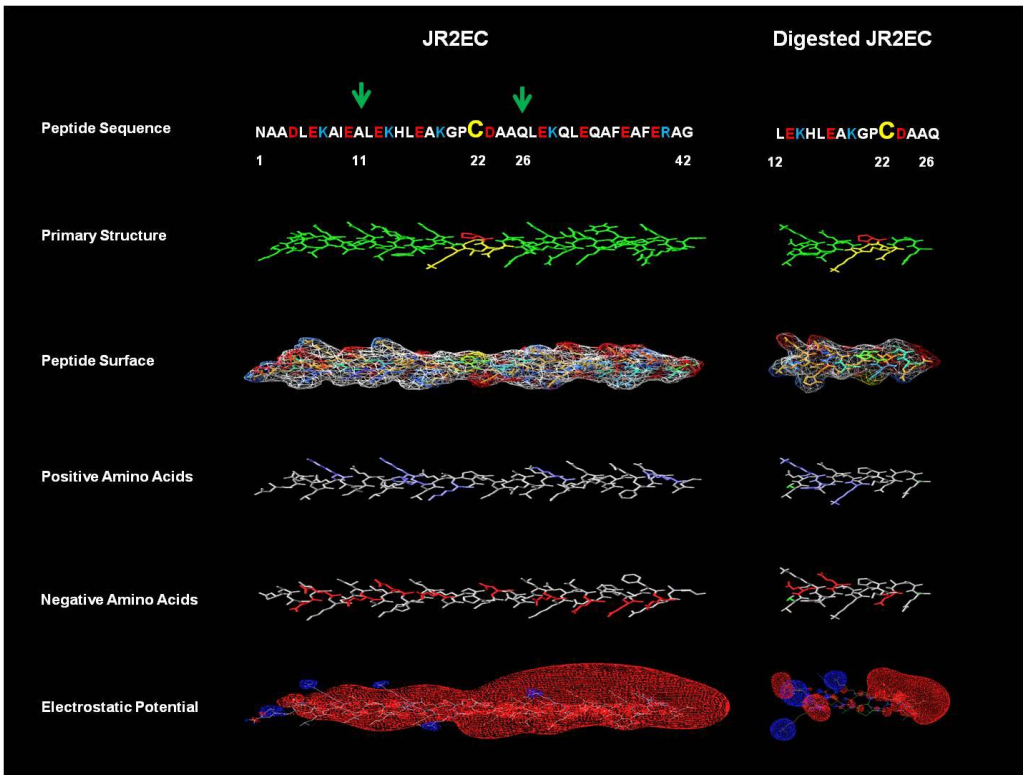

Figure 5.6 Sequence, primary structure, peptide surface, highlight of positive and negative amino acids, and electrostatic potential of intact and digested JR2EC peptide calculated at pH 7. Reproduced from ref.[12]with permission from The Royal Society of Chemistry.

The sequence, primary structure, distribution of positively and negatively charged amino acids are highlighted in Figure 5.6. The net charges of peptide before (-5) and after digestion (-1) with MMP-7 can be calculated from the number of positively charged and negatively charged amino acids. More accurately, the distribution of electrostatic potential can be calculated to visually illustrate the

impact of digestion on surface charges. As shown in Figure 5.6, the red color stands for negative electrostatic potential while the blue color stands for positive electrostatic potential. After digestion with MMP-7, the negative electrostatic potential decreases significantly.

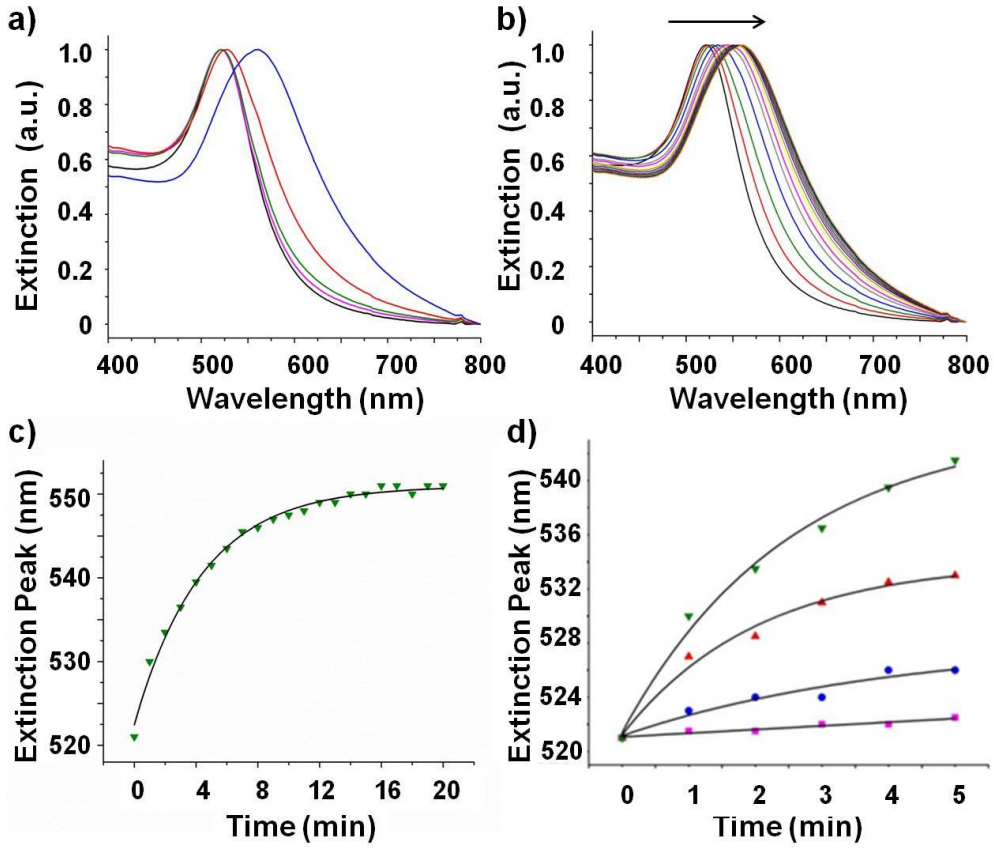

Figure 5.7 (a) UV-Vis extinction spectra of citrate-capped AuNPs (black) and JR2EC modified AuNPs after exposure to MMP-7 (blue), MMP-2 (red), MMP-7 with 10 μM inhibitor II (green) and MMP-7 with 10 mM EDTA (pink), respectively in PBS at pH 7.4. (b) Sequential extinction spectra of JR2EC modified AuNPs obtained during 30 min in the presence of 2 μg/mL MMP-7. (c) Plot of the evolution of the extinction maximum with time in the presence of 4 μg/mL MMP-7 in 20 min. Data points were fitted with exponential curve, the R^2 of which is equal to 0.9928. (d) Evolution of the extinction maximum with time for MMP-7 at different concentrations from top to bottom: 4 μg/mL, 2 μg/mL, 0.5 μg/mL and 0.1 μg/mL, respectively. Adapted from ref.[12] with permission from The Royal Society of Chemistry.

Figure 5.7(a) shows the UV-Vis extinction spectra of JR2EC functionalized AuNPs treated with MMP-7. The peak of the LSPR band after 30 min incubation with 2 μg/mL MMP-7 appears at 561 nm, i.e. a shift of ~ 40 nm is observed. This redshift is due to the increased optical coupling between the AuNPs because of the nanoparticle aggregation.[31,82] Extinction spectra of bare JR2EC functionalized AuNPs as well as JR2EC functionalized AuNPs digested with MMP-2, MMP-7 with inhibitor II and MMP-7 with EDTA, respectively. None of the control experiment show significant response as that of MMP-7. MMP-2 is a similar zinc depend enzyme to MMP-7 in the MMP family that cleaves peptide at sites not present in JR2EC.[205,208]

The stability of the AuNP colloidal system is determined by two main factors: van der Waals attraction of AuNPs, and columbic electrostatic repulsion governed by identically charged peptides as described by Derjaguin−Laudau−Verwey−Overbeck (DLVO) theory.[225] The MMP-7 mediated digestion of JR2EC reduces the net negative charge of the immobilized peptide from -5 to -1, which significantly reduces the columbic electrostatic repulsion. On the other hand, the van der Waals attraction, however, is determined by the core of AuNPs, which is not affected much by digestion of peptide. As a result, the net attraction force induced by MMP-7 digestion leads to the aggregation of the AuNPs. Figure 5.8 shows the TEM image of JR2EC modified AuNPs before and after incubation with 2 μg/mL MMP-7. Before addition of MMP-7, the AuNPs are very well dispersed. After addition of MMP-7, the AuNPs aggregate a lot and

the average distance between AuNPs after addition of MMP-7 is around 3.5 nm, which is expected to give significant color shift due to coupling effect.

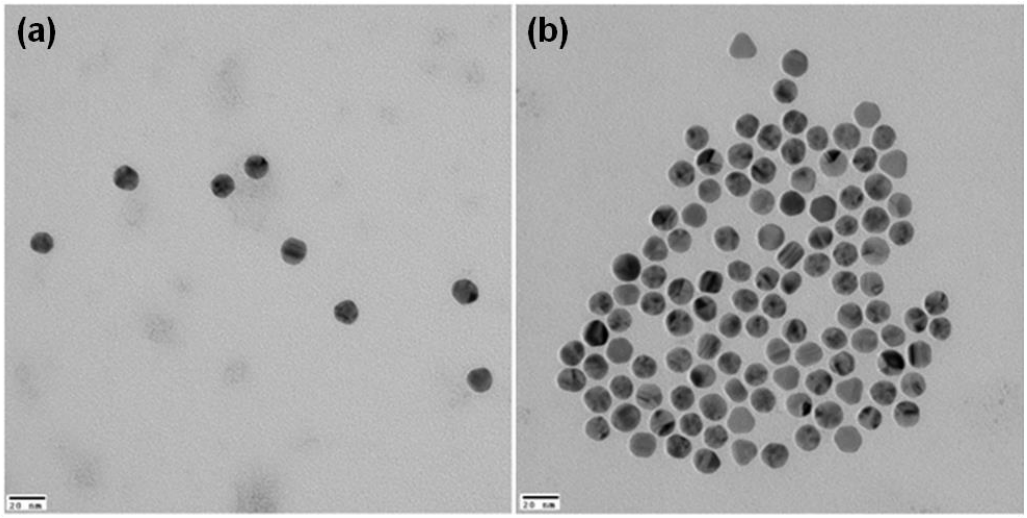

Figure 5.8 TEM images of the peptide functionalized AuNPs (a) before and (b) after 2 μg/mL MMP-7 digestion. Scale bar: 20 nm. Adapted from ref.[12] with permission from The Royal Society of Chemistry.

MMP-7 utilizes both Zn^{2+} and Ca^{2+} as cofactors. The absence of aggregation of AuNPs is evident when the MMP-7 was incubated with 10 mM Ethylenediaminetetraacetic acid (EDTA) or 10 μM MMP inhibitor II (Figure 5.7(a)). The activity of MMP-7 depends strongly on the two Zn^{2+} and two Ca^{2+} in the enzyme. EDTA can potentially chelate both cations while inhibitor II binds specifically to the catalytic zinc ion.[226] The IC_{50} of the MMP inhibitor II to MMP-7 is 30 nM.[227] Moreover, no particle aggregation was obtained upon addition of MMP-2, as expected as it has no reported activity on the peptide sequence used.[213] These control experiments demonstrate that the LSPR shift originates from a specific digestion of the peptide by MMP-7. Moreover, the aggregation

was very quick and a distinct response was obtained within minutes after addition of MMP-7. Figure 5.7(b) shows 10 sequential extinction spectra of AuNPs after addition of 2 μg/mL MMP-7. The LSPR peak gradually shifts from 521 nm to about 560 nm. Figure 5.7(c) shows the shift of the extinction spectrum over time upon introduction of 4 μg/mL MMP-7 into the JR2EC functionalized AuNP solution. The observed LSPR peak shift upon introducing MMP-7 was fitted to an exponential function. The kinetics of the peak shift depend strongly on the concentration of the MMP-7 present in the JR2EC functionalized AuNPs solution, see Figure 5.7(d).

Figure 5.9(a) shows a typical set of UV-Vis spectra of JR2EC functionalized AuNPs incubated with different concentrations of MMP-7 at 25 ℃ for 4 minutes. Figure 5.9(b) summarizes the LSPR peak positions of the JR2EC functionalized AuNP suspensions incubated with different concentration of MMP-7 for 0 min, 2 min, 4 min, 8 min and 20 min, respectively. For the short time incubations (2 min, 4 min and 8 min) the LSPR peak increases with the MMP-7 concentration following an exponential decay curve. However, at 20 min incubation, a deviation from exponential decay curve is observed, which is attributed to the saturation of aggregation. At time 4 min, a roughly linear relationship was observed for concentrations up to 2 μg/mL of MMP-7, Figure 5.9(c). An estimated limit of detection based on three time of standard deviation of baseline is ~ 47.2 ng/mL (2.4 nM) for the present assay. The concentration of MMP-7 in saliva in healthy people is as low as 3.1 ± 0.66 ng/mL, [228] while the levels of MMP-7 in salivary gland cancer patients typically vary between 100 ng/mL to a few μg/mL

depending on the stage of disease development. Interestingly, at high concentrations of 2 μg/mL, the aggregation of AuNPs brings obvious color difference, Figure 5.9(d). Therefore, this platform shows a great promise for development into an easy to use diagnostic tool for detection of salivary gland cancer without the need of sophisticated instrumentation.

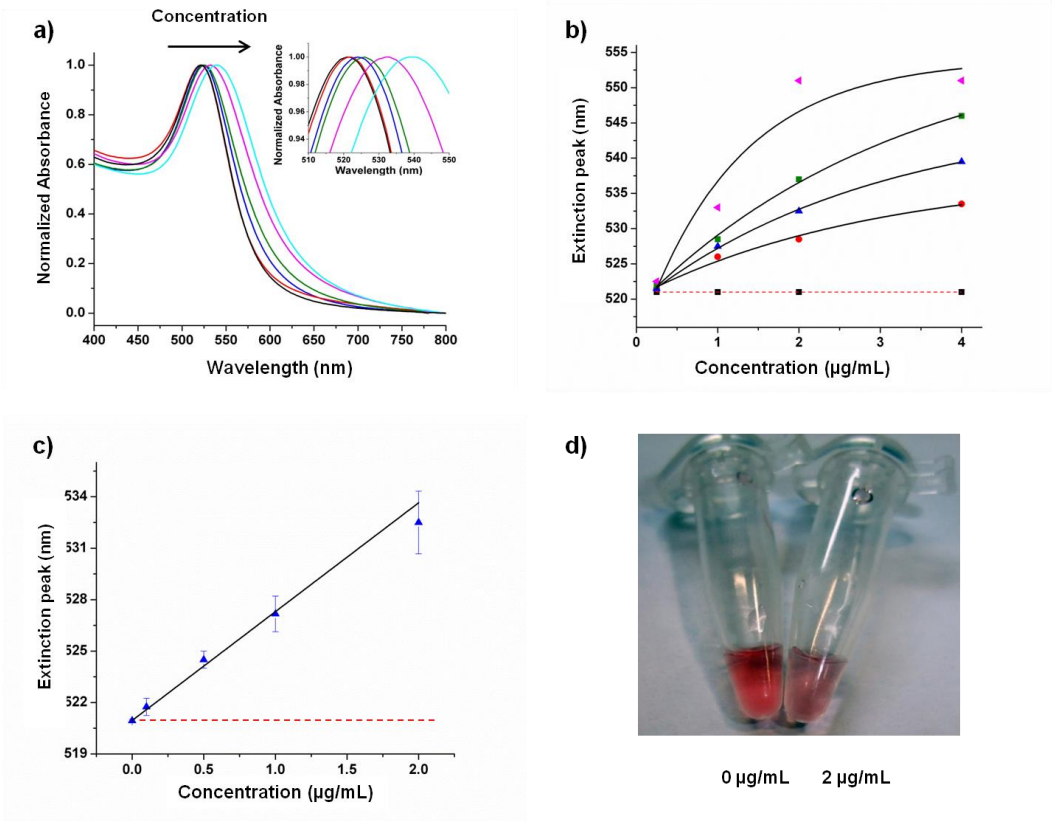

Figure 5.9 (a)Normalized extinction spectra of JR2EC modified AuNPs at different concentrations of MMP-7 from left to right is 0 μg/mL, 0.1 μg/mL, 0.5 μg/mL, 1 μg/mL, 2 μg/mL, and 4 μg/mL, respectively at time 4 min. Inset: zoom in extinction spectra. (b) LSPR peak position versus MMP-7 concentration incubated for different time from bottom to top: 0, 2, 4, 8 and 20 min, respectively. (c) LSPR peak position versus MMP-7 concentration (black line). The dashed line represents the extinction peak position plus 3 times of standard deviation (σ = 0.1 nm) of the JR2EC functionalized AuNPs which is used to determine the limit of detection (LOD). (d) Photos of JR2EC modified AuNPs without MMP-7 and with 2 μg/mL MMP-7 incubated for 20 min. Adapted from ref.[12] with permission from The Royal Society of Chemistry.

5.3 Experimental Section

Ethylenediaminetetraacetic acid (EDTA), Gold (III) Chloride Trihydrate (>=99.9%), sodium citrate tribasic dihydrate (ACS reagent, >=99.0%), α-Cyano-4-hydroxycinnamic acid (CHCA) and calcium chloride were purchased from Sigma-Aldrich. Phosphate Buffered Saline (PBS) Ultra Pure Grade and Bis-tris buffer were purchased from 1st base. MMP-7 human recombinant, E. Coli and MMP-2 human recombinant, E. Coli and MMP inhibitor II (N-Hydroxy-1,3-di-(4-methoxybenzenesulphonyl)-5,5-dimethyl-[1,3]-piperazine-2-carboxamide) were purchased from Merck Chemicals. The SH-$(CH_2)_{16}$-OH and the HO-EG_6-C_{11}-S-S-C11-EG_6-NHCO-Maleimide used as the PDMS inking and backfilling anchoring molecules, respectively, in the ellipsometric microarray experiments, were purchased from Prochimia, Poland. O-(7-benzotriazole-1-yl)-1,1,3,3-tetramethyluronium tetrafluoroborate was purchased from TBTU, Alexis Biochemicals.

The peptide JR2EC (NAADLEKAIE**AL**EKHLEAKGPCDA**AQL**EKQLEQA-FEAFERAG) was synthesized on a Pioneer automated peptide synthesizer (Applied Biosystems) using standard fluorenylmethoxycarbonyl (Fmoc) chemistry with O-(7-benzotriazole-1-yl)-1,1,3,3-tetramethyluronium tetrafluoroborate as the activating reagent. The peptide was dissolved in 10 mM sodium citrate buffer with pH 6.

Gold nanoparticles with a diameter of ~17 nm were obtained by the citrate reduction of $HAuCl_4$[1, 2] and stored at 4 ℃ until further use. UV-Vis extinction spectrum of the as-synthesized and citrate capped AuNPs showed a plasmonic peak around 520 nm. Functionalization of the AuNPs was performed by

incubation of the particle in the 10 μM peptide solution at pH 6 (10 mM sodium citrate). The unbound peptide was removed by 5 repeated centrifugations followed by washing with PBS buffer at pH 7.4, and stored until further use. Before use, the buffer of the JR2EC functionalized AuNPs was changed to PBS buffer with 1 mM $CaCl_2$ at pH 7.4. After functionalization, the extinction peak of the AuNPs appeared at 521 nm.

Patterning of the peptide on gold surface was prepared by micro contact printing of a hydroxyl-terminated alkane thiol to form a frame followed by backfilling with a maleimide disulphide in the non-printed domains (diameter 30 μm).[3] In a typical printing process, the PDMS stamp was soaked in a 5 mM SH-$(CH_2)_{16}$-OH solution for 1 min followed by drying in nitrogen gas before it was brought into conformal contact with the gold surface for 5 min. The printed gold surface was then incubated in a 50 μM maleimide (HO-EG_6-C_{11}-S-S-C_{11}-EG_6-NHCO-Maleimide) for 1 hr followed by incubation in 40 μM peptide solution in PBS buffer for 12 hrs. Imaging ellipsometry was conducted using a modified EP3 spectroscopic ellipsometer from Accurion, Germany. During the ellipsometric profile measurements the OH-thiol areas were used as reference positions for calculating the incremental thickness changes upon exposure to the maleimide disulphide, immobilization of the JR2EC peptide and after digestion. For example, the thickness difference between the OH-thiol and the maleimide disulphide was approximately 0.5 nm. This particular thickness must be subtracted when evaluating the thickness of peptide before and after digestion.

The MMP-7 mediated hydrolysis of the immobilized peptides was performed at 25 ℃ and real time extinction spectra were recorded with the Lambda 35 spectrometer during 30 min. Control experiments were performed using 2 μg/mL MMP-2, 2 μg/mL MMP-7 with 10 μM MMP inhibitor II and 2 μg/mL MMP-7 with 10 mM ethylenediaminetetraacetic acid (EDTA), respectively. Digestion of the peptide in PBS buffer was characterized by MALDI-TOF-MS using a Shimadzu mass spectrometer with α-Cyano-4-hydroxycinnamic acid (CHCA) as matrix. A solution containing 10 μM of the peptide in PBS pH 7.4 was digested with 1 μg/mL MMP-7 for 2 hr at 25 ℃. The digested sample was desalted before MALDI-TOF experiment. Digestion of the peptides on planar gold by MMP-7 was evaluated by measuring the height profile of peptide-patterned gold surfaces using imaging ellipsometry.

5.4 Conclusions

In summary, we have reported an assay format for detecting MMP-7 based on polypeptide functionalized gold nanoparticles. It enables rapid (4 min) and easy colorimetric detection as well as accurate quantitative analysis. The robustness of the synthetic peptide and gold nanoparticles enables the assay to be employed in harsh environments. Therefore, this easy and robust sensing platform can be developed into an attractive assay for field applications since no analytical tools are required in order to monitor the read out. The simplicity of the used colorimetric approach is particularly important when designing cheap and robust kits for remote field-testing in resource limited countries.

The aggregation of AuNPs is driven by the reduced electrostatic repulsion force from the digestion of peptide. There is no binding of cross-linking molecules involved. This sensitivity of this type of aggregation is not limited by the amount of cross-linking molecules. In principle, this type of sensor can be very sensitive, given enough time to allow the enzyme to digest more peptide.

Chapter 6: Towards a LSPR and Raman hybrid sensing

6.1 LSPR and Raman hybrid sensing chip

Localized surface plasmon resonance is widely used to monitor molecular binding. The refractive index dependent resonance frequency is very useful to monitor the amount of molecules adsorbed to the particle surface as well as the binding kinetics, etc. However, the LSPR sensor is not able to give molecular information of the target molecule itself. Thus, the LSPR sensor is not a spectroscopic tool. Instead, the identification of the target molecule relies on the specific interaction between target molecule itself and the immobilized receptor. As a result, the LSPR sensing is not able to differentiate the response induced by binding of impurities from the response from the target. This problem is especially important for detection in real samples, where the matrix contains a lot of biomolecules besides the target molecule. To solve this problem, a hybrid sensing platform is proposed, where the Raman scattering from the target molecules is measured together with LSPR response. Raman scattering offers fingerprinting of the target molecules. In principle, by combining the two complementary techniques, the hybrid sensor is capable of monitor the molecular interaction in real time quantitatively and it is also capable of identifying the molecule adsorbed to the particle. With this platform, for sensing in real samples false readings from other molecules could be excluded. Thus, it is a more reliable platform than the LSPR sensor alone where only one kind of signal is monitored. The LSPR response is monitored by UV/Vis absorption spectrometer while the Raman scattering is

monitored by Raman spectrometer. Figure 6.1 shows the structure of a typical hybrid platform.

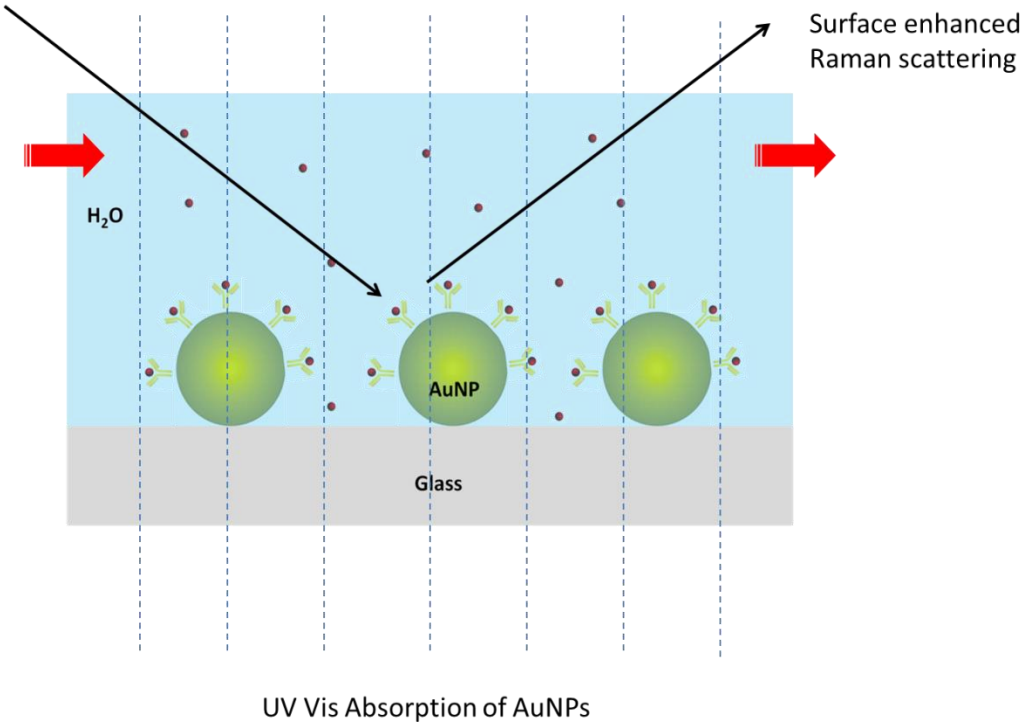

Figure 6.1 Illustration of a hybrid sensing platform. The LSPR response is monitored with UV/Vis absorption spectrometer while the Raman scattering is monitored by a Raman spectrometer.

One of the major problems of this type of sensor is that Raman scattering is very weak. Many Raman active molecules also display a strong fluorescence. Thus, Raman scattering is easily overwhelmed by the fluorescence background [42,229,230] due to the smaller Raman cross section (10^{-22} cm^2) compared to the strong fluorescence (10^{-16} cm^2).[231,232] Therefore, the signal-to-background (S/B) ratio is much too low to resolve the characteristic peaks of Raman scattering of organic molecules from the large fluorescence background.[230,231] Traditional efforts to

solve this problem mainly utilize surface enhanced Raman scattering (SERS), *i.e.* noble metal nanostructures are used to enhance the Raman scattering.[48,137,138,199,233] Very recently, an alternative was proposed where graphene is used to quench the strong fluorescence.[234] Although the aforementioned methods improve the S/B ratio to a certain extent, there are still much room to improve, especially if one considers the fact that the fluorescence is ~6 orders of magnitude stronger than Raman scattering.[231,232] To further increase the S/B ratio, we report on a novel method to simultaneously enhance the Raman scattering and reduce the fluorescence by assembling graphene oxide (GO) and $Au_{0.7}Ag_{0.3}$ alloy nanoparticles (NPs) on a SiO_2 substrate. A highly fluorescent molecule, Alexa fluor 488, is used in this experiment as Raman reporter to demonstrate the capability of the Raman substrate. To the best of our knowledge, it is the first report discussing the improvement of S/B ratio of a highly fluorescent molecule by integration of Raman enhancement from noble metals and fluorescence quenching from graphene.

Confocal Raman spectrometer with Argon ion laser of 488 nm was used in the Raman scattering measurement. In order to excite strong surface plasmon, the resonance frequency of the plasmonic nanoparticles should match with the laser. For the most common gold and silver spherical nanoparticles, the resonance wavelength is around 520 nm and 400 nm, respectively. One way to tune the resonance wavelength to 488 nm is to mix the two metals to form an alloy Au_xAg_y.[103] Alloy NPs with different molar fraction of gold were synthesized and the peak wavelength is plotted with fraction of gold in Figure 6.2(a). The peak

wavelength is a linear function of the molar fraction of gold. Therefore, it is easily calculated that in order to have the resonance wavelength at 488 nm, the molar fraction of gold should be ~70% ($Au_{0.7}Ag_{0.3}$ NP). Figure 6.2(b) shows the extinction spectrum of $Au_{0.7}Ag_{0.3}$ NPs and the peak position is at 489 nm. Figure 6.2(c) shows the TEM image of the $Au_{0.7}Ag_{0.3}$ NP, and the size of which is around 40 nm. EDX spectroscopy was conducted to analyze the composition of the $Au_{0.7}Ag_{0.3}$ NP and the molar fraction of gold is measured to equal 69.5%, Figure 6.2(d).

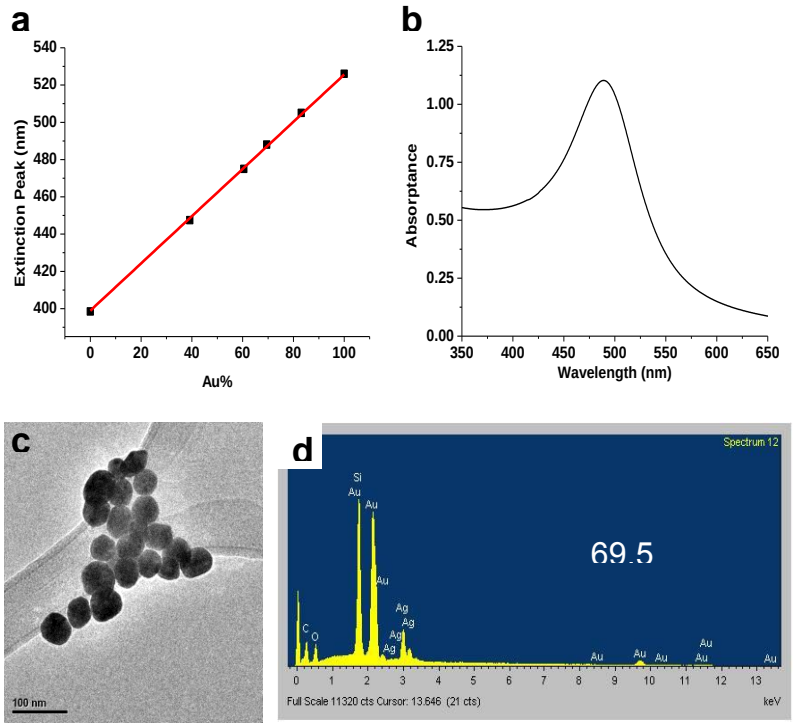

Figure 6.2 (a) Peak of extinction spectra of AuAg alloy NPs with different molar fraction of Au (dots). The fitted curve (red line) shows a slope of 1.27 nm/1%Au and R^2 of 0.9993 (b) Extinction spectrum of $Au_{0.7}Ag_{0.3}$ NPs. The peak position of this spectrum is 488 nm. (c) TEM image of the $Au_{0.7}Ag_{0.3}$ NPs. (d) Energy-dispersive X-ray spectroscopy (EDX) spectrum of $Au_{0.7}Ag_{0.3}$ NPs. The molar percentage of Au is measured to equal 69.5%.

Graphene, a single layer of hexagonally arranged sp^2 carbon atoms was discovered in 2004 and received noble prize in 2010.[148,149] It has been attracted tremendous research interests due to its unique electronic, quantum confinement, optical, and mechanical properties since its discovery.[150] Among those properties, the excellent fluorescence quenching property was recently explored in biosensing,[33] as well as resonance Raman scattering[95] etc. Many methods have been developed to fabricate graphene, including mechanical cleavage from graphite,[148] CVD growth[139] and chemical oxidization.[155] Graphene oxide (GO), an oxidized derivative of single carbon atoms-graphene share the properties of graphene. Moreover, it has many advantages over graphene. Firstly, graphene oxide is easily synthesized in large scale. Secondly, graphene oxide is very easy to modify chemically based on the functional groups available such as hydroxyl groups, carboxylic groups and epoxy groups.[156,235] GO was synthesized using the modified Hummer's method.[155,236] GO sheets were adsorbed onto (3-Aminopropyl)triethoxysilane (APTES) modified SiO_2 substrate by electrostatic attraction. Atomic Force Microscope (AFM) image of GO on SiO_2 substrate is shown in Figure 6.3(a) and the height profile along the red line is shown in Figure 6.3(b). The thickness of the single layer GO measured is ~0.8 nm, which is consistent with previous report.[237]

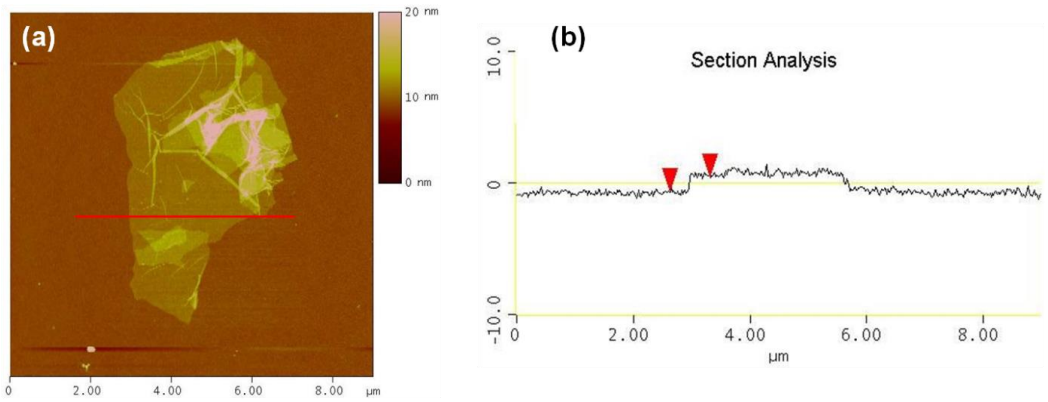

Figure 6.3 (a) atomic force microscope (AFM) image of as-synthesized GO on SiO_2 substrate. (b) The height profile along the red line in (a).

Figure 6.4 shows the assembly process of graphene oxide (GO) and $Au_{0.7}Ag_{0.3}$ nanoparticles (NPs) on SiO_2. GO was synthesized by the modified Hummers method.[157] The as synthesized GO was then treated with sodium hydroxide solution to activate the carboxylate groups.[238] The activated GO is negatively charged because of the carboxylic groups. It was then adsorbed onto 3-aminopropyltriethoxysilane (APTES)-modified SiO_2 surface. The activated GO sheet was functionalized with ethylene diamine by forming amide bond.[239] The reaction between carboxylic acid group and amine group is mediated by NHS and EDC, the well-known chemistry. After ethylene diamine modification, the GO sheet become positively charged. The negatively charged $Au_{0.7}Ag_{0.3}$ NPs were adsorbed onto the positively charged amine-functionalized GO (FGO) surface through electrostatic attraction. The final Raman substrate was referred to as SiO_2/FGO/Au-Ag NP.

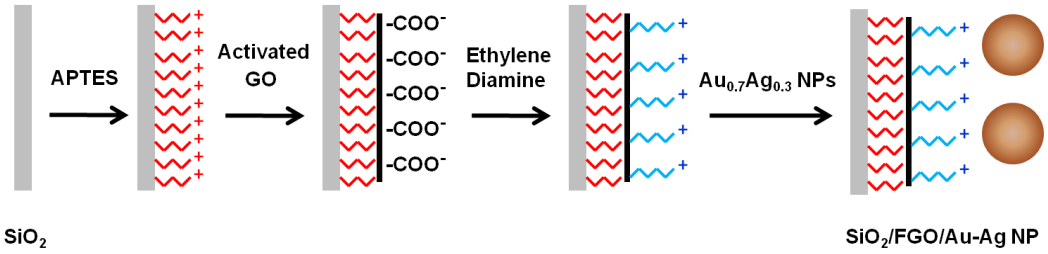

Figure 6.4 Illustration of the assembly process of graphene oxide and $Au_{0.7}Ag_{0.3}$ NPs on SiO_2 substrate. Reprinted with permission from ref.[95] Copyright © 2011, American Chemical Society.

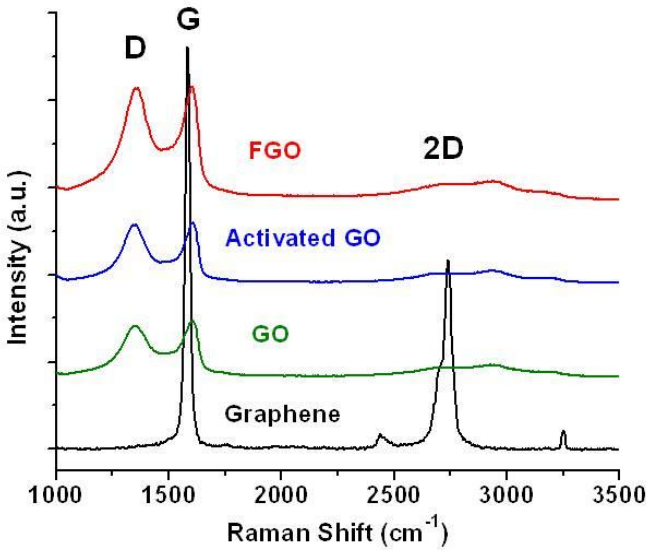

Figure 6.5 Raman spectra of graphite flakes, GO, activated GO and functionalized GO (FGO). Adapted with permission from ref.[95] Copyright © 2011, American Chemical Society.

The surface modification of GO was characterized with Raman scattering. Figure 6.5 shows the Raman spectra of graphene and GO with different functionalization. The mechanically cleaved graphene shows a sharp peak, which corresponds to the first order scattering of E_{2g} mode (G band)[240] at 1584 cm^{-1} and

the second-order zone boundary mode (2D band)[241] at 2700 cm^{-1}, respectively. The characteristic peak at 1350 cm^{-1}(D band), due to zone-boundary phonons, however, was not observed in graphene.[242] The GO sheets contain many oxygen rich functional groups,[243] which changed the Raman scattering mode from that of graphene, which can be seen from the higher D band and lower 2D band in the Raman spectrum of GO (green spectrum in Figure 6.5). In addition, G band is blue shifted to 1600 cm^{-1}. This shift is also attributed to the doping from oxygen-rich functional groups.[244] The G/D ratio is a very good indication of the presence of the surface functionalities. After the activation with NaOH, an increase in D/G ratio from 0.69 to 0.79 was observed for GO (blue spectrum in Figure 6.5). The NaOH activation process activated the carboxylic groups for amine coupling reaction.[238] During this process, however, some oxygen-rich groups were also removed from GO surface.[245,246] The coupling reaction of diamine molecules with the carboxylic groups on GO surface did not bring more changes in the D/G ratio (red spectrum in Figure 6.5), suggesting that the reaction only occurred at the existing carboxylic groups. The constant position of G band also confirms that the coupling reaction did not induce changes on the basal plane of GO.

Figure 6.6 shows the secondary electron image of the as prepared substrate SiO_2/FGO/Au-Ag NP. The black sheet with wrinkles are graphene oxide and the while dots are $Au_{0.7}Ag_{0.3}$ NPs. Dye molecule was immobilized on the GO surface through reaction with the amine group.

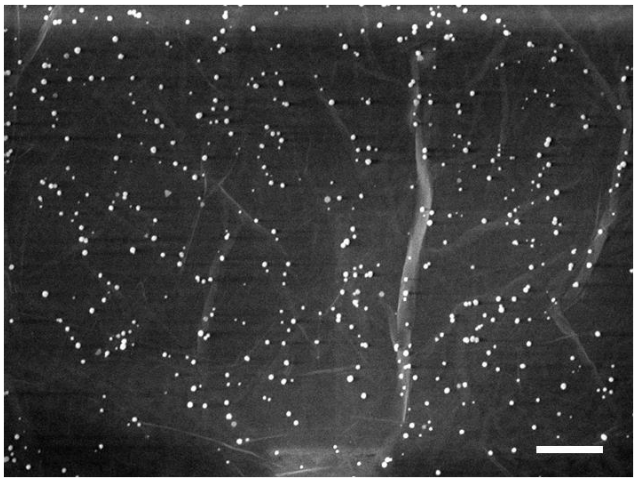

Figure 6.6 FESEM image of SiO2/FGO/Au-Ag NP substrate. Scale bar: 500 nm. Adapted with permission from ref.[95] Copyright © 2011, American Chemical Society.

Briefly, 1 μM Alexa fluor 488 with succinimidyl ester in sodium bicarbonate buffer solution was applied onto the FGO surface and then incubated for 10 min to allow for the reaction. The substrates were then rinsed carefully with DI water to remove excess dye molecules. Resonance Raman spectroscopy (RRS) was then conducted to measure the Raman scattering and the fluorescence of the Alexa fluor 488 on different substrates. Three other substrates, *i.e.* APTES-modified SiO_2, SiO_2/FGO, and SiO_2/Au-Ag NP, were used in control experiment for comparative studies.

The SiO_2 substrate is not plasmonic materials and it has no enhancement on neither Raman scattering nor fluorescence. With the excitation wavelength of 488 nm, the molecule Alexa fluor 488 is highly fluorescent, which overwhelms the weak Raman scattering, see the red spectrum in Figure 6.7(a) (note the scale of 1/5). This observation is in good agreement with the fact that the cross section of

Raman scattering (cross sections of 10^{-22} cm^2) is much lower than that of fluorescence (cross sections of 10^{-16} cm^2). With the high fluorescence background even the Raman peak of silicon ~ 520 cm^{-1} can not be observed.

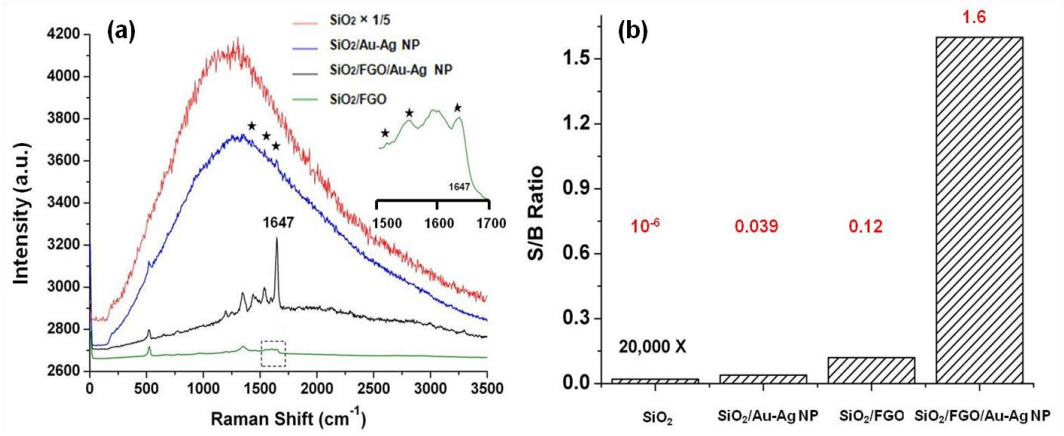

Figure 6.7 (a) Raman spectra of Alexa fluor 488 on the SiO_2, SiO_2/Au-Ag NP, SiO_2/FGO/Au-Ag NP and SiO_2/FGO, respectively. Characteristic peaks of Alexa fluor 488 in the blue spectrum are indicated by stars. The intensity of the spectrum on SiO_2 is divided by a factor of 5. Inset: Zoom in of the Raman spectrum of Alexa fluor 488 on SiO_2/FGO in the area of dotted square of green spectrum. (b) S/B ratio of different substrates: SiO_2 (10^{-6}), SiO_2/Au-Ag NP (0.039), SiO_2/FGO (0.12) and SiO_2/FGO/Au-Ag NP (1.6), respectively. Reprinted with permission from ref.[95] Copyright © 2011, American Chemical Society.

The SiO_2/Au-Ag NP substrate, however, was able to enhance the Raman scattering due to the near fields around the particles. As shown in the blue curve of Figure 6.7(a), the SiO_2/Au-Ag NP substrate gave weak Raman peaks sit on the top of a high fluorescence background. Although fluorescence emission still made the Raman spectrum very noisy, at least a few Raman peaks can be distinguished, as indicated by the stars. Besides the enhancement to Raman scattering, the intensity of fluorescence from Alexa 488 also reduced by 85% compared to SiO_2

(the red spectrum in Figure 6.7(a). This reduction in fluorescence is due to the fluorescence quenching from the Au-Ag NPs.

In addition to the aforementioned strategy for purely enhancing the Raman scattering, the SiO_2/FGO substrate was used to quench the high fluorescence emission. As shown by the green spectrum in Figure 6.7(a), the SiO_2/FGO substrate could virtually eliminate all the fluorescence emission from the Alexa fluor 488. This observation agrees with the previous study that graphene is a much better fluorescence quencher than noble metals.[139] From the inset in Figure 6.7(a), the Raman characteristic peaks of the Alexa fluor 488 molecules in region of 1500-1700 cm^{-1} are clearly resolved.

The SiO_2/FGO/Au-Ag NP substrate could enhance Raman scattering and quenching fluorescence at the same time. As shown by the black curve in Figure 6.7(a), SiO_2/FGO/Au-Ag NP substrate gives a very nice Raman spectrum with clear Raman peaks and low fluorescence background. The most significant peak at ~1647 cm^{-1} is attributed to the stretching vibration of the C=C bonds in the ring structure.[137,247] The S/B ratio (signal-to-background) calculated using the intensity of this peak and fluorescence intensity at this position is summarized in Figure 6.7(b). The ultrahigh S/B ratio of 1.6 was achieved using the SiO_2/FGO/Au-Ag NP substrate, which is 10^6 higher than that on SiO_2.

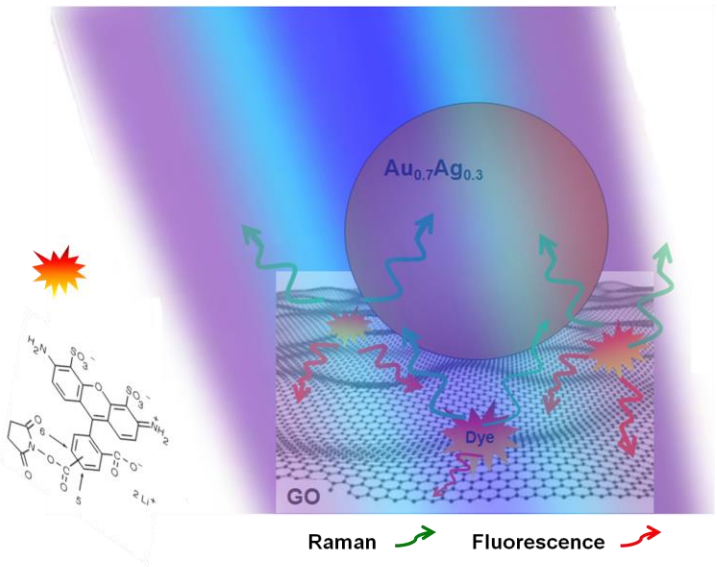

Figure 6.8 The working principle of the SiO2/FGO/Au-Ag NP substrate. Adapted with permission from ref.[95] Copyright © 2011, American Chemical Society.

The working principle of the substrate is illustrated in Figure 6.8. Dye molecules were attached on the FGO surface by covalent bond. No molecules were expected on $Au_{0.7}Ag_{0.3}$ NPs because of the electrostatic repulsion between the negatively charged NPs and the negatively charged dye molecules. With illumination of the laser at 488 nm, the fluorescence from whatever dye molecules on the surface is quenched by FGO. On the other hand, the Raman scattering of these dye molecules in the close proximity of the $Au_{0.7}Ag_{0.3}$ NPs is enhanced.

Some reports also suggest that graphene could also enhance Raman scattering and gold nanoparticles could also quench fluorescence. Although graphene could also contribute to the Raman scattering by chemical enhancement[139,248,249], the effect is much smaller than that of electromagnetic enhancement from noble metals.[249,250] Similarly, the fluorescence quenching efficiency from plasmonic nanoparticles on dyes is much lower than graphene.[113] Therefore, we believe that the fluorescence

quenching property of the SiO_2/FGO/Au-Ag NP substrate mainly arises from the graphene oxide, possibly due to the resonance energy transfer[251] or charge transfer[252] between dye molecules and FGO.

With Alex fluor 488 as a model molecule, the SiO_2/FGO/Au-Ag NP as a Raman substrate could be used to monitor the characteristic Raman peaks of the molecule. In biosensors, most target molecules such as proteins and DNAs/RNAs are also Raman and fluorescence active. There are 20 natural amino acids in proteins, of which the phenylalanine, tryptophan, histidine, alanine, leucine and tyrosine are Raman active, epically the aromatic ones.[140-142] All the fives nucleotides consist of DNAs/RNAs, adenine, guanine, thymine, cytosine and uracil are Raman active.[143,144] Therefore, this platform has the potential to be developed into a label free hybrid sensing device, where the LSPR binding and Raman scattering could be monitored simultaneously.

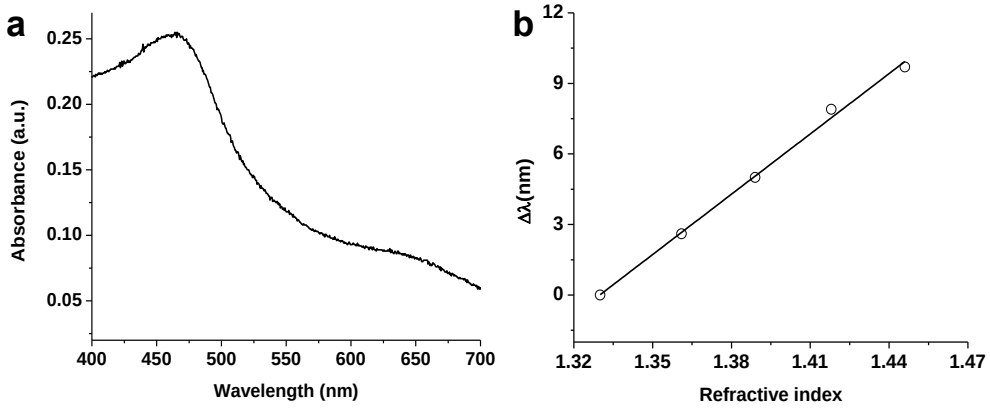

Figure 6.9 (a) Absorption spectrum of the FGO/Au-Ag NP Raman substrate on glass measured in air. (b) The peak shift of the FGO/Au-Ag NP Raman substrate measured in solvents with different refractive indices. The peak position is linearly fitted with slope of 85.5 nm/RIU and R^2 of 0.9958.

In addition to the Raman enhancement, the FGO/Au-Ag NP also works as a LSPR sensor. Figure 6.9(a) shows the absorption spectrum of the FGO/Au-Ag NP Raman substrate on glass measured in air and the peak maximum is ~467 nm. The LSPR peak of the FGO/Au-Ag NP measured at different refractive indices is summarized in Figure 6.9(b). The peak shift sensitivity with bulk refractive index is 85.5 nm/RIU.

6.2 Experimental section

Graphene oxide was synthesized using the modified Hummers method.[25, 45] Briefly, 0.3 g graphite was added into a mixture of 2.4 mL 98% H_2SO_4, 0.5 g $K_2S_2O_8$, and 0.5 g P_2O_5, the solution was maintained at 80 ℃ for 4.5 h. The resulting pre-oxidized product was cleaned by water and dried. After the pre-oxidized product was added into 12 mL 98% H_2SO_4, followed by slowly added 1.5 g $KMnO_4$ with the temperature maintained at below 20 ℃ in order to avoid overheating and explosion, the solution temperature was increased to 35 ℃ and maintained for 2 h. Then 25 mL H_2O was added. After 2 h, additional 70 mL H_2O was added to dilute the solution, and 2 mL 30% H_2O_2 was injected into the solution to completely react with the excess $KMnO_4$. A bright yellow solution was obtained. Then the resulting mixture was washed by HCl and H_2O and the graphite oxide powder was obtained by drying in air.

The as-prepared GO powder of 10 mg was then activated by dissolving in 50 mL of NaOH aqueous solution (3 M) and incubated for 30 min.[26] After the activation,

the GO was washed with DI water carefully until the pH of the supernatant drops to 8.

Gold silver alloy nanoparticles (NPs) were synthesized by co-reduction of the gold and silver salt simultaneously with trisodium citrate in aqueous solution.[31] In a typical experiment of synthesis of $Au_{0.7}Ag_{0.3}$ NPs, 875 μL of $HAuCl_4$ aqueous solution (10 mM) was introduced quickly into a flask containing 50 mL reflux DI water. After that 375 μL of $AgNO_3$ aqueous solution (10 mM) was introduced to the reaction solution. The reaction solution was kept for a stirring of ~30 min to allow for uniform mixture of the metal ions. Then, 2.5 mL of trisodium citrate aqueous solution (1 wt%) was quickly introduced to the reaction solution. The color of the reaction solution changed from colorless to orange gradually. The reaction solution was kept at refluxed for ~30 min to allow for complete reaction before cooling to room temperature in air. UV-Vis absorption spectrometer Lambda 35 from PerkinElmer was used to measure the absorption spectrum of $Au_{0.7}Ag_{0.3}$ NPs. Transmission electron microscope (TEM) Jeol 2100 was used to image the $Au_{0.7}Ag_{0.3}$ NPs.

Silicon wafers of 1×1 cm^2 size with a oxidation layer of 300 nm SiO_2 / glass slides of 1×0.5 cm^2 size were cleaned with RCA method. Briefly, the substrates were incubated in the mixture of DI water, 25% ammonia solution and 30% H_2O_2 (5:1:1 v:v:v) at boiling condition for 5 min. They are then rinsed carefully with DI water a few times. After the rinsing, they are dried by N_2. The surface are functionalized by incubation in 3-Aminopropyltriethoxysilane (APTES) aqueous solution (42.5 mM) for 5 min. [25, 46] The Au-Ag NPs were assembled by

immersing the APTES-modified substrates into the $Au_{0.7}Ag_{0.3}$ NP solution for 10 min, followed by rinsing with DI water. The GO was assembled by immersing the APTES-modified substrates into the activated graphene oxide (GO) solution for 10 min. The activated GO surface was then functionalized with ethylene diamine.

In a typical coupling reaction, the mixture of aqueous solution of N-Hydroxysuccinimide (NHS) 0.05 M and N,N'-dicyclohexylcarbodiimide (EDC) 0.2 M was applied on the activated GO surface and incubated for ~20 min. The substrate was then rinsed with DI water carefully. After that the surface is incubated with 100 µL ethylenediamine (NH_2-CH_2-CH_2-NH_2) 99.9% for ~30 min.[30] One of the amine group in the ethylene diamine reacted with the reactive succinimide ester on GO surface, while the other one is unreacted and convert the GO surface to amine-terminated. The substrate was then rinsed with DI water carefully. The GO surface was then incubated in $Au_{0.7}Ag_{0.3}$ NP solution for 10 min to allow adsorption of NPs. The substrates were then rinsed with DI water and dried with N_2.

500 µL of Alexa fluor@488 carboxylic acid, succinimidyl ester in sodium bicarbonate buffer solution 1 µM was applied onto the amine terminated substrates. After an incubation of ~10 min, the substrates were rinsed with DI water carefully and dried with N_2.

Field emission scanning electron microscope (FESEM) Jeol 7600F was used to image the substrates and elemental analysis. In a typical FESEM experiment, 5 kV was used for the imaging and 20 kV was used for EDX analysis. Raman

scattering of Alexa fluor 488 molecules were collected with the confocal Raman spectrometer WITec alpha 300. The laser of 488 nm LASOS Argon-Ion Laser Power Supplies LGN 7812 was used to excite the Raman scattering and fluorescence. A low laser power of < 1 mW and a short integration time (0.05 s) were used to minimize the decomposition of molecules. The Raman peak of silicon at ~520 cm^{-1} was used as the reference.

6.3 Conclusions

To sumarize, a novel Raman substrate SiO_2/FGO/Au-Ag NP has been fabricated by immoblizing $Au_{0.7}Ag_{0.3}$ NPs onto the GO film coated on SiO_2 through electrostatic attraction. The Raman substrate integrates the excellent fluorescence quenching property from GO with the Raman enhancement property from the $Au_{0.7}Ag_{0.3}$ NPs. With the highly fluorescent model molecule Alexa fluor 488, the Raman substrate demonstrates an improvement in the signal-to-background ratio of 6 orders of magnitude. The novel Raman substrate SiO_2/FGO/Au-Ag NP opens up an avenue for label free Raman characterization of ordinary biomolecules, such as proteins and DNAs/RNAs. In addition the substrate also demonstrate a LSPR peak shift with bulk refractive index changes, where the refractive index sensitivity is 85.5 nm/RIU. With this novel substrate, a hybrid sensing platform based on Raman scattering and LSPR response can be developed.

Chapter 7: Collaborative projects on plasmonics and biosensors

In this chapter I will briefly introduce the relevant projects done in collaboration will other researchers. These works are already published or ready for submission. The works could be further categorized into colorimetric sensors, plasmonic sensing platforms and electrical sensors.

7.1 Colorimetric Sensor 1: Bio-functionalized gold nanoparticles for colorimetric sensing of botulinum neurotoxin A light chain

Botulinum neurotoxin is considered to be one of the most toxic substances and recently it was found to be present in milk powders. Botulinum neurotoxin is also a potential bio-weapon for terrorists. Therefore, an accurate, convenient and rapid assay for botulinum neurotoxins is of high significance to address the safety concerns. Herein, a gold nanoparticle-based colorimetric assay for botulinum neurotoxin serotype A light chain (BoLcA) was developed where novel biotinylated peptide substrates are utilized. In the colorimetric assay, the biotinylated peptides serve as linker molecules, which bring individual gold nanoparticles into aggregation. A distinct color transition from red to blue is clear to seen by naked eyes. The cleavage of the peptides by BoLcA prevents nanoparticle aggregation and the color remain unchanged. Two different assay strategies are developed, and the limit of detection is ranging from 5 nM to 0.1 nM of BoLcA. The overall assay time can be finished in 4 hours.

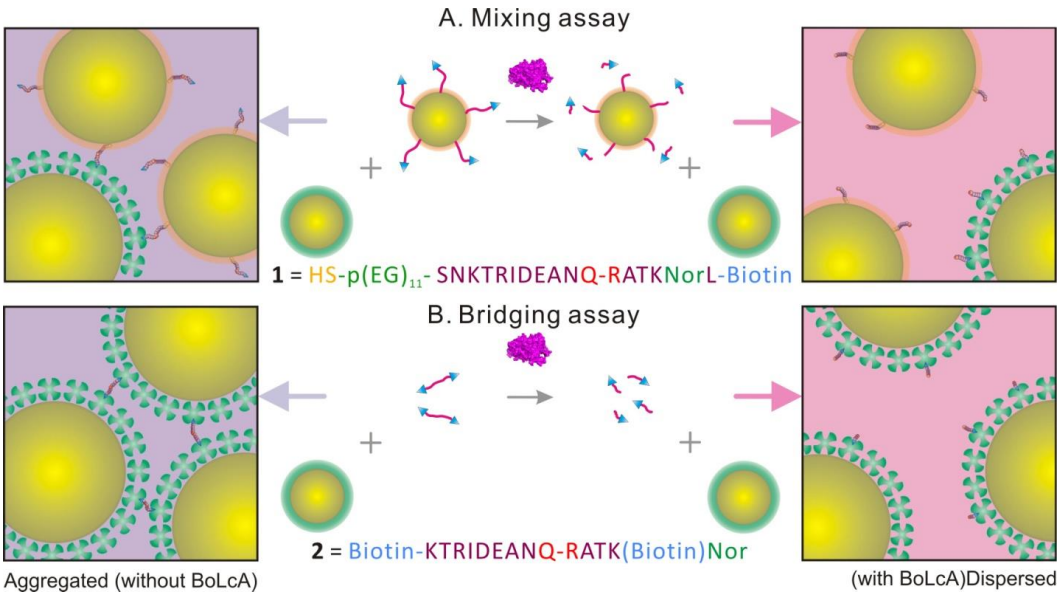

Figure 7.1 Schematic illustration of the mixing (A) and bridging (B) assays for detection of BoLcA using two peptide-designs (1 and 2) and bio-functionalized AuNPs. Reprinted with permission from ref.[25] Copyright © 2014, American Chemical Society.

The two detection strategies are illustrated in Figure 7.1. Bridging assay shows a higher sensitivity. The calibration curve and color image of bridging assay is shown in Figure 7.2. The concentration dependent peak-shift Δλ and color changes are shown in Figure 7.2(a) and 7.2(b), respectively. The LOD was estimated to be 0.1 nM (5 ng/ml of BoLcA) using 3 time of standard deviation of baseline. Interestingly, the peak shift induced a significant color difference which enable the naked eye detection, see Figure 7.2(b).

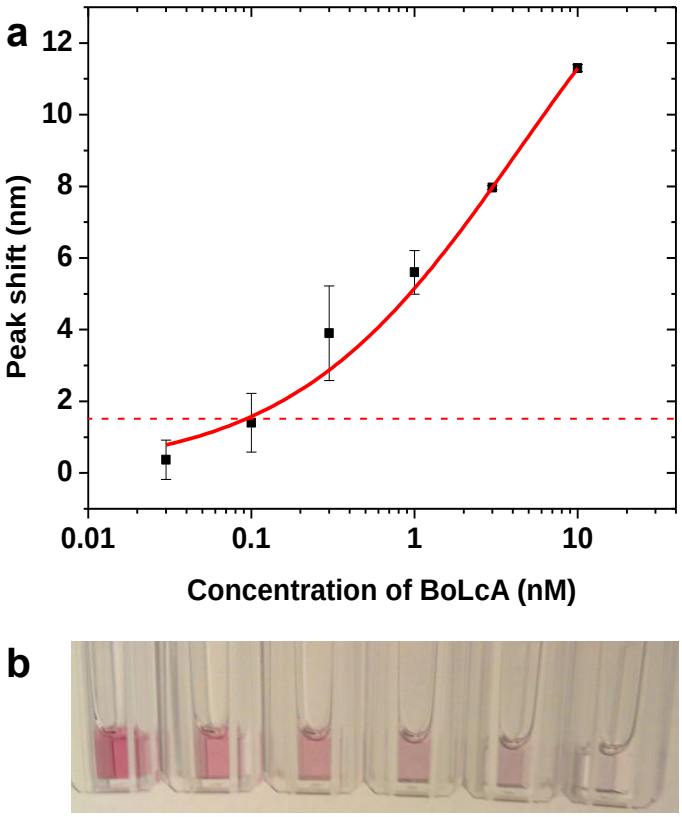

Figure 7.2 (a) Calibration curve for the BoLcA concentrations by the bridging assay. (Error bars are the standard error of n measurements, n ≥ 3) (b) Photograph of the navi-AuNP solutions with 10, 3, 1, 0.3, 0.1 and 0 nM of BoLcA from left to right. Adapted with permission from ref.[25] Copyright © 2014, American Chemical Society.

This work was published on *Analytical Chemistry*. I provided the help in the gold nanoparticle synthesis and functionalization, discussion of result and the writing of paper.

Liu, X. H. ; Wang, Y.; Chen, P.; Wang, Y.; Zhang, J.; Aili, D.; Liedberg, B., Bio-functionalized Gold Nanoparticles for Colorimetric Sensing of Botulinum Neurotoxin A Light Chain. *Anal. Chem.* **2014**, 86 (5), 2345–2352

7.2 Colorimetric Sensor 2: Gold aggredots for colorimetric G6PD deficiency sensing

Human cells can contain up to 10 mM of reduced glutathione which serves as an antioxidant in protecting cells from oxidative stress [201]. Detection of reduced glutathione is important for the diagnosis of glucose-6-phosphate dehydrogenase deficiency, a disease affecting over 400 million people worldwide [202]. Disease carriers are extremely sensitive to oxidative substances such as quinine derivatives that are used to treat malaria, of which when exposure to, can lead to lethal hemolytic anaemia. Detecting glutathione in the reduced state can be challenging due to the similarity in immuno-reactivity between reduced and oxidized states. To achieve specificity in our assay, we utilized the dimeric glutathione-S-transferase (GST) protein of *schistosoma japonicum* which is extremely specific to reduced glutathione. [203] The assay format is firstly the gold nanoparticles are aggregated into macroscopic dots by the GST proteins. Addition of GSH will disperse the dots into individual nanoparticles. The dispersion process brings the suspension with the dots from transparent to red. Figure 7.3(a) shows the FESEM image of the aggregated AuNPs in a dot and dispersed AuNPs. Figure 7.3(b) shows the color change of aggregated dots with addition of 10 mM GSH and 10 mM BME (control).

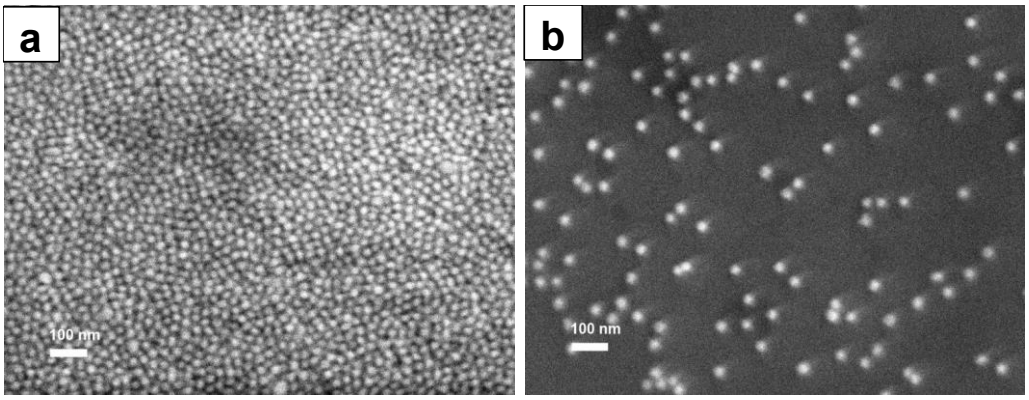

Figure 7.3 (a) FESEM image of AuNPs in an aggregated dot. (b) FESEM images of AuNPs dispersed from (a) with addition of 10 mM GSH.

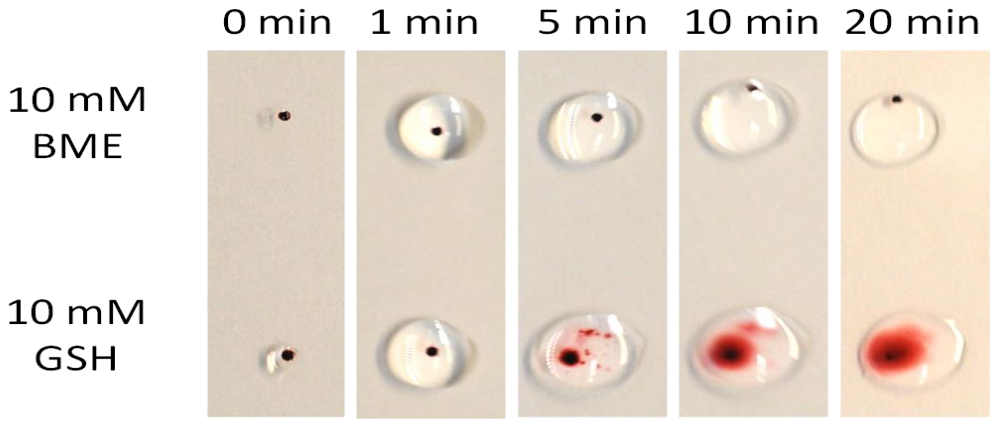

Figure 7.4 Photos of the aggregated AuNP dots in different stage of dispersion with addition of GSH and BME (control experiment).

The dispersion of AuNPs by GSH is very quick and the color change is very obvious for human eyes, Figure 7.4.

This work is done by Wei Sheng Chia, Peng Chen, Li Hoi Yeung, Peter Prieser and Bo Liedberg. The manuscript will be submitted soon. My contribution on this manuscript is modeling and calculation of the disperse of gold nanoparticles from

a dots, characterization of the AuNPs in aggregated and dispersed form with field emission microscope, help in the writing of papers.

7.3 Colorimetric Sensor 3: Peptide-assembled graphene oxide as fluorescent turn-on sensor for specific and sensitive lipopolysaccharide detection

Lipopolysaccharide (LPS), or endotoxin, is a major component in the outer cell membrane of Gram-negative bacteria. It is a glycolipid comprising a variable polysaccharide domain attached to a conserved glucosamine-based phospholipid called lipid A.[177] It is a very powerful and toxic inflammatory stimulator which induces host monocytes and macrophages to secrete a wide range of inflammatory cytokines including interleukins-1, tumor necrosis factor-α, and interleukin-8.[177-179] Excessive secretion of these cytokines may contribute to organ failure or result in sepsis or septic shock, a significant medical problem effecting about 700,000 patients and causing 250,000 casualties annually in the United States.[253,254] In fact, septic shock is one of the top causes of death in hospital patients (high mortality rate of 30-50%) in Europe.[178]

The development of specific and sensitive LPS biosensor is of highly importance. However, the currently used enzymatic Limulus amebocyte lysate (LAL) assay is highly susceptible to changes in temperature and pH,[255] various interference factors (either inhibiting or enhancing) in the samples,[256-259] and requires cumbersome sample preparation, storage and controlled experimental condition.[255,260] Herein we developed a simple colorimetric biosensor for LPS utilizing graphene oxide and synthetic peptide. The principle of this biosensor is

shown in Figure 7.5. Briefly, the LPS binding release the dye from graphene oxide surface and turn the fluorescence on.

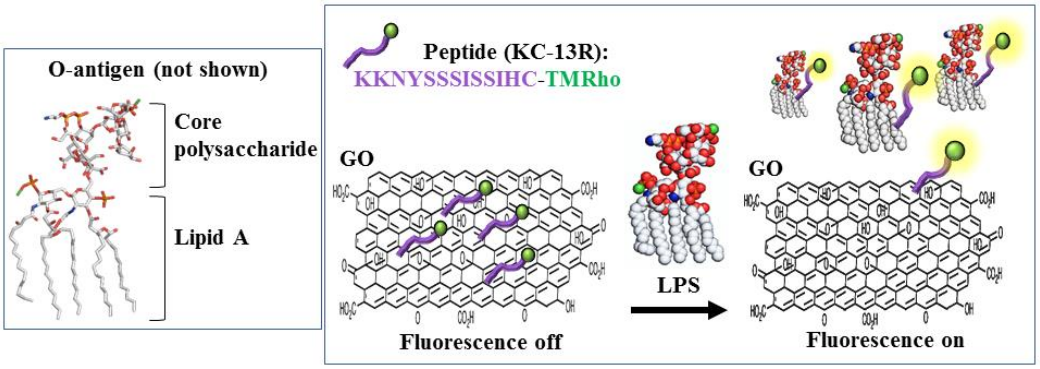

Figure 7.5 Structure of LPS and (B) Sensing principle of the peptide-GO assembled LPS sensor.

Figure 7.6(a) shows the fluorescence spectra of the peptide functionalized GO with addition of different concentrations of LPS. A linear relationship (R^2=0.99043) was observed with the LPS concentration ranging from 2 to 20 nM, Figure 7.6(b). The detection limit of the present approach was found to be 130 pM.

This work was done by Seng Koon Lim, Peng Chen, Fook Loy Lee, Shabbir Moochhala and Bo Liedberg. A provisional US patent has recently been filed. My contribution to the work is help in the design the project, experiments work related to graphene oxide synthesis, modification, characterization, and help in the writing of manuscript.

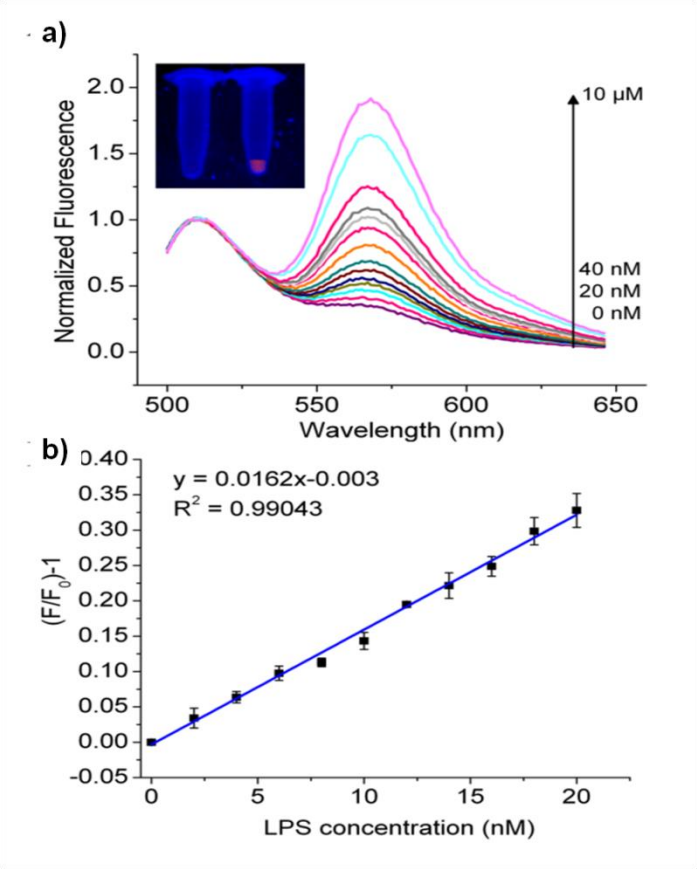

Figure 7.6 Detection of LPS in buffer containing LPS standards (a) Fluorescence titration spectra of peptide-GO assembled upon addition of 0 to 10 μM of LPS. The inset shows the corresponding fluorescence change in absence (left) and in the presence of 8 μM LPS (right). (b) Calibration curve of fluorescence intensity change [(F- F0)-1] vs the concentration of LPS (0-20 nM). F0 and F are fluorescence intensities at 572 nm in the absence and the presence of LPS, respectively.

7.4 Platform 1: Optimizing the refractive index sensitivity of plasmonically coupled gold nanoparticles

The local refractive index sensitivity of 3D AuNP clusters was investigated both theoretically and experimentally. The optical coupling between Au-NPs of various sizes was tuned by the inter-particle separation using a layer-by-layer assembly of polyelectrolytes. The bulk refractive index (RI) sensitivity for the

plasmonic coupling modes was investigated and compared to the RI sensitivity of dispersed Au-NPs. Results from both experimental measurements and theoretical calculations clearly demonstrates that the RI sensitivity can be significantly enhanced in plasmonically coupled Au-NPs. The proposed approach is simple and scalable and improves the rather modest RI sensitivity of spherical gold nanoparticles with a factor of 3.

Extinction spectra of various AuNP clusters in different solvents are shown in Figure 7.7(a)-(f). The refractive index sensitivity is summarized in Figure 7.7(g).

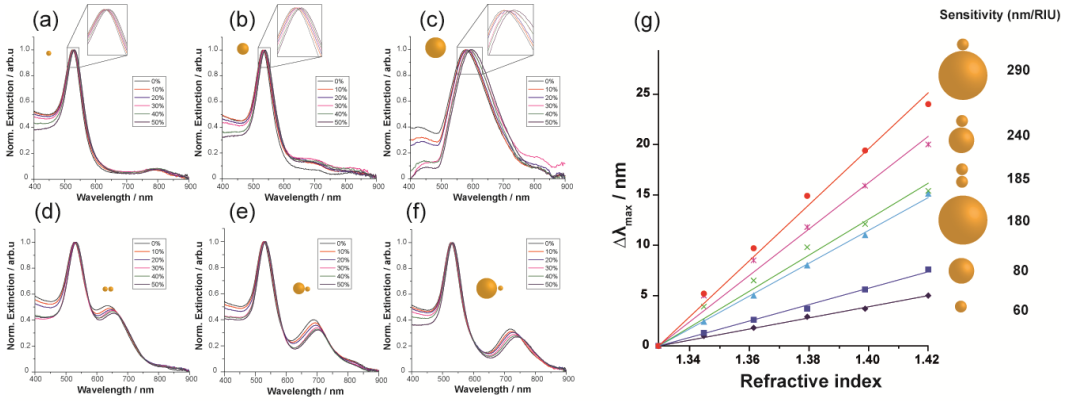

Figure 7.7 Extinction spectra obtained in water/sucrose mixtures (0-50%) for individual gold nanoparticles; a) 25 nm, b) 50 nm, c) 100 nm and for particle coupling between; d) 25 nm + 25 nm, e) 50 nm + 25 nm and f) 100 nm + 25 nm. G) LSPR maximum in a-c and plasmon coupling LSPR maximum in d-f plotted as a function of refractive index. The sensitivities was obtained through linear fitting. Reprinted with permission from ref.[200] Copyright © 2013, Springer Science+Business Media New York.

This work was published on *Plasmonics*.

Martinsson, E.; Sepulveda, B.; Chen, P.; Elfwing, A.; Liedberg, B.; Aili, D., Optimizing the Refractive Index Sensitivity of Plasmonically Coupled Gold Nanoparticles. *Plasmonics* **2014**, 9, (4) 773-780.

My contribution to this work is help in the project initiation, help in the result analysis and help in the writing of manuscript.

7.5 Platform 2: High-density metallic nanogaps fabricated on solid substrates used for surface enhanced Raman scattering

Surface enhanced Raman scattering (SERS), as a surface sensitive technique has been widely explored in fundamental studies and applications.[131] Various noble metal nanostructures, e.g. nanorings, nanocrescents, nanostars, nanoflowers, triangles, nanogaps, dimers, nanorods, nanorices and nanoshells have been used as SERS substrates.[130-136] However, for these substrates, a dramatic Raman enhancement can only be obtained at specific locations (Raman hot spots), which limit its applications in real applications. Therefore, it is of importance to enhance the overall Raman signal on the substrate by designing a metallic nanostructure with high-density Raman hot spots. For metallic nanogaps, the enhancement capability is strongly dependent on the gap size. Generally, smaller size shows better enhancement performance due to the strong coupling of surface plasmon. We report a simple, convenient and tunable method to fabricate high-density plasmonic nanogaps on Si wafers using repeated electroless deposition of Ag NPs or Au NPs. Repeated deposition contribute to enhancement in two different ways. Firstly, as more particles are added to the surface, more gaps are formed, as a result, the density of hot spots increase. Secondly, as more gaps are formed on a

fixed area, the size of gaps becomes smaller. This method also enables a control over the gap size and type of materials. The fabrication process of the high-density plasmonic nanogaps is illustrated in Figure 7.8.

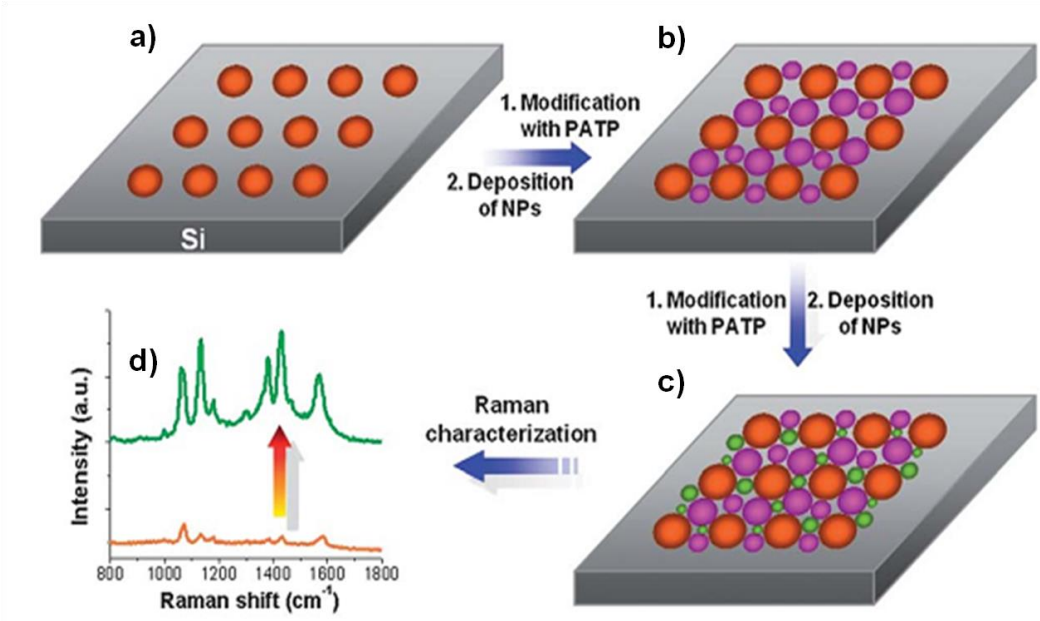

Figure 7.8 Schematic illustration of the fabrication process of the high-density nanogaps of Au and Ag on Si wafer. (a) First-round Au or Ag NPs were deposited on Si wafer. (b) Second-round deposition of Ag or Ag NPs on the exposed Si region in (a). (c) Third-round deposition of Au or Ag NPs on the exposed Si region in (b). (d) Raman scattering from PATP on the substrate. Reproduced from ref.[191] with permission from The Royal Society of Chemistry.

The high-density nanogaps work very well for various molecules. Figure 7.9 shows the Raman spectrum of some commonly seen Raman tag molecules.

This work was published on *Nanoscale*.

Lu, G.; Li, H.; Wu, S.; Chen, P.; Zhang, H., High-density metallic nanogaps fabricated on solid substrates used for surface enhanced Raman scattering. Nanoscale 2012, 4 (3), 860-863.

My contribution to this work is to help on the analysis of Raman result and help in the writing of paper.

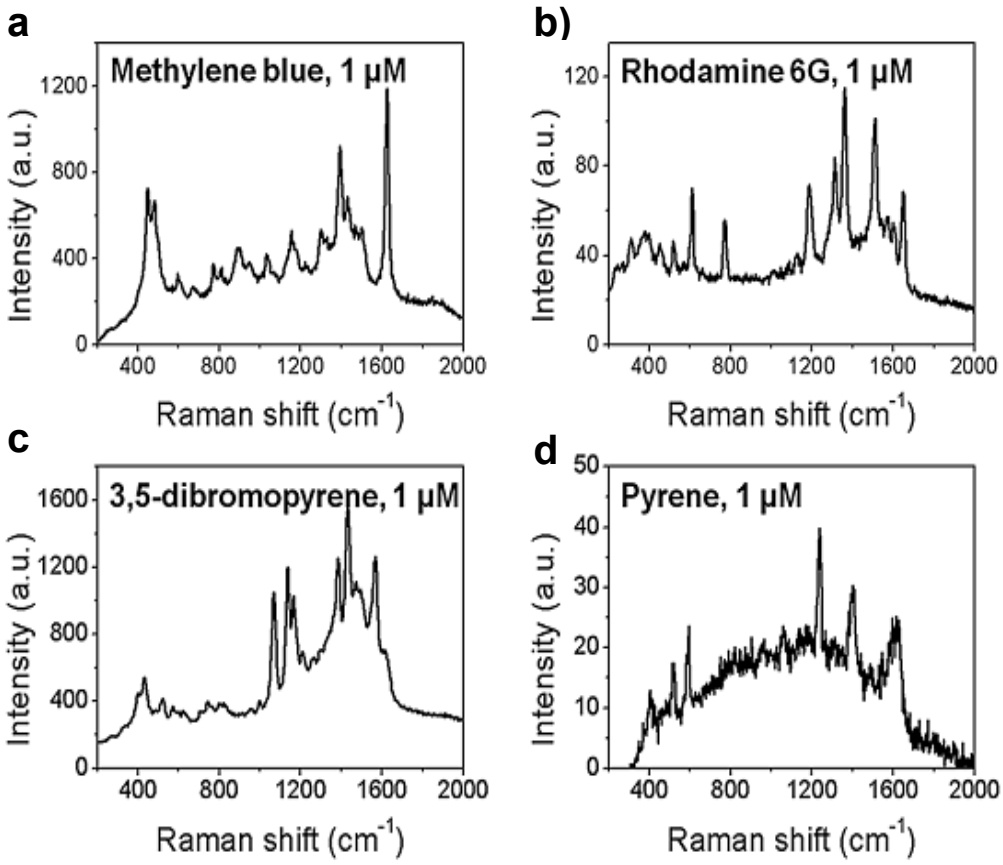

Figure 7.9 Raman spectra of (a) methylene blue, (b) rhodamine 6G, (c) 3,5-dibromopyrene and (d) pyrene on the SERS substrate. Adapted from ref.[191] with permission from The Royal Society of Chemistry.

7.6 Electrical sensor 1: Label-free, electrochemical detection of methicillin-resistant staphylococcus aureus DNA with reduced graphene oxide-modified electrodes

The methicillin-resistant Staphylococcus aureus bacterium (MRSA) DNA is a common pathogen that causes difficult-to-treat diseases in humans, such as pneumonia, bacterial endocarditis, and hospital- and community-acquired

bacteremic infections.[261,262] The MRSA bacterium has developed the resistance to beta-lactam and vancomycin antibiotics through the natural selection process.[263,264] Therefore, a simple and sensitive method to detect MRSA is of significant importance for the control of diseases. Herein, a characteristic DNA of MRSA is detected using electrochemical impedance spectroscopy. Reduced graphene oxide (rGO) is used as electrode. The combination of the novel 2D materials and sensitive technique enable a limit of detection of 10^{-14} M. The fabrication of rGO electrode and detection method is illustrated in Figure 7.10.

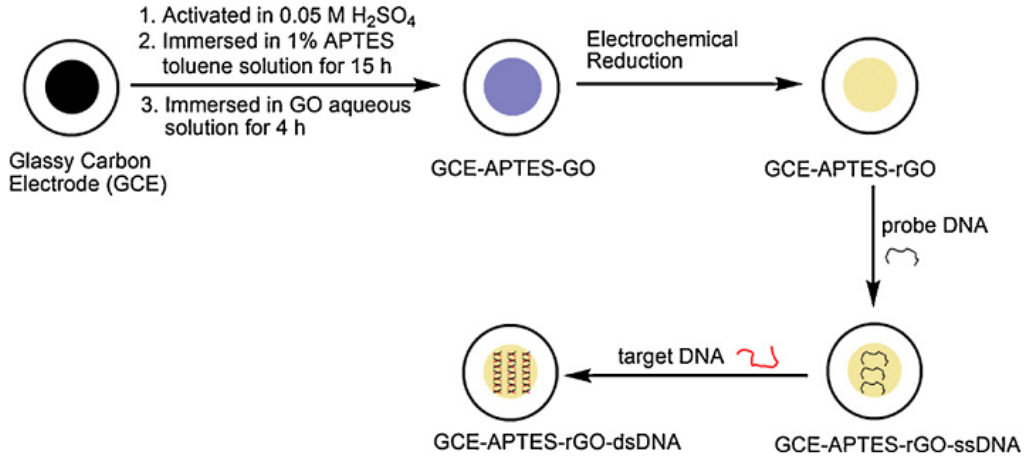

Figure 7.10 Schematic illustration of the surface functionalization process of the glassy carbon electrode for DNA detection. Reprinted with permission from ref. [160] Copyright © 2011, Elsevier.

The response of impedance to different concentrations of target DNA is shown in Figure 7.11A. Higher concentration of target DNA produces larger impedance (the radius of the semicircle). Figure 7.11B shows the calibration curve for the target DNA as well as two non-complementary DNAs. The concentration of

target DNA can be detected at 10^{-14} M. The specificity of this sensor is also very good that non-complementary DNAs give very small response.

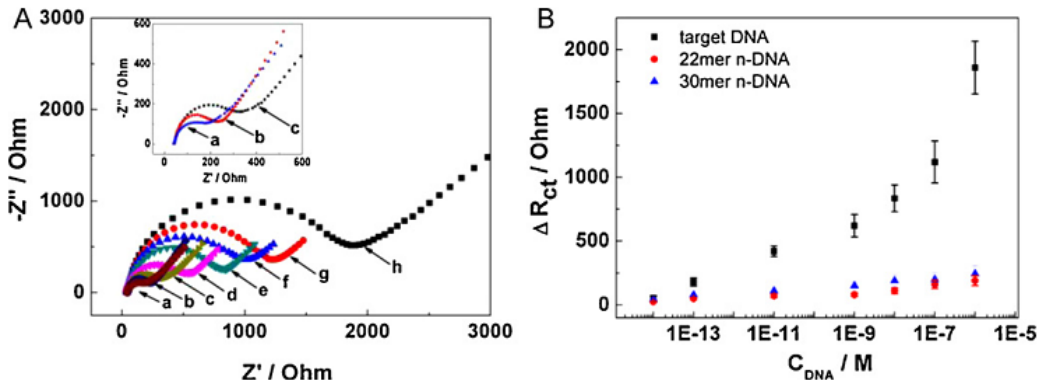

Figure 7.11 (A) Nyquist plots of GCE-APTES-rGO-ssDNA hybridized with target DNA at different concentrations: (a) 0, (b) 10^{-14}, (c) 10^{-13}, (d) 10^{-11}, (e) 10^{-9}, (f) 10^{-8}, (g) 10^{-7} and (h) 10^{-6} M. Inset: magnification of curves a, b and c. (B) Calibration curve and control experiment with 20-mer and 30-mer non-complementary DNAs. Adapted with permission from ref. [160] Copyright © 2011, Elsevier.

This work was published on *Biosensors and Bioelectronics*.

Wang, Z.; Zhang, J.; Chen, P.; Zhou, X.; Yang, Y.; Wu, S.; Niu, L.; Han, Y.; Wang, L.; Chen, P.; Boey, F.; Zhang, Q.; Liedberg, B.; Zhang, H., Label-free, electrochemical detection of methicillin-resistant staphylococcus aureus DNA with reduced graphene oxide-modified electrodes. Biosens. Bioelectron. 2011, 26 (9), 3881-3886.

My contribution to this work is doing the Raman experiment and help on the writing of paper.

7.7 Electrical sensor 2: Real-time DNA detection using Pt nanoparticle-decorated reduced graphene oxide field-effect transistors

Graphene, a novel 2D carbon material has been widely explored for applications including transistors (FETs), memories, sensors and photovoltaics. Due to its unique electronic and optical properties as well as biocompatibility, graphene attracted many research interests in biosensors. Most biosensors utilize the fluorescence or electrochemical transducing mechanism, which requires some labeling tags. Herein, an electrical platform based on FET device enables a label free and real time monitoring of the molecular binding. Graphene, although very sensitive to molecular binding, the surface is easily saturated, which limit its detection in high concentration range. To enhance the dynamic range, Pt nanoparticles are immobilized onto the graphene surface to introduce more surface areas. With DNA, the FET based electrical sensor could detect binding in the range of 2.4 nM to 5 mM.

The fabrication process of the FET device is illustrated in Figure 7.12. Briefly, GO sheets are coated on SiO_2 surface by Langmuir-Blodgett method. After adsorbed onto the SiO_2 substrate, it was reduced to rGO by thermal annealing in hydrogen atmosphere. Platinum nanoparticles were then deposited on the rGO surface through photochemical reduction of Pt ions.

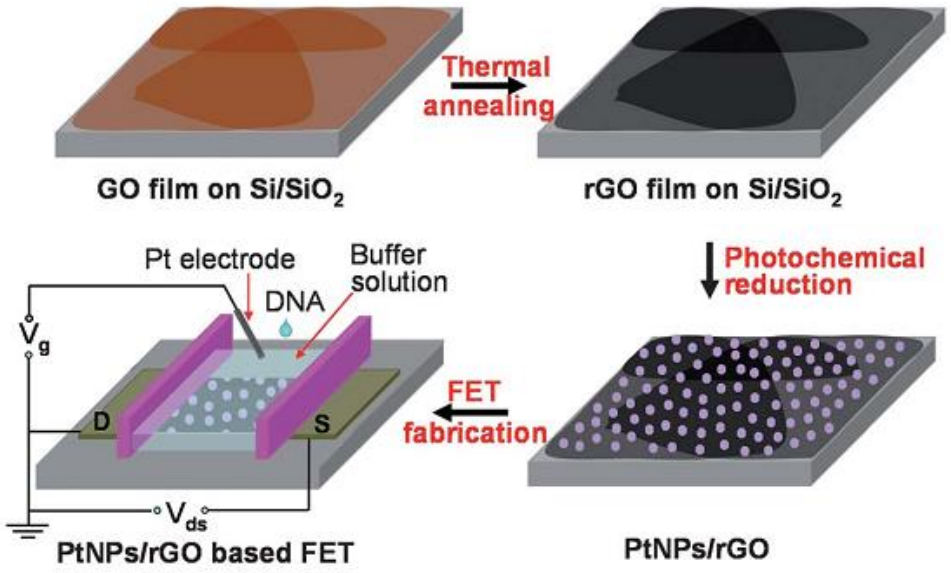

Figure 7.12 illustration of fabrication process of a solution-gated FET sensing device based on PtNPs/rGO films. Reproduced from ref.[265] with permission from The Royal Society of Chemistry.

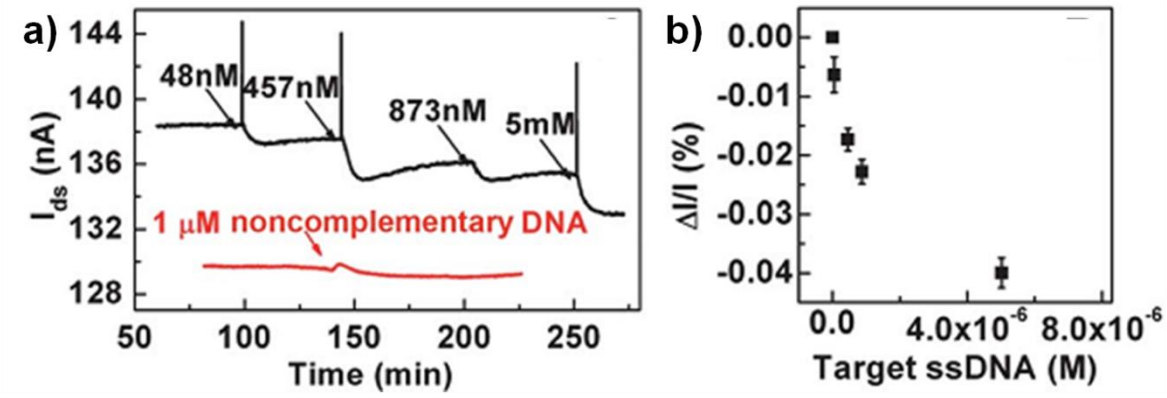

Figure 7.13 (a) Real-time response of the hybridization of target DNA to probe DNA in PBS buffer (black line) and a control experiment result with addition of non-complementary DNA (red line). (b) Plot of conductance change at different concentrations of target DNA. Reproduced from ref.[265] with permission from The Royal Society of Chemistry.

The source drain current of the FET device depends on the amount of DNA binding. Figure 7.13(a) shows the real time response of current with addition of

different concentrations of DNA molecules. The current decreases with the binding of DNA. The percentage of current change is plotted with concentrations in Figure 7.13(b).

This work was published on *Nanoscale*.

Yin, Z.; He, Q.; Huang, X.; Zhang, J.; Wu, S.; Chen, P.; Lu, G.; Chen, P.; Zhang, Q.; Yan, Q.; Zhang, H., Real-time DNA detection using Pt nanoparticle-decorated reduced graphene oxide field-effect transistors. *Nanoscale* **2012,** *4* (1), 293-297.

My contribution to this work is discussion of the result and help on the writing of paper.

Chapter 8: Conclusion and Future Perspectives

Plasmonic nanoparticles offer many opportunities to design biosensors with better performance due to its unique optical properties. In this thesis, I have demonstrated three different designs based plasmonic nanoparticles, namely refractive index sensing, colorimetric sensing and Raman scattering based hybrid sensing platform. The refractive index sensing is a universal technique that can monitor the real time binding kinetics, affinity etc. Colorimetric sensing enables an easy assay without equipment, which is very useful for field testing. The Raman scattering based hybrid sensing integrates a spectroscopic characterization into a sensor. Therefore, it provides more information and more reliable.

Refractive index sensing by LSPR sensor monitors the changes in refractive index upon molecular binding. It could monitor the concentration and binding kinetics of a particular target of interest. The sensitivity of the LSPR sensor to refractive index (RIU) is very small for the spherical nanoparticles compared to that of planar SPR sensor, which limit its applications in detecting molecules in low concentrations. Two approaches are explored to solve this problem. Firstly, a new strategy to evaluate the LSPR spectrum by the curvature was proposed. The refractive index sensitivity of curvature was investigated theoretically and experimentally. Compared to traditional peak shift and extinction, the curvature method enables a lower detection limit and high reliability because a larger portion of the LSPR spectrum is used in the analysis. Secondly, a new method to improve the refractive index sensitivity by optimizing the configurations of coupling nanoparticles was investigated. In a 2D plane, the linearly packed

coupling nanostructures are the most sensitive device followed with closely packed ones.

Colorimetric sensors based on gold nanoparticles attract increasing interest because of its simplicity to use and equipment-less detection. The principle of the colorimetric sensor is that the color of AuNPs can be tuned by the inter-particle distance. By controlled aggregation or dispersion, colorimetric sensors for three different target molecules, MMP-7, Botulinum and reduced glutathione were designed. A colorimetric sensor of the cancer marker MMP-7 was designed based on peptide functionalized AuNPs. Presence of MMP-7 leads to aggregation of AuNPs and bluish transition, which can be detected by the naked eye. Similarly, the botulinum sensor is designed based on peptide functionalized AuNPs, where the presence of botulinum prevents the aggregation of AuNPs. The reduced glutathione sensor was designed on the reverse principle by dispersing the pre-aggregated AuNPs. The reduced glutathione could disperse the aggregated AuNPs and the red color recovers. This type of colorimetric sensing system can be extended to detect other targets of interest.

In addition to the sensitivity, we also focus on improving the reliability of the sensor (the ability of distinguishing response from other stuff other than target). To achieve this, we propose to build hybrid sensor that have two or more independent transducing mechanisms. A prototype hybrid sensing platform combining the Raman scattering and LSPR refractive index sensing is built. A novel substrate based on $Au_{0.7}Ag_{0.3}$ and graphene oxide was fabricated as the

sensing chip. This substrate shows excellent Raman signal to fluorescence background ratio. It also demonstrates good bulk refractive index sensitivity.

In future, research works could be explored in the following directions, small molecule detection and drug screening, colorimetric sensor for clinical test and hybrid sensors development etc.

Small molecules play significant roles in biological process of human body. Some of the small molecules include ATP, glutathione, Ca^{2+}, phenylalanine and glucose etc. These molecules are very difficult to be detected using the commercial SPR sensors. A simple and quick monitoring these molecules could be done with the LSPR sensor by monitoring the response of curvature upon molecular binding. Similarly, this platform could be used for drug screening, especially for those with small molecular weight.

We have developed many types of colorimetric sensors for different target molecules in the buffer solution. For real application however, it must work in real matrix, e.g. blood, serum and milk etc. Matrilysin or MMP-7 is found to be related to human colorectal carcinogenesis. The levels and activity of MMP-7 in patients of different stages can be analyzed using the colorimetric sensor. This work will be done in collaboration with hospitals and a research group at Leuven University, the Netherlands.

Hybrid sensing platform based on Raman scattering and LSPR will be developed for detecting biomolecules in the real matrix, e.g. blood and serum. Most often, LSPR sensor alone could not work very well due to the unspecific binding from

the Human serum albumin as well as other molecules present. With Raman scattering, the fingerprint of the binding molecules could reveal exactly what is the molecule.

Curvature of LSPR peak is a very useful technique and now used widely for study molecular binding and aggregations as well. However, in the time of thesis preparation, the curvature method is a new technique and before which the other projects listed in the thesis have been finished and that is the reason that the useful technique is not even used by me in my thesis.

Chapter 9 Publications Chen Peng

9.1 Journals

1. Chen, P.; Selegård, R.; Aili, D.; Liedberg, B., Peptide Functionalized Gold Nanoparticles for Colorimetric Detection of Matrilysin (MMP-7) Activity. *Nanoscale* **2013,** *5*, 8973-8976.
2. Chen, P.; Yin, Z.; Huang, X.; Wu, S.; Liedberg, B.; Zhang, H., Assembly of Graphene Oxide and $Au_{0.7}Ag_{0.3}$ Alloy Nanoparticles on SiO_2: A New Raman Substrate with Ultrahigh Signal-to-Background Ratio. *J. Phys. Chem. C* **2011,** *115* (49), 24080-24084.
3. Liu, X. H.; Wang, Y.; Chen, P.; Wang, Y.; Zhang, J.; Aili, D.; Liedberg, B., Bio-functionalized Gold Nanoparticles for Colorimetric Sensing of Botulinum Neurotoxin A Light Chain. *Anal. Chem.* **2014**, *86* (5), 2345-2352.
4. Lu, G.; Li, H.; Wu, S.; Chen, P.; Zhang, H., High-density metallic nanogaps fabricated on solid substrates used for surface enhanced Raman scattering. *Nanoscale* **2012,** *4* (3), 860-863.
5. Martinsson, E.; Sepulveda, B.; Chen, P.; Elfwing, A.; Liedberg, B.; Aili, D., Optimizing the Refractive Index Sensitivity of Plasmonically Coupled Gold Nanoparticles. *Plasmonics* **2014**, 9 (4), 773-780.
6. Wang, Z.; Wu, S.; Zhang, J.; Chen, P.; Yang, G.; Zhou, X.; Zhang, Q.; Yan, Q.; Zhang, H., Comparative studies on single-layer reduced graphene oxide films obtained by electrochemical reduction and hydrazine vapor reduction. *Nanoscale Res. Lett.* **2012,** *7* (1), 161.

7. Wang, Z.; Zhang, J.; Chen, P.; Zhou, X.; Yang, Y.; Wu, S.; Niu, L.; Han, Y.; Wang, L.; Chen, P.; Boey, F.; Zhang, Q.; Liedberg, B.; Zhang, H., Label-free, electrochemical detection of methicillin-resistant staphylococcus aureus DNA with reduced graphene oxide-modified electrodes. *Biosens. Bioelectron.* **2011,** *26* (9), 3881-3886.
8. Yin, Z.; He, Q.; Huang, X.; Zhang, J.; Wu, S.; Chen, P.; Lu, G.; Chen, P.; Zhang, Q.; Yan, Q.; Zhang, H., Real-time DNA detection using Pt nanoparticle-decorated reduced graphene oxide field-effect transistors. *Nanoscale* **2012,** *4* (1), 293-297.
9. Yin, Z.; Zeng, Z.; Liu, J.; He, Q.; Chen, P.; Zhang, H., Memory Devices Using a Mixture of MoS_2 and Graphene Oxide as the Active Layer. *Small* **2013,** *9* (5), 727-731.
10. Chen, P.; Liedberg, B., Curvature of Localized Surface Plasmon Resonance Peak. *Anal. Chem.* **2014,** *86* (15), 7399-7405.
11. Chen, H.; Lim, S. K.; Chen, P.; Huang, J.; Wang, Y.; Palaniappan, A.; Platt, M.; Liedberg, B.; Tok, A. I. Y., Reporter-encapsulated liposomes on graphene field effect transistors for signal enhanced detection of physiological enzymes. *Phys. Chem. Chem. Phys.* **2015,** *17* (5), 3451-3456.
12. Chia, W. S.; Chen, P.; Li, H. Y.; Prieser, P.; Liedberg, B., Gold aggredots for colorimetric G6PD deficiency sensing. *Submitted*.
13. Lim, S. K.; Chen, P.; Lee, F. L.; Moochhala, S.; Liedberg, B., Peptide-assembled graphene oxide as fluorescent turn-on sensor for specific and sensitive lipopolysaccharide detection. *Under Review*.

14. Lim, S. K.; Chen, P.; Liedberg, B., Method of endotoxin/lipopolysaccharide detection. *Provisional US Patent filed*, TECH/305/13.
15. Chen, P.; Liu, X.; Nhung, T. T.; Liedberg, B., Enzyme free colorimetric detection of hydrogen peroxide through dimerization induced aggregation of gold nanoparticles (AuNPs). *In preparation*.
16. Chen, P.; Nhung, T. T.; Liu, X.; Daniel, A.; Liedberg, B., Study on the aggregation process of gold nanoparticles by the curvature of localized surface plasmon resonance (LSPR) peak. *In preparation*.
17. Chen, P.; Nhung, T. T.; Liedberg, B., Inflection point of the localized surface plasmon resonance (LSPR) peak: a general method to improve refractive index sensitivity, *In preparation*.

9.2 Conferences and Workshops

1. Chen, P.; Zhou, X.; Yin, Z.; Huang, X; Li, H.; Boey, F.; Zhang, H. A Novel Versatile Method for Synthesis of Reduced Graphene Oxide/Nanoparticle Composite, Asia-Oceania Top Univ. League on Engineering International Conference on Engineering, 2010, Bandung, Indonesia. (Oral presentation)

2. Chen, P.; Aili, D.; Zeng, Z.; Zhang, H.; Liedberg, B.; Peptide Functionalized Gold Nanoparticles for Colorimetric Detection of Protease Activity, ICMAT, 2011, Singapore. (Poster)

3. Chen, P.; Aili, D.; Liedberg, B.; Peptide functionalized gold nanoparticles for colorimetric detection of matrilysin (MMP-7) activity, Biosensors 2012, 2012, Cancun, Mexico. (Oral presentation)

4. Chen, P.; Liu, X.H.; Wang, Y.; Aili, D.; Liedberg, B; Aggregation of gold nanoparticles, 30 Years of Surface Plasmon Resonance (SPR) in Biosensing, 2013, Singapore (Best Poster)

5. Chen, P.; Liedberg, B; On the Curvature of Localized Surface Plasmon Resonance Peak, 30 Years of Surface Plasmon Resonance (SPR) in Biosensing, 2013, Singapore (Poster)

6. Liedberg, B.; Chen, P.; Liu, X.H.; Wang, Y.; Aili, D., Soft matter Nanoarchitectures and Nanoparticles for Biosensing and Diagnostics, International Conference on Small Science 2014, Hong Kong. (Oral presentation)

7. Chen, P.; Liedberg, B; Colorimetric detection of MMP-7 by peptide functionalized gold nanoparticles, Polyelectrolyte workshop, 2015, Singapore (Poster)

References

(1) Raschke, G.; Kowarik, S.; Franzl, T.; Sönnichsen, C.; Klar, T. A.; Feldmann, J.; Nichtl, A.; Kürzinger, K. *Nano Letters* **2003**, *3*, 935-938.

(2) Willets, K.; Van Duyne, R. *Annual Review of Physical Chemistry* **2007**, *58*, 267-297

(3) Homola, J.; Yee, S. S.; Gauglitz, G. *Sensors and Actuators B: Chemical* **1999**, *54*, 3-15.

(4) Cooper, M. A. *Nature Reviews Drug Discovery* **2002**, *1*, 515-528.

(5) Liedberg, B.; Nylander, C.; Lundström, I. *Biosens. Bioelectron.* **1995**, *10*, i-ix.

(6) Liedberg, B.; Nylander, C.; Lundström, I. *Sens. Actuators* **1983**, *4*, 299-304.

(7) Löfas, S.; Malmqvist, M.; Ronnberg, I.; Stenberg, E.; Liedberg, B.; Lundström, I. *Sens. Actuators B* **1991**, *5*, 79-84.

(8) Nylander, C.; Liedberg, B.; Lind, T. *Sensors and Actuators* **1983**, *3*, 79-88.

(9) Haes, A.; Van Duyne, R. *Anal. Bioanal. Chem.* **2004**, *379*, 920-930.

(10) Kelly, K. L.; Coronado, E.; Zhao, L. L.; Schatz, G. C. *The Journal of Physical Chemistry B* **2002**, *107*, 668-677.

(11) Link, S.; El-Sayed, M. A. *Annu. Rev. Phys. Chem.* **2003**, *54*, 331-366.

(12) Chen, P.; Selegård, R.; Aili, D.; Liedberg, B. *Nanoscale* **2013**, *5*, 8973-8976.

(13) Bănică, F.-G. In *Chemical Sensors and Biosensors*; John Wiley & Sons, Ltd: 2012, p 1-20.

(14) Yao, H.; Zhang, Y.; Xiao, F.; Xia, Z.; Rao, J. *Angewandte Chemie International Edition* **2007**, *46*, 4346-4349.

(15) Omidinia, E.; Shadjou, N.; Hasanzadeh, M. *Applied Biochemistry and Biotechnology* **2013**, 1-11.

(16) Rangin, M.; Basu, A. *J. Am. Chem. Soc.* **2004**, *126*, 5038-5039.

(17) Voss, S.; Fischer, R.; Jung, G.; Wiesmüller, K.-H.; Brock, R. *J. Am. Chem. Soc.* **2006**, *129*, 554-561.

(18) Schedin, F.; Geim, A.; Morozov, S.; Hill, E.; Blake, P.; Katsnelson, M.; Novoselov, K. *Nature Materials* **2007**, *6*, 652-655.

(19) Wang, A.-J.; Guo, H.; Zhang, M.; Zhou, D.-L.; Wang, R.-Z.; Feng, J.-J. *Microchimica Acta* **2013**, *180*, 1051-1057.

(20) Fan, H.; Li, Y.; Wu, D.; Ma, H.; Mao, K.; Fan, D.; Du, B.; Li, H.; Wei, Q. *Analytica chimica acta* **2012**, *711*, 24-28.

(21) Ai, K.; Liu, Y.; Lu, L. *Journal of the American Chemical Society* **2009**, *131*, 9496-9497.

(22) Day, J. S.; Edwards, H. G.; Dobrowski, S. A.; Voice, A. M. *Spectrochimica Acta Part A: Molecular and Biomolecular Spectroscopy* **2004**, *60*, 563-568.

(23) Solans, A.; Carnicero, M.; De la Torre, R.; Segura, J. *Journal of analytical toxicology* **1995**, *19*, 104-114.

(24) Kim, T. H.; Lee, B. Y.; Jaworski, J.; Yokoyama, K.; Chung, W.-J.; Wang, E.; Hong, S.; Majumdar, A.; Lee, S.-W. *ACS Nano* **2011**, *5*, 2824-2830.

(25) Liu, X.; Wang, Y.; Chen, P.; Wang, Y.; Zhang, J.; Aili, D.; Liedberg, B. *Analytical Chemistry* **2014**, *86*, 2345-2352.

(26) Hornbeck, P. *Current protocols in immunology* **1991**, 2.1. 1-2.1. 22.

(27) Rodahl, M.; Hook, F.; Fredriksson, C.; A. Keller, C.; Krozer, A.; Brzezinski, P.; Voinova, M.; Kasemo, B. *Faraday Discussions* **1997**, *107*, 229-246.

(28) Drummond, T. G.; Hill, M. G.; Barton, J. K. *Nat Biotech* **2003**, *21*, 1192-1199.

(29) Roche Diagnostics: Indianapolis, 2004; Vol. 101 pages.

(30) Bell, R. P.; Goldfarb, J. P.; Prokop, G. F.; Google Patents: 2000.

(31) Elghanian, R.; Storhoff, J. J.; Mucic, R. C.; Letsinger, R. L.; Mirkin, C. A. *Science* **1997**, *277*, 1078.

(32) Preechaburana, P.; Gonzalez, M. C.; Suska, A.; Filippini, D. *Angewandte Chemie* **2012**, *124*, 11753-11756.

(33) Lu, C.; Yang, H.; Zhu, C.; Chen, X.; Chen, G. *Angewandte Chemie International Edition* **2009**, *48*, 4785-4787.

(34) Artyukhin, A. B.; Stadermann, M.; Friddle, R. W.; Stroeve, P.; Bakajin, O.; Noy, A. *Nano Letters* **2006**, *6*, 2080-2085.

(35) Borovsky, D.; Powell, C. A.; Carlson, D. A. *Archives of insect biochemistry and physiology* **1992**, *21*, 13-21.

(36) Engvall, E.; Perlmann, P. *Immunochemistry* **1971**, *8*, 871-874.

(37) Van Weemen, B.; Schuurs, A. *FEBS letters* **1971**, *15*, 232-236.

(38) Löfås, S.; Malmqvist, M.; Rönnberg, I.; Stenberg, E.; Liedberg, B.; Lundström, I. *Sensors and Actuators B: Chemical* **1991**, *5*, 79-84.

(39) Nenninger, G. G.; Tobiška, P.; Homola, J.; Yee, S. S. *Sensors and Actuators B: Chemical* **2001**, *74*, 145-151.

(40) Slavík, R.; Homola, J. *Sensors and Actuators B: Chemical* **2007**, *123*, 10-12.

(41) Hartland, G. V.; Schatz, G. *J. Phys. Chem. C* **2011**, *115*, 15121-15123.

(42) Campion, A.; Kambhampati, P. *Chem. Soc. Rev.* **1998**, *27*, 241-250.

(43) Pompa, P.; Martiradonna, L.; Della Torre, A.; Della Sala, F.; Manna, L.; De Vittorio, M.; Calabi, F.; Cingolani, R.; Rinaldi, R. *Nature Nanotech.* **2006**, *1*, 126-130.

(44) Odom, T. W.; Schatz, G. C. *Chem. Rev.* **2011**, *111*, 3667-3668.

(45) Nath, N.; Chilkoti, A. *Anal. Chem.* **2001**, *74*, 504-509.

(46) Nath, N.; Chilkoti, A. *Anal. Chem.* **2004**, *76*, 5370-5378.

(47) Aili, D.; Selegård, R.; Baltzer, L.; Enander, K.; Liedberg, B. *Small* **2009**, *5*, 2445-2452.

(48) Cao, Y. C.; Jin, R.; Mirkin, C. A. *Science* **2002**, *297*, 1536-1540.

(49) Mie, G. *Annalen der Physik* **1908**, *330*, 377-445.

(50) Bohren, C. F.; Huffman, D. R. *Absorption and scattering of light by small particles*; Wiley, 2008.

(51) Yurkin, M. A.; Hoekstra, A. G. *Journal of Quantitative Spectroscopy and Radiative Transfer* **2007**, *106*, 558-589.

(52) Tanev, S.; Tuchin, V.; Paddon, P. *Laser Physics Letters* **2006**, *3*, 594-598.

(53) Johnson, P. B.; Christy, R. W. *Phys. Rev. B* **1972**, *6*, 4370-4379.

(54) Berciaud, S.; Cognet, L.; Tamarat, P.; Lounis, B. *Nano Lett.* **2005**, *5*, 515-518.

(55) Kreibig, U.; Vollmer, M. *Optical properties of metal clusters*; Springer-Verlag: Berlin, 1995.

(56) Nusz, G. J.; Marinakos, S. M.; Curry, A. C.; Dahlin, A.; Hook, F.; Wax, A.; Chilkoti, A. *Anal. Chem.* **2008**, *80*, 984-989.

(57) Spadavecchia, J.; Barras, A.; Lyskawa, J.; Woisel, P.; Laure, W.; Pradier, C.-M.; Boukherroub, R.; Szunerits, S. *Anal. Chem.* **2013**, *85*, 3288-3296.

(58) Sun, Y.; Xia, Y. *Anal. Chem.* **2002**, *74*, 5297-5305.

(59) Shen, Y.; Zhou, J.; Liu, T.; Tao, Y.; Jiang, R.; Liu, M.; Xiao, G.; Zhu, J.; Zhou, Z.-K.; Wang, X.; Jin, C.; Wang, J. *Nat. Commun.* **2013**, *4*.

(60) Im, H.; Bantz, K. C.; Lee, S. H.; Johnson, T. W.; Haynes, C. L.; Oh, S.-H. *Adv. Mater.* **2013**, *25*, 2678-2685.

(61) Martinsson, E.; Shahjamali, M. M.; Enander, K.; Boey, F.; Xue, C.; Aili, D.; Liedberg, B. *J. Phys. Chem. C* **2013**, *117*, 23148-23154.

(62) Mirkin, C. A.; Letsinger, R. L.; Mucic, R. C.; Storhoff, J. J. *Nature* **1996**, *382*, 607-609.

(63) Li, H.; Rothberg, L. *Proc. Nat. Acad. Sc. U. S.* **2004**, *101*, 14036-14039.

(64) Aili, D.; Gryko, P.; Sepulveda, B.; Dick, J. A. G.; Kirby, N.; Heenan, R.; Baltzer, L.; Liedberg, B.; Ryan, M. P.; Stevens, M. M. *Nano Lett.* **2011**.

(65) Chen, C.-K.; Huang, C.-C.; Chang, H.-T. *Biosens. Bioelectron.* **2010**, *25*, 1922-1927.

(66) Sun, J.; Ge, J.; Liu, W.; Wang, X.; Fan, Z.; Zhao, W.; Zhang, H.; Wang, P.; Lee, S.-T. *Nano Res.* **2012**, *5*, 486-493.

(67) Du, J.; Zhu, B.; Chen, X. *Small* **2013**, *9*, 4104-4111.

(68) Ai, K.; Liu, Y.; Lu, L. *J. Am. Chem. Soc.* **2009**, *131*, 9496-9497.

(69) Jiang, Y.; Zhao, H.; Zhu, N.; Lin, Y.; Yu, P.; Mao, L. *Angew. Chem.* **2008**, *120*, 8729-8732.

(70) Aili, D.; Enander, K.; Baltzer, L.; Liedberg, B. *Nano Lett.* **2008**, *8*, 2473-2478.

(71) Liu, J.; Lu, Y. *Nat. Protoc.* **2006**, *1*, 246-252.

(72) Su, X.; Kanjanawarut, R. *ACS Nano* **2009**, *3*, 2751-2759.

(73) Chang, C.-C.; Chen, C.-Y.; Chen, C.-P.; Lin, C.-W. *Anal. Methods* **2014**.

(74) Chen, Y.-Y.; Unnikrishnan, B.; Li, Y.-J.; Huang, C.-C. *Analyst* **2014**, *139*, 5977-5982.

(75) Aili, D.; Enander, K.; Rydberg, J.; Nesterenko, I.; Björefors, F.; Baltzer, L.; Liedberg, B. *J. Am. Chem. Soc.* **2008**, *130*, 5780-5788.

(76) Liu, X. H.; Wang, Y.; Chen, P.; Wang, Y.; Zhang, J.; Aili, D.; Liedberg, B. *Anal. Chem.* **2014**, *86*, 2345-2352.

(77) Chandrawati, R.; Stevens, M. M. *Chem. Commun.* **2014**.

(78) Ding, X.; Ge, D.; Yang, K.-L. *Sensor Actuat B-Chem* **2014**, *201*, 234-239.

(79) Sato, K.; Hosokawa, K.; Maeda, M. *Nucleic Acids Res.* **2005**, *33*, e4-e4.

(80) Tan, Y. N.; Su, X.; Zhu, Y.; Lee, J. Y. *ACS Nano* **2010**, *4*, 5101-5110.

(81) Tan, Y. N.; Su, X.; Liu, E. T.; Thomsen, J. S. *Anal. Chem.* **2010**, *82*, 2759-2765.

(82) Jain, P. K.; El-Sayed, M. A. *Nano Letters* **2008**, *8*, 4347-4352.

(83) Fan, J. A.; Bao, K.; Wu, C.; Bao, J.; Bardhan, R.; Halas, N. J.; Manoharan, V. N.; Shvets, G.; Nordlander, P.; Capasso, F. *Nano Letters* **2010**, *10*, 4680-4685.

(84) Luk'yanchuk, B.; Zheludev, N. I.; Maier, S. A.; Halas, N. J.; Nordlander, P.; Giessen, H.; Chong, C. T. *Nature Materials* **2010**, *9*, 707-715.

(85) Xu, X.; Peng, B.; Li, D.; Zhang, J.; Wong, L. M.; Zhang, Q.; Wang, S.; Xiong, Q. *Nano Lett* **2011**, *11*, 3232-3238.

(86) Verellen, N.; Van Dorpe, P.; Huang, C.; Lodewijks, K.; Vandenbosch, G. A. E.; Lagae, L.; Moshchalkov, V. V. *Nano Lett* **2011**, *11*, 391-397.

(87) Rodríguez-Lorenzo, L.; de La Rica, R.; Álvarez-Puebla, R. A.; Liz-Marzán, L. M.; Stevens, M. M. *Nature Mater.* **2012**, *11*, 604-607.

(88) Anker, J. N.; Hall, W. P.; Lyandres, O.; Shah, N. C.; Zhao, J.; Van Duyne, R. P. *Nature Mater.* **2008**, *7*, 442-453.

(89) Carpay, F.; Cense, W. *Nature Phys. Sci.* **1973**, *241*.

(90) Vigderman, L.; Khanal, B. P.; Zubarev, E. R. *Advanced Materials* **2012**, *24*, 4811-4841.

(91) Jana, N.; Gearheart, L.; Murphy, C. *Chemical Communications* **2001**, *2001*, 617-618.

(92) Liu, Y.; Walker, A. R. H. *Angewandte Chemie* **2010**, *122*, 6933-6937.

(93) Chen, H.; Kou, X.; Yang, Z.; Ni, W.; Wang, J. *Langmuir* **2008**, *24*, 5233-5237.

(94) Pelton, M.; Sader, J. E.; Burgin, J.; Liu, M.; Guyot-Sionnest, P.; Gosztola, D. *Nature Nanotechnology* **2009**, *4*, 492-495.

(95) Chen, P.; Yin, Z.; Huang, X.; Wu, S.; Liedberg, B.; Zhang, H. *J. Phys. Chem. C* **2011**, *115*, 24080-24084.

(96) Link, S.; Wang, Z. L.; El-Sayed, M. A. *The Journal of Physical Chemistry B* **1999**, *103*, 3529-3533.

(97) Xia, Y.; Xiong, Y.; Lim, B.; Skrabalak, S. *Angew. Chem. Int. Ed* **2009**, *48*, 60–103.

(98) Zorić, I.; Zäch, M.; Kasemo, B.; Langhammer, C. *ACS Nano* **2011**, *5*, 2535-2546.

(99) Sugawa, K.; Tahara, H.; Yamashita, A.; Otsuki, J.; Sagara, T.; Harumoto, T.; Yanagida, S. *ACS Nano* **2015**, DOI: 10.1021/nn506800a.

(100) Wang, Y.; Aili, D.; Selegard, R.; Tay, Y.; Baltzer, L.; Zhang, H.; Liedberg, B. *Journal of Materials Chemistry* **2012**, *22*, 20368-20373.

(101) Hiramatsu, H.; Osterloh, F. E. *Chemistry of Materials* **2004**, *16*, 2509-2511.

(102) Tao, A.; Habas, S.; Yang, P. *Small* **2008**, *4*, 310.

(103) Sun, Y.; Xia, Y. *The Analyst* **2003**, *128*, 686-691.

(104) Sun, Y.; Xia, Y. *Analytical Chemistry* **2002**, *74*, 5297-5305.

(105) Malinsky, M. D.; Kelly, K. L.; Schatz, G. C.; Van Duyne, R. P. *Journal of the American Chemical Society* **2001**, *123*, 1471-1482.

(106) McFarland, A. D.; Van Duyne, R. P. *Nano Letters* **2003**, *3*, 1057-1062.

(107) Lee, K.-S.; El-Sayed, M. A. *J. Phys. Chem. B* **2006**, *110*, 19220-19225.

(108) Dondapati, S. K.; Sau, T. K.; Hrelescu, C.; Klar, T. A.; Stefani, F. D.; Feldmann, J. *ACS Nano* **2010**, *4*, 6318-6322.

(109) Martinsson, E.; Shahjamali, M. M.; Enander, K.; Boey, F.; Xue, C.; Aili, D.; Liedberg, B. *The Journal of Physical Chemistry C* **2013**, *117*, 23148-23154.

(110) Lee, Y. H.; Chen, H.; Xu, Q.-H.; Wang, J. *The Journal of Physical Chemistry C* **2011**, *115*, 7997-8004.

(111) Sannomiya, T.; Sahoo, P. K.; Mahcicek, D. I.; Solak, H. H.; Hafner, C.; Grieshaber, D.; Vörös, J. *Small* **2009**, *5*, 1889-1896.

(112) Liu, S.-D.; Yang, Z.; Liu, R.-P.; Li, X.-Y. *J. Phys. Chem. C* **2011**, *115*, 24469-24477.

(113) Kim, Y.-P.; Oh, Y.-H.; Oh, E.; Ko, S.; Han, M.-K.; Kim, H.-S. *Analytical Chemistry* **2008**, *80*, 4634-4641.

(114) Jain, P. K.; Huang, W.; El-Sayed, M. A. *Nano Lett.* **2007**, *7*, 2080-2088.

(115) Sönnichsen, C.; Reinhard, B.; Liphardt, J.; Alivisatos, A. *Nature biotechnology* **2005**, *23*, 741-745.

(116) Tabor, C.; Murali, R.; Mahmoud, M.; El-Sayed, M. A. *The Journal of Physical Chemistry A* **2008**, *113*, 1946-1953.

(117) Aili, D.; Enander, K.; Rydberg, J.; Lundström, I.; Baltzer, L.; Liedberg, B. *J. Am. Chem. Soc.* **2006**, *128*, 2194-2195.

(118) Chai, F.; Wang, C.; Wang, T.; Li, L.; Su, Z. *ACS Applied Materials & Interfaces* **2010**, *2*, 1466-1470.

(119) Kuang, H.; Chen, W.; Yan, W.; Xu, L.; Zhu, Y.; Liu, L.; Chu, H.; Peng, C.; Wang, L.; Kotov, N. A.; Xu, C. *Biosensors and Bioelectronics* **2011**, *26*, 2032-2037.

(120) Chah, S.; Hammond, M. R.; Zare, R. N. *Chemistry & Biology* **2005**, *12*, 323-328.

(121) Laromaine, A.; Koh, L.; Murugesan, M.; Ulijn, R. V.; Stevens, M. M. *Journal of the American Chemical Society* **2007**, *129*, 4156-4157.

(122) You, C.-C.; Miranda, O. R.; Gider, B.; Ghosh, P. S.; Kim, I.-B.; Erdogan, B.; Krovi, S. A.; Bunz, U. H.; Rotello, V. M. *Nature Nanotechnology* **2007**, *2*, 318-323.

(123) Yang, R.; Jin, J.; Chen, Y.; Shao, N.; Kang, H.; Xiao, Z.; Tang, Z.; Wu, Y.; Zhu, Z.; Tan, W. *Journal of the American Chemical Society* **2008**, *130*, 8351-8358.

(124) Chang, H.; Tang, L.; Wang, Y.; Jiang, J.; Li, J. *Analytical Chemistry* **2010**, *82*, 2341-2346.

(125) Zhang, M.; Yin, B.-C.; Tan, W.; Ye, B.-C. *Biosensors and Bioelectronics* **2011**, *26*, 3260-3265.

(126) Song, Y.; Qu, K.; Zhao, C.; Ren, J.; Qu, X. *Advanced Materials* **2010**, *22*, 2206-2210.

(127) Raman, C. V. *Indian Journal of physics* **1928**, *2*, 387-398.

(128) Fleischmann, M.; Hendra, P. J.; McQuillan, A. J. *Chemical Physics Letters* **1974**, *26*, 163-166.

(129) Jeanmaire, D. L.; Van Duyne, R. P. *Journal of Electroanalytical Chemistry and Interfacial Electrochemistry* **1977**, *84*, 1-20.

(130) Lee, S. J.; Guan, Z.; Xu, H.; Moskovits, M. *The Journal of Physical Chemistry C* **2007**, *111*, 17985-17988.

(131) Stiles, P. L.; Dieringer, J. A.; Shah, N. C.; Van Duyne, R. P. *Annual Review of Analytical Chemistry* **2008**, *1*, 601-626.

(132) Braun, G.; Pavel, I.; Morrill, A. R.; Seferos, D. S.; Bazan, G. C.; Reich, N. O.; Moskovits, M. *Journal of the American Chemical Society* **2007**, *129*, 7760-7761.

(133) Camden, J. P.; Dieringer, J. A.; Wang, Y.; Masiello, D. J.; Marks, L. D.; Schatz, G. C.; Van Duyne, R. P. *Journal of the American Chemical Society* **2008**, *130*, 12616-12617.

(134) Lee, S. J.; Morrill, A. R.; Moskovits, M. *Journal of the American Chemical Society* **2006**, *128*, 2200-2201.

(135) Liusman, C.; Li, S.; Chen, X.; Wei, W.; Zhang, H.; Schatz, G. C.; Boey, F.; Mirkin, C. A. *ACS Nano* **2010**, *4*, 7676-7682.

(136) Qin, L.; Zou, S.; Xue, C.; Atkinson, A.; Schatz, G. C.; Mirkin, C. A. *Proceedings of the National Academy of Sciences* **2006**, *103*, 13300-13303.

(137) Nie, S.; Emory, S. R. *Science* **1997**, *275*, 1102-1106.

(138) Hildebrandt, P.; Stockburger, M. *The Journal of Physical Chemistry* **1984**, *88*, 5935-5944.

(139) Ling, X.; Xie, L.; Fang, Y.; Xu, H.; Zhang, H.; Kong, J.; Dresselhaus, M.; Zhang, J.; Liu, Z. *Nano Letters* **2010**, *10*, 553-561.

(140) Wei, F.; Zhang, D.; Halas, N. J.; Hartgerink, J. D. *The Journal of Physical Chemistry B* **2008**, *112*, 9158-9164.

(141) Nabiev, I. R.; Savchenko, V. A.; Efremov, E. S. *Journal of Raman Spectroscopy* **1983**, *14*, 375-379.

(142) Suh, J. S.; Moskovits, M. *Journal of the American Chemical Society* **1986**, *108*, 4711-4718.

(143) Bell, S. E. J.; Sirimuthu, N. M. S. *Journal of the American Chemical Society* **2006**, *128*, 15580-15581.

(144) Koglin, E.; Séquaris, J. M.; Valenta, P. *Journal of Molecular Structure* **1982**, *79*, 185-189.

(145) Hall, W. P.; Modica, J.; Anker, J.; Lin, Y.; Mrksich, M.; Van Duyne, R. P. *Nano Letters* **2011**, *11*, 1098-1105.

(146) Dahlin, A. B.; Tegenfeldt, J. O.; Höök, F. *Analytical Chemistry* **2006**, *78*, 4416-4423.

(147) Novoselov, K. S.; Geim, A. K.; Morozov, S. V.; Jiang, D.; Zhang, Y.; Dubonos, S. V.; Grigorieva, I. V.; Firsov, A. A. *Science* **2004**, *306*, 666-669.

(148) Novoselov, K. S.; Geim, A. K.; Morozov, S. V.; Jiang, D.; Katsnelson, M. I.; Grigorieva, I. V.; Dubonos, S. V.; Firsov, A. A. *Nature* **2005**, *438*, 197-200.

(149) Novoselov, K. S.; Jiang, Z.; Zhang, Y.; Morozov, S. V.; Stormer, H. L.; Zeitler, U.; Maan, J. C.; Boebinger, G. S.; Kim, P.; Geim, A. K. *Science* **2007**, *315*, 1379-.

(150) Avouris, P. *Nano Letters* **2010**, *10*, 4285-4294.

(151) Ju, L.; Geng, B.; Horng, J.; Girit, C.; Martin, M.; Hao, Z.; Bechtel, H. A.; Liang, X.; Zettl, A.; Shen, Y. R.; Wang, F. *Nat Nano* **2011**, *6*, 630-634.

(152) Swathi, R.; Sebastian, K. *The Journal of Chemical Physics* **2009**, *130*, 086101.

(153) Kasry, A.; Ardakani, A. A.; Tulevski, G. S.; Menges, B.; Copel, M.; Vyklicky, L. *The Journal of Physical Chemistry C* **2012**, *116*, 2858-2862.

(154) Li, X.; Cai, W.; An, J.; Kim, S.; Nah, J.; Yang, D.; Piner, R.; Velamakanni, A.; Jung, I.; Tutuc, E.; Banerjee, S. K.; Colombo, L.; Ruoff, R. S. *Science* **2009**, *324*, 1312-1314.

(155) Li, D.; Muller, M. B.; Gilje, S.; Kaner, R. B.; Wallace, G. G. *Nat Nano* **2008**, *3*, 101-105.

(156) Huang, X.; Yin, Z.; Wu, S.; Qi, X.; He, Q.; Zhang, Q.; Yan, Q.; Boey, F.; Zhang, H. *Small* **2011**.

(157) Zhou, X.; Huang, X.; Qi, X.; Wu, S.; Xue, C.; Boey, F.; Yan, Q.; Chen, P.; Zhang, H. *The Journal of Physical Chemistry C* **2009**, *113*, 10842-10846.

(158) Dreyer, D. R.; Park, S.; Bielawski, C. W.; Ruoff, R. S. *Chemical Society Reviews* **2010**, *39*, 228-240.

(159) Liu, Y.; Dong, X.; Chen, P. *Chemical Society Reviews* **2012**, *41*, 2283-2307.

(160) Wang, Z.; Zhang, J.; Chen, P.; Zhou, X.; Yang, Y.; Wu, S.; Niu, L.; Han, Y.; Wang, L.; Boey, F.; Zhang, Q.; Liedberg, B.; Zhang, H. *Biosens. Bioelectron.* **2011**, *26*, 3881-3886.

(161) Dong, X.; Shi, Y.; Huang, W.; Chen, P.; Li, L.-J. *Advanced Materials* **2010**, *9999*, NA.

(162) Yang, M.; Javadi, A.; Li, H.; Gong, S. *Biosensors and Bioelectronics* **2010**, *26*, 560-565.

(163) Sudibya, H. G.; He, Q.; Zhang, H.; Chen, P. *ACS Nano* **2011**, *5*, 1990-1994.

(164) Mao, S.; Lu, G.; Yu, K.; Bo, Z.; Chen, J. *Advanced Materials* **2010**, *22*, 3521-3526.

(165) Zhou, M.; Zhai, Y.; Dong, S. *Analytical Chemistry* **2009**, *81*, 5603-5613.

(166) Tang, L.; Wang, Y.; Li, Y.; Feng, H.; Lu, J.; Li, J. *Advanced Functional Materials* **2009**, *19*, 2782-2789.

(167) Xu, H.; Dai, H.; Chen, G. *Talanta* **2010**, *81*, 334-338.

(168) Kang, X.; Wang, J.; Wu, H.; Aksay, I. A.; Liu, J.; Lin, Y. *Biosensors and Bioelectronics* **2009**, *25*, 901-905.

(169) Su, B.; Tang, J.; Huang, J.; Yang, H.; Qiu, B.; Chen, G.; Tang, D. *Electroanalysis* **2010**, *22*, 2720-2728.

(170) Aili, D.; Stevens, M. M. *Chemical Society Reviews* **2010**, *39*, 3358-3370.

(171) Anai, T.; Nakata, E.; Koshi, Y.; Ojida, A.; Hamachi, I. *Journal of the American Chemical Society* **2007**, *129*, 6232-6239.

(172) Tothill, I. In *Recognition Receptors in Biosensors*; Zourob, M., Ed.; Springer New York: 2010, p 249-274.

(173) Turner, A. P. F. *Chemical Society Reviews* **2013**, *42*, 3184-3196.

(174) Enander, K.; Aili, D.; Baltzer, L.; Lundström, I.; Liedberg, B. *Langmuir* **2005**, *21*, 2480-2487.

(175) Aili, D.; Tai, F.-I.; Enander, K.; Baltzer, L.; Liedberg, B. *Angewandte Chemie International Edition* **2008**, *47*, 5554-5556.

(176) Suzuki, M. M.; Matsumoto, M.; Yamamoto, A.; Ochiai, M.; Horiuchi, Y.; Niwa, M.; Omi, H.; Kobayashi, T.; Takagi, T. *Journal of Microbiological Methods* **2010**, *83*, 153-155.

(177) Beutler, B.; Rietschel, E. T. *Nat Rev Immunol* **2003**, *3*, 169-176.

(178) Rajah, K. Q. a. A. *British Journal of Medical Practitioners* **2008**, *1*, 7-12.

(179) Munford, R. S. *Annual Review of Pathology: Mechanisms of Disease* **2006**, *1*, 467-496.

(180) Wang, C.; Qi, H.; Qiu, X.; Gao, Q.; Zhang, C. *Analytical Methods* **2012**, *4*, 2469-2474.

(181) Wang, Y.; Huang, C.-J.; Jonas, U.; Wei, T.; Dostalek, J.; Knoll, W. *Biosens. Bioelectron.* **2010**, *25*, 1663-1668.

(182) Yin, X.; Schäferling, M.; Metzger, B.; Giessen, H. *Nano Lett.* **2013**, *13*, 6238-6243.

(183) Link, S.; El-Sayed, M. A. *J. Phys. Chem. B* **1999**, *103*, 4212-4217.

(184) Zhao, Y.; Zhou, F.; Zhou, H.; Su, H. *Phys. Chem. Chem. Phys.* **2013**, *15*, 1690-1698.

(185) Urban, A. S.; Shen, X.; Wang, Y.; Large, N.; Wang, H.; Knight, M. W.; Nordlander, P.; Chen, H.; Halas, N. J. *Nano Lett.* **2013**, *13*, 4399-4403.

(186) Hentschel, M.; Saliba, M.; Vogelgesang, R.; Giessen, H.; Alivisatos, A. P.; Liu, N. *Nano Lett.* **2010**, *10*, 2721-2726.

(187) Emani, N. K.; Chung, T.-F.; Kildishev, A. V.; Shalaev, V. M.; Chen, Y. P.; Boltasseva, A. *Nano Lett* **2013**, *14*, 78-82.

(188) Chen, P.; Selegård, R.; Aili, D.; Liedberg, B. *Nanoscale*, *5*, 8973-8976.

(189) Wang, Z.; Zhang, J.; Yin, Z.; Wu, S.; Mandler, D.; Zhang, H. *Nanoscale* **2012**, *4*, 2728-2733.

(190) Feuz, L.; Jonsson, M. P.; Höök, F. *Nano Lett.* **2012**, *12*, 873-879.

(191) Lu, G.; Li, H.; Wu, S.; Chen, P.; Zhang, H. *Nanoscale* **2012**, *4*, 860-863.

(192) Wu, K.; Rodríguez-Córdoba, W. E.; Yang, Y.; Lian, T. *Nano Lett.* **2013**, *13*, 5255-5263.

(193) Paz-Soldan, D.; Lee, A.; Thon, S. M.; Adachi, M. M.; Dong, H.; Maraghechi, P.; Yuan, M.; Labelle, A. J.; Hoogland, S.; Liu, K.; Kumacheva, E.; Sargent, E. H. *Nano Lett.* **2013**, *13*, 1502-1508.

(194) Rosman, C.; Prasad, J.; Neiser, A.; Henkel, A.; Edgar, J.; Sönnichsen, C. *Nano Lett.* **2013**, *13*, 3243-3247.

(195) Holzner, F.; Kuemin, C.; Paul, P.; Hedrick, J. L.; Wolf, H.; Spencer, N. D.; Duerig, U.; Knoll, A. W. *Nano Lett* **2011**, *11*, 3957-3962.

(196) Lodewijks, K.; Van Roy, W.; Borghs, G.; Lagae, L.; Van Dorpe, P. *Nano Lett.* **2012**, *12*, 1655-1659.

(197) Hall, W. P.; Modica, J.; Anker, J.; Lin, Y.; Mrksich, M.; Van Duyne, R. P. *Nano Lett.* **2011**, *11*, 1098-1105.

(198) Zhang, Y.; Wen, F.; Zhen, Y.-R.; Nordlander, P.; Halas, N. J. *Proc. Natl. Acad. Sci.* **2013**, *110*, 9215-9219.

(199) Freeman, R. G.; Grabar, K. C.; Allison, K. J.; Bright, R. M.; Davis, J. A.; Guthrie, A. P.; Hommer, M. B.; Jackson, M. A.; Smith, P. C.; Walter, D. G.; Natan, M. J. *Science* **1995**, *267*, 1629-1632.

(200) Martinsson, E.; Sepulveda, B.; Chen, P.; Elfwing, A.; Liedberg, B.; Aili, D. *Plasmonics* **2014**, DOI:10.1007/s11468-11013-19659-y.

(201) Chakravarthi, S.; Jessop, C. E.; Bulleid, N. J. *EMBO Rep* **2006**, *7*, 271-275.

(202) Peters, A. L.; Van Noorden, C. J. *J Histochem Cytochem* **2009**, *57*, 1003-1011.

(203) Kaplan, W.; Husler, P.; Klump, H.; Erhardt, J.; Sluis-Cremer, N.; Dirr, H. *Protein Sci* **1997**, *6*, 399-406.

(204) Frens, G. *Nature-Physical Science* **1973**, *241*, 20-22.

(205) Azzam, H.; Arand, G.; Lippman, M.; Thompson, E. *JNCI Journal of the National Cancer Institute* **1993**, *85*, 1758.

(206) Egeblad, M.; Werb, Z. *Nature Reviews Cancer* **2002**, *2*, 163-176.

(207) Luukkaa, H.; Klemi, P.; Hirsimäki, P.; Vahlberg, T.; Kivisaari, A.; Kähäri, V.; Grénman, R. *Acta Oncologica* **2010**, *49*, 85-90.

(208) Sier, C.; Kubben, F.; Ganesh, S.; Heerding, M.; Griffioen, G.; Hanemaaijer, R.; Van Krieken, J.; Lamers, C.; Verspaget, H. *British journal of cancer* **1996**, *74*, 413.

(209) Luukkaa, H.; Klemi, P.; Hirsimäki, P.; Vahlberg, T.; Kivisaari, A.; Kähäri, V.; Grénman, R. **2009**.

(210) Kioi, M.; Yamamoto, K.; Higashi, S.; Koshikawa, N.; Fujita, K.; Miyazaki, K. *Oncogene* **2003**, *22*, 8662-8670.

(211) Bjurlin, M. A.; Bloomer, S.; Nelson, C. J. *Biotechnology Letters* **2002**, *24*, 191-195.

(212) Zhao, Z.; Raftery, M. J.; Niu, X. M.; Daja, M. M.; Russell, P. J. *ELECTROPHORESIS* **2004**, *25*, 1142-1148.

(213) Shi, L.; De Paoli, V.; Rosenzweig, N.; Rosenzweig, Z. *Journal of the American Chemical Society* **2006**, *128*, 10378-10379.

(214) Odom, T. W.; Schatz, G. C. *Chemical Reviews* **2011**, *111*, 3667-3668.

(215) Song, J.; Li, Z.; Cheng, Y.; Liu, C. *Chemical Communications* **2010**, *46*, 5548-5550.

(216) Aili, D.; Mager, M.; Roche, D.; Stevens, M. M. *Nano Lett.* **2010**, *11*, 1401-1405.

(217) Ghadiali, J. E.; Stevens, M. M. *Adv. Mater.* **2008**, *20*, 4359-4363.

(218) *Journal of Nanoscience and Nanotechnology* **2010**, *10*, 4154-4158.

(219) Daniel, W.; Han, M.; Lee, J.; Mirkin, C. *J. Am. Chem. Soc* **2009**, *131*, 6362-6363.

(220) Xu, X.; Daniel, W. L.; Wei, W.; Mirkin, C. A. *Small* **2010**, *6*, 623-626.

(221) Loo, C.; Lowery, A.; Halas, N.; West, J.; Drezek, R. *Nano Lett* **2005**, *5*, 709-711.

(222) Huschka, R.; Neumann, O.; Barhoumi, A.; Halas, N. J. *Nano Letters* **2010**, *10*, 4117-4122.

(223) Guarise, C.; Pasquato, L.; De Filippis, V.; Scrimin, P. *Proceedings of the National Academy of Sciences of the United States of America* **2006**, *103*, 3978-3982.

(224) Alexander, P.; Oncogene Research Products: 2002; Vol. 2, p 11.

(225) Ghosh, S. K.; Pal, T. *Chemical Reviews* **2007**, *107*, 4797-4862.

(226) Hoekstra, R.; Eskens, F. A. L. M.; Verweij, J. *The Oncologist* **2001**, *6*, 415-427.

(227) In *Inhibitor SourceBook*; Calbiochem p119-122.

(228) Ress, C.; Tschoner, A.; Ciardi, C.; Laimer, M. W.; Engl, J. W.; Sturm, W.; Weiss, H.; Tilg, H.; Ebenbichler, C. F.; Patsch, J. R. *Eur. Cytokine Netw* **2010**, *21*, 65-70.

(229) Eustis, S.; El-Sayed, M. *Chem. Soc. Rev.* **2006**, *35*, 209-217.

(230) Graham, D. *Angewandte Chemie International Edition* **2010**, n/a-n/a.

(231) Shim, S.; Stuart, C.; Mathies, R. *ChemPhysChem* **2008**, *9*, 697-699.

(232) Schrader, B.; Moore, D. *Pure Appl. Chem* **1997**, *69*, 1451-1468.

(233) McLellan, J. M.; Li, Z.-Y.; Siekkinen, A. R.; Xia, Y. *Nano Letters* **2007**, *7*, 1013-1017.

(234) Xie, L.; Ling, X.; Fang, Y.; Zhang, J.; Liu, Z. *Journal of the American Chemical Society* **2009**, *131*, 9890-9891.

(235) Loh, K.; Bao, Q.; Ang, P.; Yang, J. *Journal of Materials Chemistry* **2010**, *20*, 2277-2289.

(236) Zhou, X.; Lu, G.; Qi, X.; Wu, S.; Li, H.; Boey, F.; Zhang, H. *The Journal of Physical Chemistry C* **2009**, *113*, 19119-19122.

(237) Lu, G.; Zhou, X.; Li, H.; Yin, Z.; Li, B.; Huang, L.; Boey, F.; Zhang, H. *Langmuir* **2010**, *26*, 6164-6166.

(238) Liu, Z.; Robinson, J. T.; Sun, X.; Dai, H. *Journal of the American Chemical Society* **2008**, *130*, 10876-10877.

(239) Andersson, O.; Nikkinen, H.; Kanmert, D.; Enander, K. *Biosensors and Bioelectronics* **2009**, *24*, 2458-2464.

(240) Tuinstra, F.; Koenig, J. *The Journal of Chemical Physics* **1970**, *53*, 1126.

(241) Piscanec, S.; Lazzeri, M.; Mauri, F.; Ferrari, A. C.; Robertson, J. *Physical Review Letters* **2004**, *93*, 185503.

(242) Ferrari, A. C.; Meyer, J. C.; Scardaci, V.; Casiraghi, C.; Lazzeri, M.; Mauri, F.; Piscanec, S.; Jiang, D.; Novoselov, K. S.; Roth, S.; Geim, A. K. *Physical Review Letters* **2006**, *97*, 187401.

(243) Dreyer, D.; Park, S.; Bielawski, C.; Ruoff, R. *Chemical Society Reviews* **2010**, *39*, 228-240.

(244) Kudin, K. N.; Ozbas, B.; Schniepp, H. C.; Prud'homme, R. K.; Aksay, I. A.; Car, R. *Nano Letters* **2007**, *8*, 36-41.

(245) Paredes, J. I.; Villar-Rodil, S.; Fernandez-Merino, M. J.; Guardia, L.; Martinez-Alonso, A.; Tascon, J. M. D. *Journal of Materials Chemistry* **2010**.

(246) Stankovich, S.; Dikin, D. A.; Piner, R. D.; Kohlhaas, K. A.; Kleinhammes, A.; Jia, Y.; Wu, Y.; Nguyen, S. T.; Ruoff, R. S. *Carbon* **2007**, *45*, 1558-1565.

(247) Colthup, N.; Daly, L.; Wiberley, S. *Introduction to infrared and Raman spectroscopy*; Academic press New York, 1964.

(248) Ling, X.; Zhang, J. *Small* **2010**, *6*, 2020-2025.

(249) Moskovits, M. *Reviews of Modern Physics* **1985**, *57*, 783.

(250) Moskovits, M. *The Journal of Chemical Physics* **1978**, *69*, 4159.

(251) Swathi, R.; Sebastian, K. *The Journal of Chemical Physics* **2008**, *129*, 054703.

(252) Baskaran, D.; Mays, J.; Zhang, X.; Bratcher, M. *J. Am. Chem. Soc* **2005**, *127*, 6916-6917.

(253) Tidswell, M.; LaRosa, S. P. *Expert Review of Anti-infective Therapy* **2011**, *9*, 507-520.

(254) Beutler, B.; Poltorak, A. *Critical Care Medicine* **2001**, *29*, S2-S6.

(255) Louren ço, F. R.; Botelho, T. D. S.; Pinto, T. D. J. A. *PDA Journal of Pharmaceutical Science and Technology* **2012**, *66*, 542-546.

(256) Morita, T.; Nakamura, T.; Miyata, T.; Iwanaga, S. *Progress in clinical and biological research* **1985**, *189*, 53-66.

(257) Balagopal, A.; Gama, L.; Franco, V.; Russell, J. N.; Quinn, J.; Higgins, Y.; Smeaton, L. M.; Clements, J. E.; Thomas, D. L.; Gupta, A.; for the, N.; team, A. s. *PLoS ONE* **2012**, *7*, e41258.

(258) Cooper, J. F.; Weary, M. E.; Jordan, F. T. *PDA Journal of Pharmaceutical Science and Technology* **1997**, *51*, 2-6.

(259) Elin, R. J.; Wolff, S. M. *Journal of Infectious Diseases* **1973**, *128*, 349-352.

(260) Ding, J.; Ho, B. In *Endotoxins: Structure, Function and Recognition*; Wang, X., Quinn, P. J., Eds.; Springer Netherlands: 2010; Vol. 53, p 187-208.

(261) Du, Z.; Yang, R.; Guo, Z.; Song, Y.; Wang, J. *Analytical Chemistry* **2002**, *74*, 5487-5491.

(262) Drummelsmith, J.; Winstall, E.; Bergeron, M. G.; Poirier, G. G.; Ouellette, M. *Journal of Proteome Research* **2007**, *6*, 4690-4702.

(263) Blomquist, P. H. *Transactions of the American Ophthalmological Society* **2006**, *104*, 322.

(264) Sieradzki, K.; Roberts, R. B.; Haber, S. W.; Tomasz, A. *New England Journal of Medicine* **1999**, *340*, 517-523.

(265) Yin, Z.; He, Q.; Huang, X.; Zhang, J.; Wu, S.; Chen, P.; Lu, G.; Zhang, Q.; Yan, Q.; Zhang, H. *Nanoscale* **2012**, *4*, 293-297.